# *Progress Towards Rydberg Dynamics in an Ultra-Cold Atomic Ensemble and the Visualisation of Arbitrary Qutrit States*

MAX ZACHARY FESTENSTEIN

# Progress Towards Rydberg Dynamics in an Ultra-Cold Atomic Ensemble and the Visualisation of Arbitrary Qutrit States

**Max Zachary Festenstein**

A thesis presented for the degree of
Doctor of Philosophy


Quantum Light and Matter
Durham University
United Kingdom
March 2023

# Progress Towards Rydberg Dynamics in an Ultra-Cold Atomic Ensemble and the Visualisation of Arbitrary Qutrit States

**Max Zachary Festenstein**

**Abstract**

This thesis describes the processes performed to restore an existing platform for Rydberg quantum optics to experimental readiness. The setup itself is initially described before the the process of re-evacuation of the experimental chamber following a vacuum break is detailed. Once ultra-high vacuum conditions had been restored, work was conducted to lower the temperature of the atomic cloud, produced by a Magneto-Optical Trap and further cooled by sub-Doppler cooling. The temperatures of the clouds produced were optimised down to $33.6 \pm 1.3$ $\mu$K measured by Time of Flight absorption imaging following the ballistic expansion of the cooled clouds.

Separate from the experiment, this thesis outlines the development of a visualisation method, bearing resemblance to the Bloch sphere for qubits, for three level qutrits. This visualisation method encapsulates all 8 dimensions required to describe any qutrit density matrix, which is a linear sum of the 8 Gell-Mann matrices. The dynamics of a qutrit can be well articulated in an easy to interpret fashion with this visualisation, and a set of common atomic physics processes are modelled to highlight the dynamics that can be conveyed via this framework.

Supervisors: Charles S. Adams and Kevin J. Wetherill

Dedicated to

my grandpa, Harold Morris.

A man of great determination, with a ferocious curiosity and an unending fascination;
you were a tailor by trade, but scientists the world over can learn from your example.

# Acknowledgements

Getting to the point of producing this document has been quite the journey. For no particular reason, conducting experimental research in 2020 presented an unprecedented challenge for us as it did everyone. Despite this, my supervisor, Stuart Adams, proved a fantastic supervisor throughout. His enthusiasm, intellectual insights and ideas for research avenues were always appreciated. Stuart struck a balance between direction for the project and space to pursue things ourselves that I very much appreciated. Though he has decades of experience over me, he always listened and considered any ideas put forward to him.

I also owe a great deal of thanks to my secondary supervisor Kevin Weatherill. Where Stuart offered conceptual support and direction, Kev was always available to answer any practical question, and offer hands-on advice regarding equipment or techniques. On top of this, Kev's pastoral support was invaluable throughout my time in QLM and I am immensely grateful for his proofreading of chapter 3.

My time at Durham was supported by the exceeding generosity of Drs Rodney and Frances Stubbs, who funded my research. It was a pleasure to meet both of you and I am immensesly grateful for the opportunity you have provided.

Along with my supervisors and benefactors, I also need to thank those who helped me during my time in the QLM group. Viv Kendon pointed me in the direction of the experimental projects in QLM during my undergraduate degree, Kali Wilson and Jack Segal helped me with the experimental techniques that were used throughout the PhD during my first year here, Danielle Pizzey walked the Rydberg Quantum Optics team through the vacuum repair process step-by-step and creating such a good quality vacuum wouldn't have happened without her and Nicholas Chancellor provided guidance and more than one proof-read on the qutrit visualisation paper on which chapter 4 is based. To Nick I wish the best of luck in his new position in Newcastle University, I've no doubt he'll be as much of an asset to their

group as he has been here. On the RQO team, Lucy Downes joined latterly but was a hugely supportive post-doc during her time on the project, and very kindly proofread my theory chapter, and Karen Wadenpfuhl, who joined the team as an MSc student, was brilliant for bouncing ideas, both theoretical and experimental, back and forth as well as navigating the Austrian postal system! To every one of you, thank you so much for the help in getting me where I am now. Finally, my thanks go to Oliver Hughes. When I arrived on the RQO project, Oli took the time to get me up to speed with the day-to-day running of the experiment and remained a fantastic lab partner and friend throughout my PhD. Whether we were repairing the vacuum chamber, re-constructing the laser system or he was talking me out of my more... visionary ideas, it was a pleasure to have worked with him.

In the wider QLM group, I thank Ifan Hughes and Simon Gardiner for the extremely useful feedback that resulted in my qutrit visualisation paper, Tobias Franzen for answering any and all stupid questions, Anton 'Jimmy' Charman, Nick Spong and Yuechun Jiao. Outside of QLM, my thanks go to Thomas Wall for offering such a warm introduction to cold atomic research, Zenos Christodoulides and Peter Curati.

Outside of academia, those who know me will know that I am a big fan of ultimate frisbee. During my time at both Imperial and Durham, the university frisbee teams (disc Doctors and DUF) have provided a much needed escape from work and I'm incredibly appreciative to have been a part of them. Another pair of societies of note were the Imperial and (latterly) Durham Jewish societies. I met many wonderful people at both of these societies, and am grateful for the communities they provided. I thank Charlotte for helping keep my head held high through some of the tougher points of the PhD and I endlessly thank Gill for all she's done for me. To Benjamin Daniel, and (another) Oli, I couldn't ask for better friends. Finally, I must thank my family: my Mum, Dad, Grandpa, Grandma and Brother. Your support was and is unwavering, your love endless, and I wouldn't be the man I am without you. Thank you.

# Contents

# Declaration

The work in this thesis is based on research carried out at the Quantum Light and Matter Group, Department of Physics, Durham University, United Kingdom. No part of this thesis has been submitted elsewhere for any other degree or qualification, and it is the sole work of the author unless referenced to the contrary in the text.

Some of the work presented in this thesis has been published in journals and conference proceedings - the relevant publications are listed below.

## Publications

Max Z. Festenstein. "An Intuitive Visualisation Method for Arbitrary Qutrit States". In: (Apr. 2023). arXiv: 2304.01741

# List of Figures

# List of Tables

# Nomenclature

**2LS** Two Level System

**3LS** Three Level System

**AOM** Acousto-Optic Modulator

**AR** Anti Reflection

**BEC** Bose-Einstein Condensate

**CQED** Cavity Quantum Electro-Dynamics

**DExTer** Durham Experimental Terminal

**ECDL** External Cavity Diode Laser

**EIT** Electromagnetically Induced Transparency

**FFT** Fast Fourier Transform

**FORT** Far Off-Resonant dipole Trap

**FPGA** Field Programmable Gate Array

**FWM** Four Wave Mixing

**GM** Gell-Mann

**HWP** Half Wave Plate

**IG** Ion Gauge

**LIAD** Light Induced Atomic Desorption

**MOT** Magneto-Optical Trap

**MTS** Modulation Transfer Spectroscopy

**NA** Numerical Aperture

**NEG** Non-Evaporable Getter

**PBS** Polarising Beam Splitter

**PD** Photo-Diode

**PDH** Pound-Drever-Hall

**QIP** Quantum Information Processing

**QWP** Quarter Wave Plate

**RGA** Residual Gas Analyser

**RMS** Root-Mean-Square

**RWA** Rotating Wave Approximation

**SHG** Second Harmonic Generation

**SO** Special Orthogonal Group

**SU** Special Unitary Group

**SIP** Sputter Ion Pump

**SPAD** Single Photon Avalanche Diode

**STIRAP** STImulated Raman Adiabatic Passage

**TA** Tapered Amplifier

**TOF** Time Of Flight

**TC** Thermo-Couple

**UHV** Ultra-High Vacuum

**vdW** van der Waals

**ZMTS** Zeeman Modulation Transfer Spectroscopy

# 1 | Introduction

Since 1802 when absorption lines in sunlight were first documented, matter has been observed to interact with light at only discrete frequencies [1]. This observation of 'Fraunhofer lines' was studied further for over 100 years without a 'quantum' picture of atomic structure as we know it today [2, 3, 4, 5], before initial work was done by Neils Bohr in 1913 to formally quantise the energies of orbital electrons around a nucleus [6]. Despite this paradigm shift, the idea of photon-atom interactions was not introduced until Einstein postulated the existence of photons to explain the photoelectric effect [7], which began building the picture of the quantised energies involved in light-matter interactions. Following this, the full quantisation of the interactions between light fields and atoms followed [8, 9], giving theoretical descriptions of how light of known frequency and (crucially) phase would interact with atoms. Despite this theoretical understanding and aside from some limited work with incoherent sources [10], it took 33 years and the advent of the laser in 1958 [11] before extensive coherent atomic experimentation was possible. What followed was an explosion of research in the field of atomic physics now that the tools with which to probe the structure of atoms were available [12, 13, 14, 15, 16]. In 1987, E. Raab *et. al.* [17] experimentally demonstrated the groundbreaking MOT platform with which atoms could be trapped and cooled to fractions of a Kelvin [18, 19], opening up avenues for atomic dynamics observable only at exceptionally low energies such as Bose-Einstein Condensation [20].

Amidst these experimental developments, Feynman postulated that in order to properly simulate a quantum system, one would need a computer capable itself of utilising quantum mechanics in its processing [21]. In 2000, DiVincenzo's 7 requirements for such a device provided a set of benchmarks by which one could assess a quantum system's suitability for such a purpose [22]. Through coherent generation from laser light, photons immediately satisfy 5 of DiVincenzo's criteria, with the notable issues of interfacing with static quantum bits (qubits) and universal gate sets persisting [23]. One of the considerable challenges present when trying to tackle

the latter issue is the requirement for interacting qubits, which is near-impossible due to no appreciable linear photon-photon interactions [24]. Furthermore, interfacing between stationary 'static' and 'flying' qubits remains a significant hurdle to quantum computation. Using atom clouds as an intermediary offers a potential solution to these issues, as coherent interactions are possible. This allows them to mediate the interactions between otherwise non-interacting light fields. An example of such an effect is the Electromagnetically Induced Transparency (EIT) process [25, 26], whereby a beam of light resonant with an atomic transition is passed through a bulk quantity (be it in a thermal cell or ultra-cold cloud) of that atomic species. Normally, photons from this beam would be absorbed by the cloud as they address transitions within the atoms, however by adding an additional beam resonant to a second transition, the atoms enter a 'dark state' superposition whereby they no longer absorb photons from the first beam. A diagram of this process is shown in figure 1.1. The EIT process has indeed seen use in Quantum Information Processing (QIP), and has been used for purposes such as quantum memories [27, 28, 29] and photonic phase gates [30, 31, 32, 33].

## 1.1 Rydberg Atoms

A Rydberg atom is one where one of its valence electrons is excited to a high principle quantum number, endowing it with several properties of experimental interest as described in section 2.3. Two of these effects are the large dipole-dipole [34, 35, 36], and van der Waals (vdW) interactions. Another of these, a long radiative lifetime, allows for their use in inducing the aforementioned EIT phenomenon [26]. [37, 38, 39]. As these act over distances much greater than inter-atomic spacing in a typical ultra-cold atomic experiment, long range interactions between Rydberg atoms can be induced. One of these, that is employed in the experiment described in this work, is the 'Rydberg blockade' (sometimes referred to as the 'dipole blockade') effect [40, 41]. This effect prevents two Rydberg atoms forming within a certain 'blockade radius' $r_{\mathrm{B}}$, ensuring the presence of only a single excited atom. By generating this atom as a superposition over $\mathcal{N}$ atoms in a cloud within a blockade radius, this Rydberg excitation can be collectively encoded into the entire ensemble. By collectively encoding a Rydberg excitation in this way, effective Rabi frequencies between states are enhanced by a factor $\propto \sqrt{\mathcal{N}}$. Cavity Quantum Electro-Dynamics (CQED) provides another route for the enhancement of light matter interactions [42], but has more significant experimental complexities, making collective Rydberg encoding preferential in obtaining this enhancement [43].

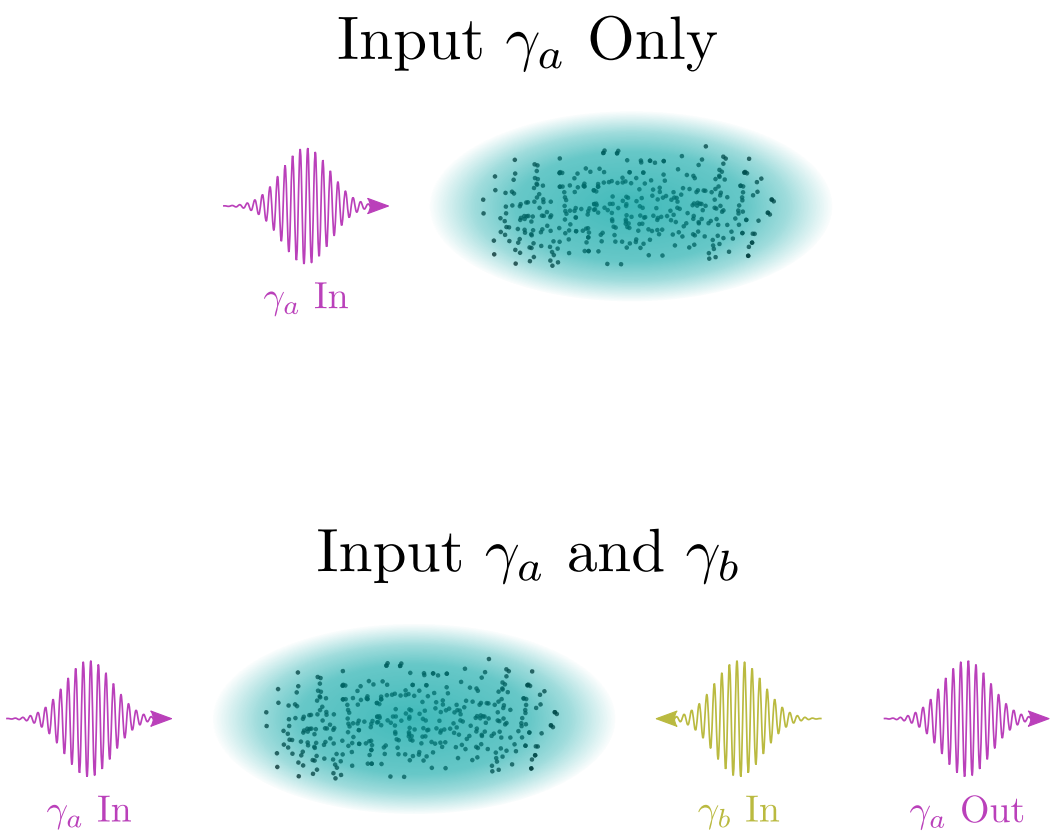


Figure 1.1: Diagram showing an atomic-mediated interaction between two radiation fields. **Upper**: Input photon $\gamma_a$ is absorbed by the atomic cloud (cyan and black) and no light is transmitted. **Lower**: By adding a second radiation field with corresponding photons $\gamma_b$, an EIT type interaction between the two fields and the atomic cloud can occur, allowing for the photon $\gamma_a$ to pass through the medium. One perspective on this interaction is that of a logical **AND** gate, by taking $\gamma_a$ and $\gamma_b$ In to be the two gate inputs and $\gamma_a$ Out to be the gate output.

Applications of Rydberg atoms within QIP are varied, providing a potential candidate for a quantum bit (qubit) [44] that are suitable for multi-qubit gates [45] and quantum simulators [46, 47] to name a few. Additionally, outside of QIP, they remain a versatile tool for conducting experiments investigating fundamental physics [42, 48, 49, 50, 51, 52, 53].

With many potential avenues for experimentation, a versatile setup that allows for the reliable creation and manipulation of Rydberg atoms is desirable. Such features could include: consistent generation of a desired number of Rydberg atoms, detection of any Rydberg atoms being formed, equipment to transition a Rydberg atom between states, environmental control to vary the conditions (such as electric and magnetic fields) the excited atoms are subjected to and the ability to readily

repeat experiments to build statistically significant data sets. These features were of chief consideration between the past and present iterations of the experiment described in this work.

## 1.2 Experimental Apparatus

The experimental apparatus described here has gone through a number of generational iterations [54, 55, 56, 57].

**Generation 1: Constructed by J. Pritchard and K. Weatherill** for the purpose of studing few-photon optical non-linearities induced by Ryderg states.

**Generation 2: Constructed by D. Maxwell, D. Paredes-Barato and J. Pritchard** to first realise collective Rydberg encoding in our laboratory, and perform experiments using microwave fields to drive to adjacent Rydberg states.

**Generation 3: Constructed by S. Ball and H. Busche** to improve the existing setup, and increase the repetition rate of the experiment. Using this setup, a collectively encoded qubit and single-atom interferometer were realised.

Our experimental apparatus is composed of two main chambers. The upper chamber is dedicated to the initial 2D MOT cooling required to bring atoms down from thermal temperatures to those where further cooling is possible and transport is possible. This chamber is situated above a larger circular-octagonal science chamber and is connected by a narrow aperture differential pumping tube to maintain a differential in vapour pressure between the chambers. In the lower chamber, referred to as the 'science chamber', all subsequent stages of atomic cooling and experimentation are performed. The science chamber contains several important *in-vacuo* components used to perform experiments on atomic ensembles. A trio of microwave antennae are available to drive transitions between Rydberg states via *ex-vacuo* microwave sources and an octet of split ring electrodes are used to generate an arbitrarily orientated DC electric field to induce Stark shifts or to simulate a noisy system [44]. Finally, a pair of high Numerical Aperture (NA) lenses are included to focus the dipole tweezer trap used as the final trapping stage, providing a narrow ($w_0 = 5$ $\mu$m) radial beam waist, aiding to ensure only one Rydberg exciton is created. In previous experiments on this setup, an additional 'cross trap' trapping beam was provided to further restrict the trap axially [58], but as no Rydberg experimentation was achieved in this work, it is not described.

## 1.3 Qutrits

By extending from two to three state levels, quantum trits (qutrits) allow for a much broader range of applications to their two level counterparts. One of these applications is in improving security in quantum communications. This can be done directly as by increasing the number of basis states one works with, the probability of an eavesdropper acquiring any useful information reduces $\propto 1/N$ for $N$ basis states [59]. Aside from this, other secure communication schemes using qutrits have been proposed [60, 61]. Furthermore, secure communications can be achieved indirectly, as the inclusion of a third auxiliary level is vital for qubit entanglement schemes such as the DLCZ protocol [62]. Additionally, schemes for optimisation algorithms [63], superdense coding [64, 65, 66] and teleportation [67, 68, 69, 70] present potential applications.

Though not strictly qutrits for QIP purposes, three levels (at minimum) are necessary to account for interesting atomic physics phenomena. Processes such as the aforementioned EIT [25, 71, 72, 73], as well as two-photon Raman transitions [74, 75, 76], STImulated Raman Adiabatic Passage (STIRAP) [77, 78, 79, 80], the recently developed 'Jump Protocol' (in a solid solid state system) [81], Four Wave Mixing (FWM) [55, 82, 83, 84, 85, 86, 87] and frequency doubling [88, 89, 90] all require three levels to encapsulate the dynamics induced during these processes.

## 1.4 Thesis Structure

The remainder of this thesis is structured as follows:

**Chapter 2** outlines the relevant theory for atom-light interactions and optical trapping. Following this, some of the key features of Rydberg atoms are detailed for context and motivation on elements of the experimental design.

**Chapter 3** details the apparatus utilised in optically trapping and cooling atomic $^{87}$Rb clouds to 33 $\mu$K. Following this, the process by which the apparatus was re-evacuated following a vacuum break is detailed before the processes of optimising the initial stages of trapping and cooling are outlined.

**Chapter 4** presents a visualisation method with which all 8 dimensions of an arbitrary qutrit state can be displayed. Using this visualisation method, some common atomic physics processes are modelled and illustrated.

**Chapter 5** concludes this thesis by summarising the work described and presenting potential avenues for future investigations.

## 1.5 Publications Arising From This Work

- Max Z. Festenstein. “An Intuitive Visualisation Method for Arbitrary Qutrit States". In: (Apr. 2023). arXiv: 2304.01741

# 2 | Theory

As the processes involved in optical trapping and Rydberg science require a good theoretical foundation with which to understand them, outlining the mechanisms by which these are achieved is of great import. As such, this chapter details the requisite theory for the understanding of optical trapping and Rydberg atomic properties and formation.

Before these, the equations that dictate the dynamics of a quantum system both with and without spontaneous decays are outlined. Following this, the properties of the atom used for experimentation, $^{87}$Rb , are stated.

## 2.1 Background

### 2.1.1 Atom-Light Interactions

To understand how light-matter interactions occur between atoms and incident radiation fields, we first look at the simplest case: the two level atom interacting with a laser field. The energy level diagram for this atom is shown in figure 2.1.

Here, the atom has two energy levels $|0\rangle$ and $|1\rangle$ separated by energy $E_{01} = \hbar\omega_{01}$ and driven by an incident laser field irradiating the atom with light of energy $E = \hbar\omega$. This light is detuned from resonance by a small frequency $\Delta_{01}$ where $\Delta_{01} \ll \omega_{01}$. Additionally, if the atom is excited up to $|1\rangle$, it decays back to the ground state $|0\rangle$ at a rate of $\Gamma_{10}$. Ignoring the decay mode $\Gamma_{10}$ for now, the evolution of this system is governed by the Schrödinger equation

$$i\hbar\frac{\partial}{\partial t}|\psi\rangle = \hat{\mathrm{H}}_{tot}|\psi\rangle, \tag{2.1}$$

where the Hamiltonian $\hat{\mathrm{H}}_{tot} = \hat{\mathrm{H}}_{atom} + \hat{\mathrm{H}}_{int}$ is the sum of the (internal) atomic and interaction Hamiltonians. The atomic Hamiltonian defines the energies of the

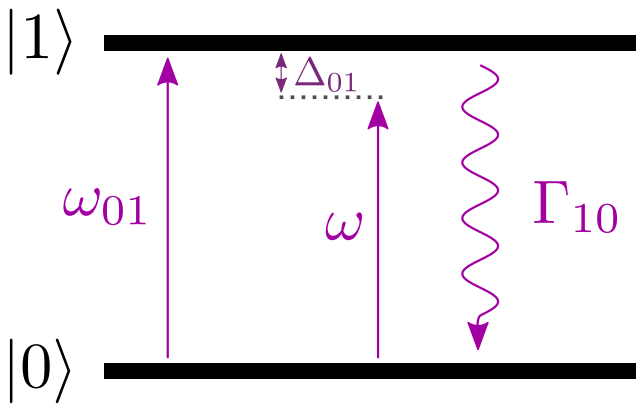


Figure 2.1: Energy level diagram showing two levels $|0\rangle$ and $|1\rangle$ separated by an energy $E_{01} = \hbar\omega_{01}$, driven by a laser field of energy $E = \hbar\omega$, detuned below resonance by $E_\Delta = \hbar\Delta_{01}$ and with a decay mode from $|1\rangle \rightarrow |0\rangle$ at a rate of $\Gamma_{10}$.

states in question. These are given as

$$\hat{\mathrm{H}}_{atom} = \hbar(\omega_0|0\rangle\langle 0| + \omega_1|1\rangle\langle 1|). \tag{2.2}$$

Written in matrix form and including the detuning $\Delta_{01}$ of a driving laser field from resonance, this is given as

$$\hat{\mathrm{H}}_{atom} = \hbar \begin{pmatrix} \omega_0 & 0 \\ 0 & \omega_1 - \Delta_{01} \end{pmatrix} \rightarrow \hat{\mathrm{H}}_{atom} = \hbar \begin{pmatrix} 0 & 0 \\ 0 & \omega_{01} - \Delta_{01} \end{pmatrix}, \tag{2.3}$$

where $\omega_{01} = \omega_1 - \omega_0$ in line with figure 2.1. In order to construct the interaction Hamiltonian, we consider the atom as an electric dipole with an electric dipole moment operator $\mathbf{d}$ interacting with a time dependant electric field $\mathbf{E}(t)$ resulting in a Hamiltonian of the form [91]

$$\hat{\mathrm{H}}_{int} = -\mathbf{d} \cdot \mathbf{E}(t). \tag{2.4}$$

In order to simplify evaluating (2.4), $\mathbf{E}(t)$ is defined along an arbitrary $\hat{\mathbf{x}}$ axis as $\mathbf{E}(t) = \mathrm{E}_0 \cos(\omega t)\hat{\mathbf{x}} = \frac{\mathrm{E}_0}{2}(\mathrm{e}^{i\omega t} + \mathrm{e}^{-i\omega t})\hat{\mathbf{x}}$ where $\omega$ is the frequency of the driving laser field. The dipole moment operator takes the form

$$\mathbf{d}_{jk} = \langle\psi_j|\mathbf{d}|\psi_k\rangle, \tag{2.5}$$

for an elementary charge $e$ [92]. As this is an odd parity, observable operator, the relations $\mathbf{d}_{jj} = 0$ and $\mathbf{d}_{jk} = \mathbf{d}_{kj}$ must both hold. Again, the orientation of the electric dipole is arbitrarily chosen to align along the $\hat{\mathbf{x}}$ axis such that the electric dipole moment can be expressed as $\mathbf{d} = \mathrm{d}\hat{\mathbf{x}}$ Thus, the overall form for $\hat{\mathrm{H}}_{int}$ for the two level case is given by

$$\hat{\mathrm{H}}_{int} = -\frac{\mathrm{E}_0\mathbf{d}_{01}}{2}(\mathrm{e}^{i\omega t} + \mathrm{e}^{-i\omega t})(|0\rangle\langle 1| + |1\rangle\langle 0|), \tag{2.6}$$

where $\omega = \omega_{01} - \Delta_{01}$ as in figure 2.1. One further definition is that of the Rabi frequency which in general between two states $j$ and $k$ is defined as [91]

$$\Omega_{jk} = \left| \frac{\mathrm{d}_{jk}\mathrm{E}_0}{\hbar} \right|. \tag{2.7}$$

After moving to the interaction picture of the detuned radiation field defined in Hamiltonian (2.3) and taking a Rotating Wave Approximation (RWA) to neglect fast moving terms [2], the overall Hamiltonian is now given by

$$\hat{\mathrm{H}}_{tot} = \hbar \begin{pmatrix} 0 & \frac{\Omega_{01}}{2} \\ \frac{\Omega_{01}}{2} & -\Delta_{01} \end{pmatrix}. \tag{2.8}$$

In the case of a pure state, where no decay mode $\Gamma_{10}$ exists, this Hamiltonian and the Schrödinger equation given in (2.1) are sufficient to encapsulate the system's dynamics. When including decay modes, however, the Schrödinger equation is no longer suitable as these decays must be accounted for. As such, the description of the quantum state shifts to one that allows for the inclusion of terms allowing for decay into the environment i.e. the density matrix $\rho$. This semi-classical description arises from decay modes inducing a dephasing of the quantum state which reduces the magnitudes of the off-diagonal coherence terms [93], as well as a loss of population in excited states. In the steady state in the presence of a constant field, the dephasing induced by the decay modes 'average out' all coherences and the state becomes a statistical mixture, where only the diagonal entries of the matrix remain. The simplest density matrix is that of the pure state

$$\rho = |\psi\rangle\langle\psi| = \sum_{j,k} \alpha_j \alpha_k^* |j\rangle\langle k|, \tag{2.9}$$

for eigenstates $|j\rangle$ and $|k\rangle$ and complex probability amplitudes $\alpha_j$ and $\alpha_k$. The equation used to model the time evolution of the density matrix when considering decay modes $\Gamma_{kj}$ is the Lindblad master equation [94], which takes the form

$$\frac{d}{dt}\rho = -i[\hat{\mathrm{H}}, \rho] + \hat{\mathcal{L}}, \tag{2.10}$$

where $\hat{\mathcal{L}}$ is defined as

$$\hat{\mathcal{L}} = \sum_j \Gamma_j \left( \mathrm{C}_j \rho \mathrm{C}_j^\dagger - \frac{1}{2}\{\rho, \mathrm{C}_j^\dagger \mathrm{C}_j\} \right), \tag{2.11}$$

for an $N$ dimensional quantum state with $j$ decay modes and associated collapse operators $\mathrm{C}_j$. In the case of the two level atom specified, the only decay mode is $\Gamma_{10}$ with the collapse operator $\mathrm{C} = |0\rangle\langle 1|$. This results in a decay matrix

$$\hat{\mathcal{L}} = \frac{\Gamma_{10}}{2} \begin{pmatrix} 2\rho_{11} & \rho_{01} \\ \rho_{10} & -2\rho_{11} \end{pmatrix}. \tag{2.12}$$

A natural extension of the Lindblad master equation described above, the 4 optical Bloch equations for a two level system simply consider each matrix element in (2.10) to give

$$\dot{\rho}_{00} = \Gamma_{10}\rho_{11} - i\Omega_{01}(\rho_{10} - \rho_{01}), \tag{2.13a}$$

$$\dot{\rho}_{01} = (\frac{\Gamma_{10}}{2} - i\Delta_{01})\rho_{01} + i\Omega_{01}(\rho_{11} - \rho_{00}), \tag{2.13b}$$

$$\dot{\rho}_{10} = (\frac{\Gamma_{10}}{2} - i\Delta_{01})\rho_{10} - i\Omega_{01}(\rho_{11} - \rho_{00}), \tag{2.13c}$$

$$\dot{\rho}_{11} = -\Gamma_{10}\rho_{11} + i\Omega_{01}(\rho_{10} - \rho_{01}). \tag{2.13d}$$

The extension of this model to three levels i.e. $|0\rangle, |1\rangle, |2\rangle$ provides the theoretical framework for the purposes of modelling the sequences presented in chapter 4. The equation in (2.10) was used for time evolution in these cases, and the system was advanced forward in time using element-wise finite differencing for each term in the density matrix at a given time step. The three level optical Bloch equations, looking at isolated density matrix terms, were only explicitly used to analytically find steady state solutions, rather than in any numerical capacity.

### 2.1.2 Rubidium Atomic Properties

The third heaviest alkali element, Rubidium has atomic number 37 with an electronic structure: [Kr] $5s^1$. The two stable isotopes are $^{85}$Rb and $^{87}$Rb with natural abundances of 72.17% and 27.83% respectively [95]. Though greater in natural abundance, the choice between isotopes has historically favoured the less abundant $^{87}$Rb , as the positive scattering length (and therefore repulsive inter-atomic interactions) of the heavier isotope facilitated the earliest experimental realisation of a Bose-Einstein Condensate (BEC) [96, 20]. This is not to say creating a BEC with $^{85}$Rb is impossible, as by reversing the sign of the scattering length using magnetic Feshbach resonances, Cornish *et. al.* realised this achievement [97]. Nonetheless, $^{87}$Rb is of primary focus in this work.

Like other group 1 elements, $^{87}$Rb has only one valence electron, allowing for an empirical expression of the electronic binding energy $E_\mathrm{b}$ with principle quantum number $n$, similar to the Rydberg series for Hydrogen; this is expressed as

$$E_\mathrm{b} = Rhc\frac{1}{(n - \delta_l)^2}, \tag{2.14}$$

where $R$ and $h$ are the Rydberg and Planck constants and $\delta_l$ is the experimentally determined quantum defect for angular momentum $l$. For the case of $l = s = 0$, this value is given as $\delta_s = 3.19$ [2]. Being a monovalent atom leads $^{87}$Rb to having a straightforward hyperfine structure, which are shown in figure 2.2(a) alongside the transitions of interest for atomic cooling in figure 2.2(b).

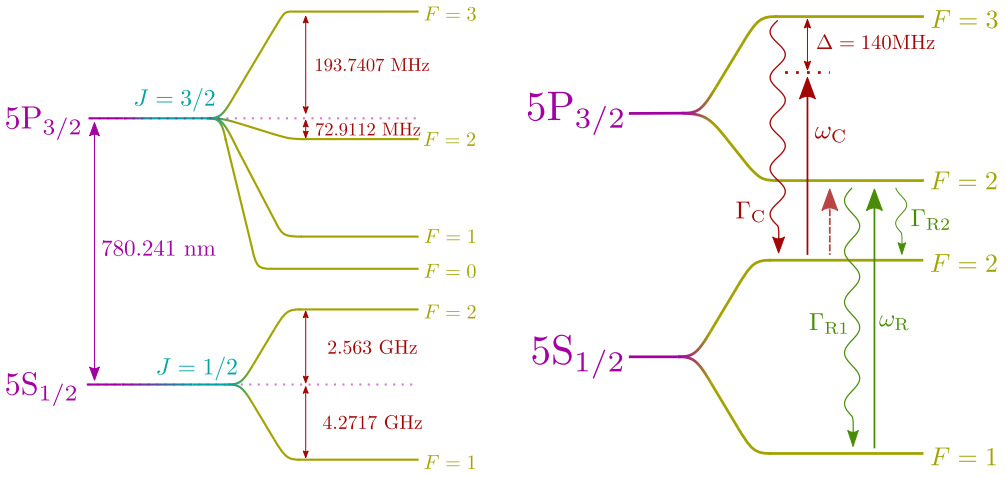


Figure 2.2: Hyperfine splitting of energy levels for $^{87}$Rb on the $D_2$ transition. **(a)**: Hyperfine (gold) splitting for the ground and first excited state of $^{87}$Rb . Relevant splittings from the central $D_2$ wavelength are shown in burgundy. Wavelength and frequency values for the $l = 0$ and $l = 1$ states are taken from [98] and [99] respectively. **(b)**: Energy levels of the cooling ($|F = 2\rangle \rightarrow |F' = 3\rangle$) and repump ($|F = 1\rangle \rightarrow |F' = 2\rangle$) transitions. The cooling ($\omega_C$) and repump ($\omega_R$) transitions are shown in burgundy and green respectively. Due to the large detuning $\Delta$ of $\omega_C$ from resonance, some population transfer $|F = 2\rangle \rightarrow |F' = 2\rangle$ occurs (dashed burgundy line), resulting in decay into the $|F = 1\rangle$ state ($\Gamma_{R1}$). Repump light ($\omega_R$) on the $|F = 1\rangle \rightarrow |F' = 2\rangle$ transition, shown in green, pumps atoms back into a state where decay back to $|F = 2\rangle$ ($\Gamma_{R2}$) is possible.

As $^{87}$Rb has nuclear spin $I = 3/2$, the range of hyperfine values $|J-I| < F < |J+I|$ for $J = 1/2$ and $J = 3/2$ are $1 < F < 2$ and $0 < F < 3$ respectively. The $l = 0$, $J = 1/2$ and $l = 1$, $J = 3/2$ hyperfine states are shown in figure 2.2(a) with the splitting of the relevant levels shown in burgundy. Figure 2.2(b) restricts the diagram to only the transitions used to cool atoms as described in section 2.2. In order to cool atoms, a transition with only one possible subsequent decay path (referred to as a 'closed' transition) is highly desirable. Such a transition exists in $^{87}$Rb , as the $|F = 2\rangle \rightarrow |F' = 3\rangle$ transition has only one decay path back down to $|F = 2\rangle$. As the laser light used to address this transition needs to be red-detuned from resonance (reasoned in section 2.2.1), a non-negligible population transfer between $|F = 2\rangle \rightarrow |F' = 2\rangle$ occurs; this can then in turn can cause atoms to decay into the dark state $|F = 1\rangle$ via decay mode $\Gamma_{R1}$, preventing any further

cooling. To resolve this issue, a single repump laser of frequency $\omega_{\mathrm{R}}$ is used to transfer atoms from $|F = 1\rangle \rightarrow |F' = 2\rangle$ where decay back to $|F = 2\rangle$ via $\Gamma_{\mathrm{R2}}$ is possible, readying them for further cooling.

## 2.2 Optical Trapping

Bringing atoms down to low enough temperatures for coherent Rydberg experimentation is a non-trivial undertaking, and a variety of methods are employed to realise this. Those employed in our setup are: MOT cooling, optical molasses sub-Doppler cooling and Far Off-Resonant dipole Trap (FORT) trapping. This section details the requisite theory to understand each.

### 2.2.1 Magneto-Optical Trapping

First proposed in 1979 [19] and later realised in 1985 [100], the MOT has revolutionised the field of cold atomic physics and is the foundational element of our apparatus. In the experimental setup described in chapter 3, the MOT acts as the first stage of the cooling process, reducing the temperature of $^{87}$Rb atoms to $\mathcal{O}(100)\mu$K before giving way to further preparatory stages. As this vital technique is indispensable to this experiment, the principle of its operation is detailed.

The (three dimensional) MOT consists of a set of three mutually orthogonal, retro-reflected laser beams crossing at a central point, with anti-Helmholtz magnetic field coils generating a field that is zeroed on this crossing point. A diagram of the 2D cross-section of this arrangement is shown in figure 2.3. This diagram shows the key elements of a MOT: the radiation and magnetic fields. Two orthogonal laser fields $\mathrm{L}_{x1}$ and $\mathrm{L}_{z1}$ (red) are retro-reflected ($\mathrm{L}_{x2}$ and $\mathrm{L}_{z2}$) such that the cloud in the centre of the trap (cyan circle) sees incoming laser light from all four directions. The third beam $\mathrm{L}_{y1}$ and its retro-reflection are not shown here, but would be going into and coming out from the page to provide a third radiation field orthogonal to the first two. The magnetic field coils are arranged in an anti-Helmholtz configuration, which results in a local minimum in magnetic field strength at the centre of the trap, increasing in magnitude along the paths of the radiation fields. The dashed black lines show the directions of the magnetic field across the trap and show that along the beam axes, the magnetic field is either parallel ($\mathrm{L}_x$) or anti-parallel ($\mathrm{L}_z$) to the incoming radiation.

This trapping realises two processes: velocity reduction via the radiation fields

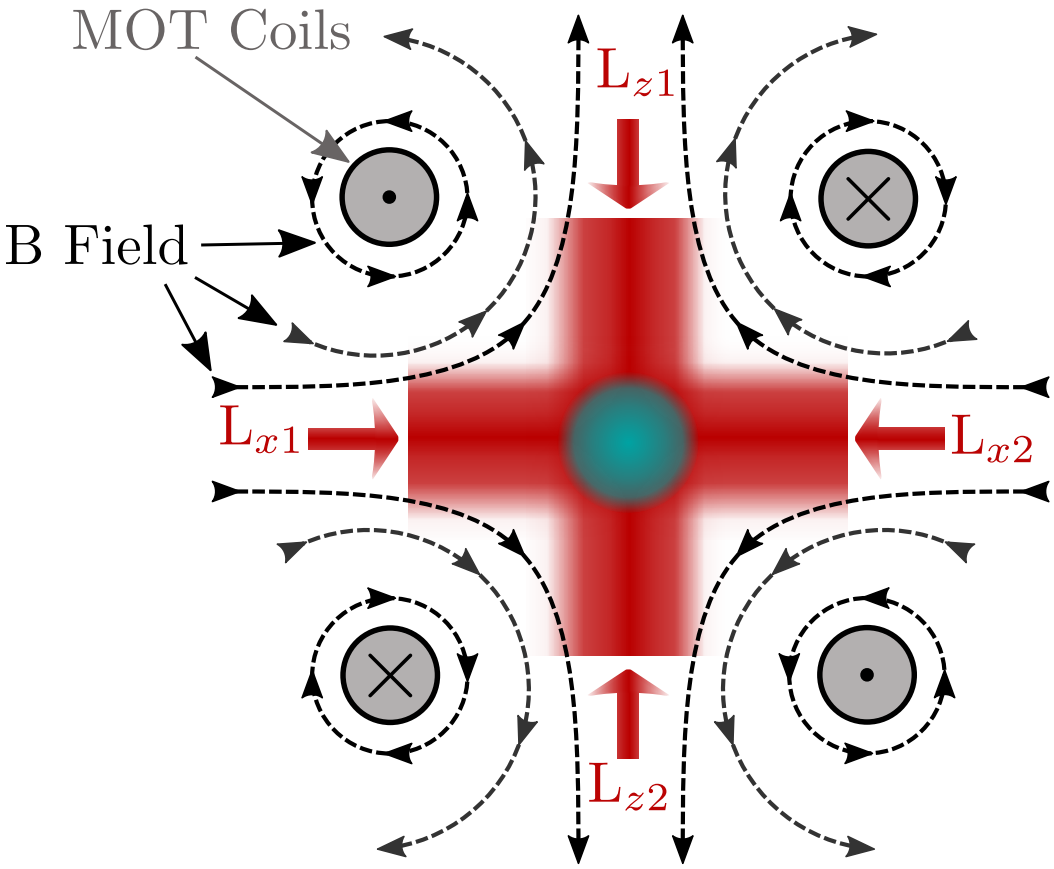


Figure 2.3: Two dimensional cross section of a Magneto-Optical Trap. Here, two incoming laser fields $L_{x1}$ and $L_{z1}$ (red) are retro-reflected ($L_{x2}$ and $L_{z2}$) such that four radiation fields are directed inwards and meet at a central point. A third beam $L_{y1}$ and its retro-reflection, which are not shown here, would be coming out from and going into the page, providing confinement in three orthogonal directions. Surrounding this crossing point are two electromagnetic field coils arranged in an anti-Helmholtz configuration (grey circles) with currents coming out from ($\cdot$) and going into ($\times$) the page. The dashed black lines show the direction of the magnetic field at a given location. The cyan cloud in the centre is where a cold cloud of atoms would form.

and spatial confinement with the magnetic fields. The mechanism by which atoms are slowed in the MOT is shown in figure 2.4.

The slowing process is illustrated by the atom in **(a)** as it moves towards the laser field $L_{x2}$. The energetic perspective of this atom is shown in **(b)**, and two energy levels $|g\rangle$ and $|e\rangle$ are considered with a transition frequency $\omega_0$ between them. In a stationary reference frame, each laser field addresses the atom with an off-resonant field of frequency $\omega_L = \omega_0 - \Delta_0$, preventing any stationary atoms from absorbing photons from the beams. When an atom moves towards the beam, however, the light is blue shifted onto resonance ($\Delta_{\nu 2}$) and the atom absorbs a photon from the beam $L_{x2}$. In absorbing this photon, the atom receives a momentum 'kick'

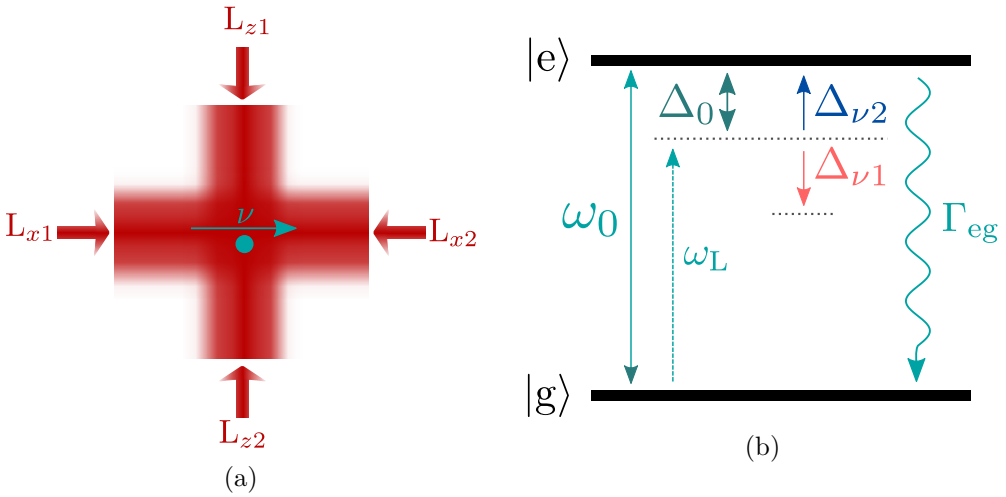


Figure 2.4: Mechanism for velocity slowing of atoms in a MOT. **(a)**: An atom in the trap moves toward (away from) beam $L_{x2}$ ($L_{x1}$) with velocity $\nu$. **(b)**: The laser fields in (a) address the transition between two atomic energy levels $|g\rangle$ and $|e\rangle$ with a transition frequency $\omega_0$ detuned from resonance by $\Delta_0$ resulting in $\omega_L = \omega_0 - \Delta_0$ (dashed cyan line). When the atom moves towards laser field $L_{x2}$, the frequency is blue shifted by $\Delta_{\nu 2} = \Delta_0$ onto resonance and a photon from the beam is absorbed. This provides a momentum kick in the direction of the blue shifted beam and thus slows the atom.

$p_\gamma = \hbar k$ in the opposite direction to the atom's velocity, thus reducing its overall velocity. If the atom is moving away from $L_{x2}$, the light will be red shifted away from resonance ($\Delta_{\nu 1}$) and no absorption occurs. By selecting a transition with a fast decay mode $\Gamma_{eg}$, the atom can re-enter $|g\rangle$ ready for another absorption. As this re-emission occurs in a random direction, the momentum change from this second process averages over the many cycles of absorption, resulting in a net momentum effect only in the direction of the laser beam. By applying this principle to all directions, the atom in **(a)** can be slowed in all directions.

With the above method atoms can be slowed in all three dimensions, but this alone provides no spatial trapping for atoms. To achieve this, a magnetic field of the form shown in figure 2.3 must be applied. The mechanism by which spatial confinement is achieved is shown in figure 2.5.
Subfigure **(a)** shows an atom displaced from the magnetic field centre B=0 by some amount $x_B$ in the direction of laser beam $L_{x2}$. For simplicity, extraneous field lines and beams have been omitted for visual clarity. Subplot **(b)** shows the energy level diagram of the atom between the two levels $|g\rangle$ and $|e\rangle$. As the atom moves away from the centre of the trap, the magnetic field it sees also increases. As such, this B field lifts the degeneracy of the angular momentum projection states $|m_e\rangle$ and induces a Zeeman shift of said states. Once this shift is equal to the detuning $\Delta_0$ of

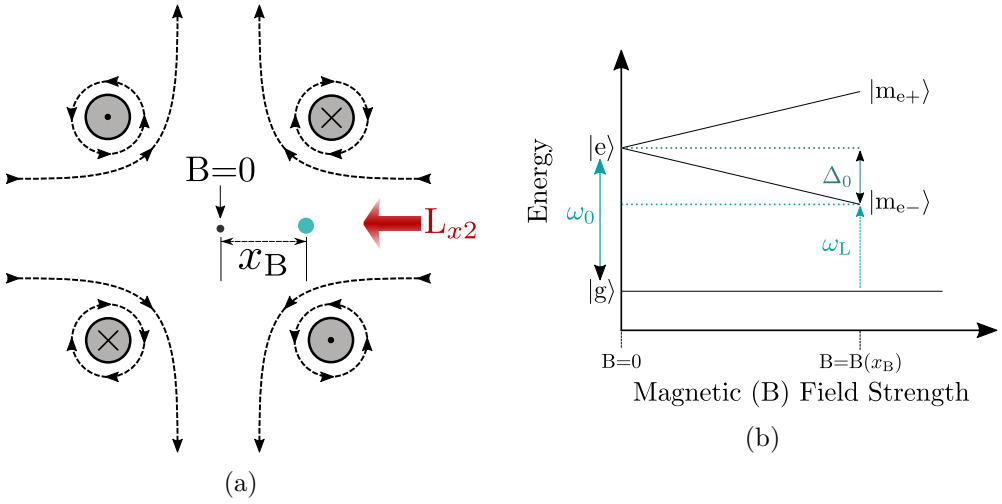


Figure 2.5: Mechanism for spatial confinement of atoms in a MOT. **(a)**: An atom (cyan) is displaced from the magnetic field zero point by a distance $x_B$. To simplify the diagram, only the circularly polarised laser field $L_{x2}$ is shown with a reduced number of field lines for ease of readability. **(b)**: Energetic diagram of the confinement process. Here, the two states $|g\rangle$ and $|e\rangle$ are again separated by transition frequency $\omega_0$, and have a laser driving field of frequency $\omega_L = \omega_0 - \Delta_0$. As the atom moves away from the centre of the trap, the larger the magnetic field it experiences becomes. This induces a Zeeman shift of the angular momentum projection states $|m_e\rangle$. At distance $x_B$, this Zeeman shift equates to the detuning $\Delta_0$ from resonance of the $\omega_L$ beam. As only light from laser field $L_{x2}$ addresses the transition with the correct-handedness circular polarisation, the atom is excited to $|m_{e-}\rangle$ and the atom gets a momentum kick from $L_{x2}$ back towards the centre of the trap.

$\omega_L$ from resonance, the atom absorbs a photon and is transferred into state $|m_{e-}\rangle$. Addressing this transition requires circularly polarised light of a specific handedness, therefore the only beam that is able to address this transition is $L_{x2}$ as the counterpropagating beam will be orthogonally polarised. By absorbing a photon from the $L_{x2}$ beam, the atom gets a momentum kick back towards the centre of the trap. This effect is replicated for all laser fields $L_{x,y,z}$ such that atoms are spatially confined to the centre of the trap.

Though this method of confinement and cooling is effective to a point, there is a lower limit to the temperature that is achievable using this method alone. This limit is set by the linewidth of the cooling transition, and arises due to the heating effect of the spontaneously emitted photon which, though random in direction, results in a momentum kick of the atom. As such, the lower limit achievable using only cooling reliant on Doppler shifted light (known as Doppler cooling) is given

by the 'Doppler Temperature'

$$\mathrm{T}_{min} = \frac{\hbar\Gamma_0}{2k_\mathrm{B}}, \tag{2.15}$$

where $\Gamma_0$ is the decay rate (and subsequently the linewidth) of the transition used in MOT cooling and $k_\mathrm{B}$ is the Boltzmann constant. For $^{87}$Rb , this temperature floor is $\sim 146$ $\mu$K. As motional dephasing will still wash out any dynamics of interest on the timescale of an experimental run outlined in chapter 3 [101, 32], additional cooling methods are required that can cool beyond what a MOT is capable of. Such methods are frequently referred to as sub-Doppler cooling techniques [2].

#### 2.2.1.1 Sub Doppler Cooling

Several methods of cooling below the Doppler temperature have been developed, including Degenerate Raman Sideband Cooling, Sisyphus cooling, and evaporative cooling to name but a few [102, 103, 104]. However, due to its simplicity and lack of additional equipment required to implement, the aforementioned optical molasses cooling method is that which is implemented in the experiment described in chapter 3 [105], thus a deeper examination of sub Doppler cooling is restricted only to this.

Despite offering the capability to cool beyond the Doppler temperature listed in (2.15), the physical mechanism of relying upon absorption and re-emission of photons in the presence of a laser field remains. Further relating to the experimental setup in chapter 3, the light used for sub-Doppler cooling is the same as that utilised in the initial Doppler cooling in the MOT albeit with a much greater detuning from resonance ($-40$ MHz increased from 11.9 MHz per figure 3.35). As such, the polarisation of the beams are circular for both Doppler and sub-Doppler stages of cooling. The resultant effect of two orthogonally polarised laser fields overlapping is a helically varying linearly polarised radiation field. A diagram of this field for one dimension of laser light is shown in figure 2.6. In this diagram, the atom (cyan) experiences a linearly polarised radiation field (gold) during the molasses cooling, but there is no net effect on the absorption of photons from either beam whilst it remains stationary. The interesting dynamics present themselves only when the atom moves toward either beam. The case where the atom moves toward field $\mathrm{L}_{x2}$ is described here.

Considering a frame of reference that is both moving at the speed of the atom, such that it has no translational motion, and rotating with the linearly polarised light, such that the polarisation appears fixed, the rotation of the atom generates

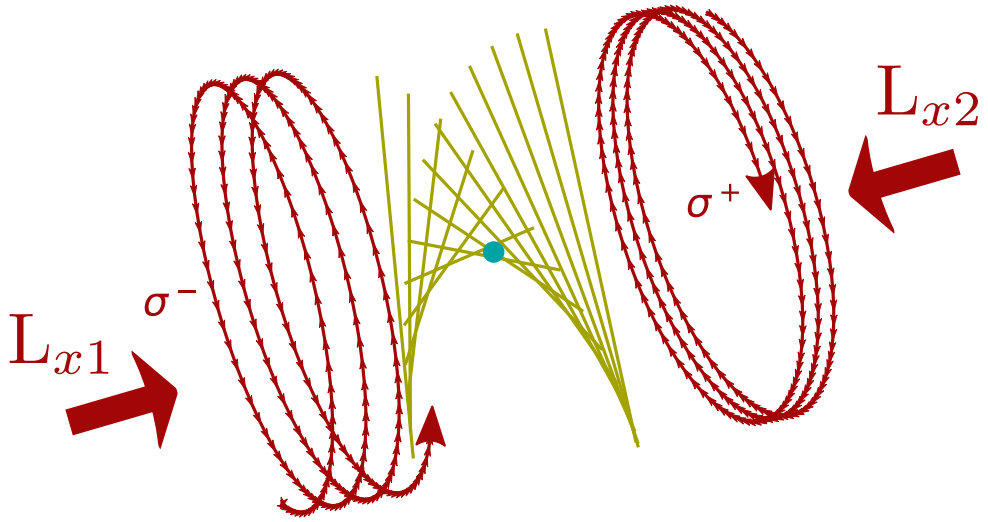


Figure 2.6: Diagram showing the radiation field generated by antiparallel $\sigma^+$ and $\sigma^-$ laser beams. The gold lines show the linear polarisation of the radiation field experienced by the atom (cyan).

an inertial field. This inertial field is magnetic, and is aligned colinearly with the laser field $L_{x2}$. This field lifts the degeneracy of the angular momentum projection states and the inertial field alters the eigenstates of the system. Considering these new eigenstates, the atom couples more strongly with the incoming $\sigma^+$ light compared to that from the $\sigma^-$ field. This results in the atom preferentially absorbing light from the $L_{x2}$ beam, thus reducing its overall momentum as it moves toward the oncoming beam. An equivalent effect occurs for atoms moving toward $L_{x1}$. This process is greatly paraphrased, and a detailed treatment of this mechanism, as well as Sisyphus cooling as previously mentioned, can be found in [103].

The key difference from the previously described Doppler cooling is that absorption of $\sigma^+$ photons is not induced by blue-shifting of the light *onto* resonance, but instead by the *increased coupling* to the detuned radiation field induced by the atom's motion. As a result, the photon spontaneously emitted by the atom is of slightly higher energy than that which it absorbed due to the large detuning of the radiation field. This means the temperature achievable using this process is lower than Doppler cooling alone. The lower limit of cooling by this method is set by the fact that the slowing mechanism of momentum kicks from photon absorptions necessitates the re-emission of the absorbed photon. Thus, though the momentum change by this process averages to 0, the Root-Mean-Square (RMS) momentum change from this process does not. From [103], this 'recoil temperature' is given by

$$T_{Rec} = \frac{(\hbar k)^2}{k_B m}, \tag{2.16}$$

for photonic wavevector $k$ and atomic mass $m$. For the optimised experimental sequence given in section 3.4.3 in chapter 3, this value is given as $T_{rec} \approx 0.4$ $\mu$K, which is over two orders of magnitude better than MOT cooling alone.

Though further temperature reduction is possible using methods such as the previously mentioned Degenerate Raman Sideband Cooling, the temperature range of $\mathcal{O}(10^{-5}$ K) is suitable for the purposes of this experiment. Temperature reduction alone is not enough to ready a cloud for experimentation, however, and trap geometry is of significant consideration. Due to the large beam sizes used in MOT cooling ($1/e^2$ diameter = 9 mm from section 3.2.1) to facilitate capturing atoms and an appreciable momentum spread of trapped atoms, the size of the atomic cloud at this stage is $\mathcal{O}$(mm). As such, the considerably smaller ($\mathcal{O}(\mu$m) down from $\mathcal{O}$(mm)) FORT is utilised to achieve the desired reduction in cloud size.

### 2.2.2 Dipole Trapping

As stated in the previous section, further cooling is not required in our system, precluding the need to implement evaporative cooling using the FORT which is a common final cooling stage for experiments, such as Bose Einstein Condensate formation. Nonetheless, a FORT is desired to reduce the size of the atomic cloud whilst maintaining density and temperature.

To understand the trapping potential experienced by an atom in a FORT, the atom is considered as an electric dipole, magnitude p given by

$$\mathrm{p} = \alpha(\omega)\mathrm{E}, \tag{2.17}$$

for a frequency dependent, complex polarisability $\alpha(\omega)$ and oscillating electric field magnitude E. The electric dipole is then given as

$$\mathbf{p} = \left(\mathrm{p}e^{-i\omega t} + \mathrm{c.c}\right)\mathbf{r}_\mathrm{p}. \tag{2.18}$$

For a dipole in an external field, the strength of the potential that it experiences is given by

$$U_\mathrm{p} = -\mathbf{p}\cdot\mathbf{E}. \tag{2.19}$$

However, as the dipole in this case is induced rather than existing prior to an electric field being applied, work must be done in order to create the dipole, which is comparable to separating two masses attached by a spring. Determining this work is done by first noting that the force required to separate the positive and

negative regions of charge within an atom ($\pm q$) is equal to the distance between the centres of these regions, $\delta$, multiplied by some constant $k$, giving

$$Eq = k\delta, \tag{2.20}$$

for energy $E$, and can thus be rearranged for $k$ to give

$$k = \frac{Eq}{\delta}. \tag{2.21}$$

The work done to separate the regions of charge can then be calculated as

$$W = \int_0^\delta F d\delta' = \int_0^\delta \delta' k d\delta', \tag{2.22}$$

which is then calculated to be

$$W = \frac{1}{2}\delta^2 k. \tag{2.23}$$

Then by substituting (2.21) into this expression and by noting that $q\delta$ is the strength of the electric dipole, and that the electric field and electric dipole are colinear, the above expression becomes

$$W = \frac{1}{2}\mathbf{p}\cdot\mathbf{E}. \tag{2.24}$$

Therefore, in accounting for this work, the overall potential becomes

$$U_{\text{eff}} = U_{\text{p}} + W = -\frac{1}{2}\mathbf{p}\cdot\mathbf{E}. \tag{2.25}$$

By considering the form of $\mathbf{E}$, a time average of the above expression can be taken. The electric field present at position $\mathbf{r}$ can be expressed as

$$\mathbf{E}(\mathbf{r}) = \hat{\mathbf{e}}[\mathrm{E}(\mathbf{r})e^{-i\omega t} + \mathrm{c.c}], \tag{2.26}$$

for a real scalar E and frequency $\omega$. Therefore by substituting (2.18) and (2.26) into (2.25) one obtains

$$U_{\text{eff}} = -\frac{1}{2}[\mathrm{E}(\mathbf{r})e^{-i\omega t} + \mathrm{c.c}]\cdot[\mathrm{p}e^{-i\omega t} + \mathrm{c.c}], \tag{2.27}$$

which then simplifies to

$$U_{\text{eff}} = -\frac{1}{2}[\mathrm{pE}(\mathbf{r})e^{-2i\omega t} + \mathrm{pE} + \mathrm{p}^*\mathrm{E} + \mathrm{p}^*\mathrm{E}e^{2i\omega t}]. \tag{2.28}$$

Taking a time average of this $U_{\text{eff}}$ then cancels the effect of the oscillating terms, resulting in a potential of the form

$$U_{\text{dip}} = -\frac{1}{2}(\mathrm{p} + \mathrm{p}^*)\mathrm{E}. \tag{2.29}$$

Using the form of p given in (2.17), the expression becomes

$$U_{\text{dip}} = -\Re(\alpha)\mathrm{E}^2, \tag{2.30}$$

which, when noting that $E^2 = I/2\epsilon_0 c$ for intensity I, then becomes [106, 107]

$$U_{\text{dip}} = -\frac{1}{2\epsilon_0 c}\Re(\alpha)\text{I}. \tag{2.31}$$

This shows that the response of an atom in the presence of such an optical potential is crucially dependent on the frequency of the illuminating light due to the real part of the polarisability $\Re(\alpha(\omega))$ of the atom, which can be calculated using [108]

$$\Re(\alpha(\omega)) = \frac{2}{3(2J+1)}\sum_{i\neq k}\frac{E_i - E_k}{(E_i - E_k)^2 - \omega^2}|\mu_{ik}|^2, \tag{2.32}$$

for a set of known atomic transitions $E_i - E_k = \hbar\omega_{i,k}$, orbital angular momentum $J$ and dipole matrix element $\mu_{ik}$. In the case of $^{87}$Rb , the plot of $\Re(\alpha)$ vs wavelength $\lambda$ is shown in figure 2.7 [107]. $\Re(\alpha)$ is quoted in atomic units (a.u.), with the conversion between S.I. units and a.u. of $\Re(\alpha)_{\text{a.u.}} = \Re(\alpha)_{\text{S.I.}}/(4\pi\epsilon_0 a_0^3)$.

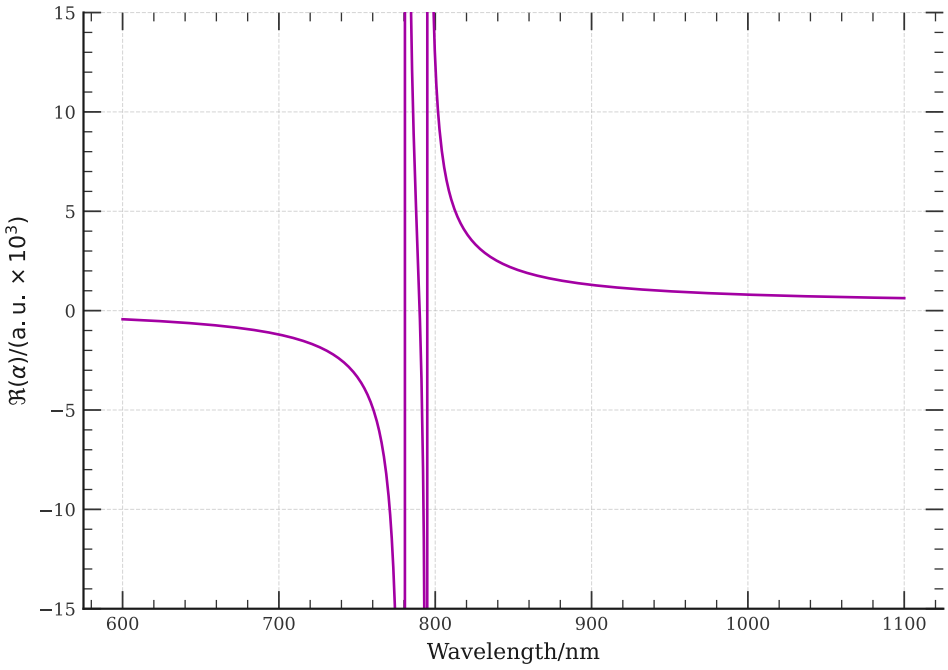


Figure 2.7: Real part of the polarisability $\alpha$ for $^{87}$Rb for both the $D_1$ (on the right, at 794.978 nm) and $D_2$ (on the left, at 780.241 nm) transitions. The conversion between atomic (a.u.) and S.I. units is given as $\Re(\alpha)_{\text{a.u.}} = \Re(\alpha)_{\text{S.I.}}/(4\pi\epsilon_0 a_0^3)$

From this figure, we can see that as $\Re(\alpha) > 0$ is required to create a potential well, a trapping wavelength of $\lambda > 795$ nm is required. Furthermore, as there are only two nearby transitions (the $D_1$ and $D_2$ transitions), the problem can be restricted to consider only these. By restricting (2.32) to only these transition, assuming $|1/(\omega_{D_j} + \omega)| \ll |1/(\omega_{D_j} - \omega)|$ for large detuning, noting that $\omega_{D_j} - \omega = \Delta_{D_j}$

and relating decay rate ($\Gamma_{ki}$) of a transition to its corresponding transition dipole moment ($\mu_{ik}$) via Fermi's Golden Rule [109], the trap depth (2.31) thus becomes

$$U_0 = \frac{3\pi c^2}{2}\left(\frac{1}{3}\frac{\Gamma_{D_1}}{\omega_{D_1}^3\Delta_{D_1}} + \frac{2}{3}\frac{\Gamma_{D_2}}{\omega_{D_2}^3\Delta_{D_2}}\right) \mathrm{I}. \tag{2.33}$$

A plot of $\Re(\alpha)$ restricted to the $\lambda > 820$ nm range, alongside trap depths at past and present trapping frequencies [54, 55, 56] is shown in figure 2.8 for a beam waist of 5 $\mu$m.

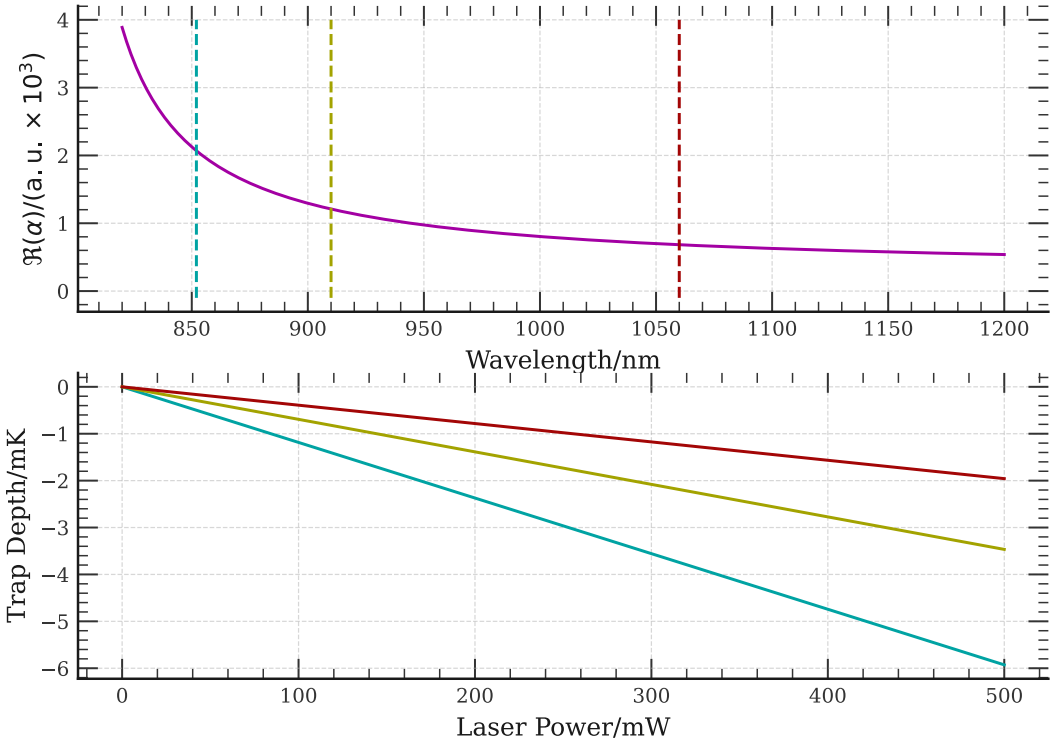


Figure 2.8: $\Re(\alpha)$ vs wavelength for $\lambda > 820$ nm (upper) and trap depths for past and present dipole trap wavelengths (lower) with a 5$\mu$m beam waist. The 910 nm (gold) and 1080 nm (burgundy) traps were used in previous iterations of the experiment and the 852nm (cyan) trap is currently utilised. The dashed lines in the upper plot correspond to wavelengths shown in the lower plot.

From this figure, it may initially seem like the choice of a wavelength closest to the $D_1$ transition is the logical one, as it allows for easier access to deeper potentials. There is, however, an additional quantity that need consideration: the spontaneous scattering rate of atoms with the trapping light [106]. Despite being very far detuned from an atomic resonance, photons from the trapping beam can still interact with atoms. As the dipole trap aims to establish a conservative potential in which atoms remain rather than relying on trapping through momentum transfer, any scattering by the atoms is purely a heating phenomenon. The scattering rate for a

given transition is given in [110] as

$$\Gamma_{\text{Scat},0} = \frac{3\pi c^2}{2\hbar\omega^3}\left(\frac{\Gamma}{\Delta}\right)^2 \text{I}, \tag{2.34}$$

for transition frequency, transition rate and detuning $\omega, \Gamma$ and $\Delta$ respectively. An additional consideration is the diffraction limit of the trapping wavelength, which limits the beam waists of longer wavelength traps.

Thus, due to the fast repetition rate of the experiment described in chapter 3 of $\sim$ 10 kHz and for safer operating powers, a trapping wavelength of 852 nm is utilised with a scattering rate of $\Gamma_{\text{scatt}} = 163\ \text{s}^{-1}$ for a beam waist of 5 $\mu$m and a dipole trap power of 65 mW (in line with the optimised sequence displayed in figure 3.35).

## 2.3 Rydberg Atoms

In section 2.2, the process of exciting $^{87}$Rb to its first excited states of $5\text{P}_{3/2}$ was described, where only the angular momenta $L$ and $J$ were affected. There is, however, significant motivation for looking to excite the principle quantum number $n$ up from $n = 5$, beyond $n = 20$ and to values near ionisation. An atom excited this way, with a large principle quantum number $n$, is referred to as a Rydberg atom. From (2.14), we see that the binding energy asymptotes to zero for $n \to \infty$, meaning ever less energy is required to ionise the excited electron as $n$ increases. This is not the only feature of the atom to change with an increased $n$, and some important properties and their scaling with $n$ are shown in table 2.1 [111, 112].

| Property | $n$ Proportionality |
|---|---|
| Dipole Moment $\langle n, L = a \vert \mathbf{d} \vert n, L = a \pm 1\rangle$ | $n^2$ |
| Radiative Lifetime | $n^3$ |
| Polarisability | $n^7$ |
| Orbital Radius | $n^2$ |
| Binding Energy | $n^{-2}$ |
| Adjacent $n$ State Separation | $n^{-3}$ |
| Resonant Dipole-Dipole Interaction ($C_3$) | $n^4$ |
| Van der Waals Interaction ($C_6$) | $n^{11}$ |

Table 2.1: Table of atomic properties and their corresponding proportionalities to principle quantum number $n$.

The decreasing separation between adjacent $n$ states is of great convenience. The portion of the excitation process (later described in section 2.3.2) up to a Rydberg state where $n$ is increased becomes possible with only a single External Cavity

Diode Laser (ECDL) where one can precisely control its lasing frequency over a wide range of Rydberg states ($35 < n < \infty$ in the experiment described here). Control over the target $n$ state being excited to correspondingly gives control over the parameters listed in table 2.1. Of the quantities mentioned, the dipole moment is of interest in affording tunability of interactions within the Rydberg manifold [112].

### 2.3.1 Rydberg Blockade

Of the quantities listed in table 2.1, only the $C_3$ and $C_6$ coefficients directly dictate inter-atomic interactions. At distances much greater than the atomic radius, these are dominated by the van der Waals interaction $V_{\mathrm{vdW}}$. Though this interaction term scales with $V_{\mathrm{vdW}} \propto r^{-6}$ for distance $r$, per table 2.1 it also scales with $V_{\mathrm{vdW}} \propto n^{11}$, thus for large values of $n$ this becomes appreciable at substantial distances [40, 113]. This effect is quantified by the so-called 'Rydberg blockade radius' [41] given by

$$r_{\mathrm{B}} = \sqrt[6]{\frac{C_6}{\gamma_R}}, \tag{2.35}$$

where $\gamma_R$ is the dominant linewidth of the laser used to excite into the Rydberg manifold [112]. In continuous wave operation, the lower limit of this linewidth is set by the locking scheme, which results in a small Lorentzian frequency spread. In practice, however, this linewidth is often dominated by a power broadening effect whereby $\gamma_{\mathrm{eff}} \propto \Omega_{\mathrm{R}}$ for Rabi frequency $\Omega_{\mathrm{R}}$ [114]. Additionally, for pulsed lasers, the Fourier linewidth can be a limiting factor, but as no lasers were operated this way, the effect is of no import here. The blockade effect can be understood by considering figure 2.9. In this figure, atom $a$ is excited by a laser field of linewidth $\gamma_R$ to a Rydberg state $|R\rangle_a$, and is located at position $r = 0$. Due to the favourable scaling with $n$, the van der Waals interaction of the Rydberg atom $a$ with its surroundings perturbs the energy required to excite a second atom $b$ to state $|R\rangle_b$ as indicated by the purple line. At distances $r < r_{\mathrm{B}}$, this energy shift is greater than the linewidth of the excitation laser, therefore the transition to state $|R\rangle_b$ is blue-shifted off resonance and no excitation occurs. A plot of principle quantum number vs blockade radius $r_{\mathrm{B}}$ is shown in figure 2.10. In this figure, the purple line shows the lower linewidth limit of the locking technique employed for the excitation laser in our experiment. This lock is one where the laser is locked to an ultra-stable high-finesse reference cavity in an evacuated chamber to protect from the effects of thermal and pressure changes [116, 115, 58], with the other two linewidths being present to illustrate the effect of linewidth on $r_{\mathrm{B}}$. The dashed black line shows the radial $1/\mathrm{e}^2$ dipole trap diameter used to prepare atomic clouds for excitation.

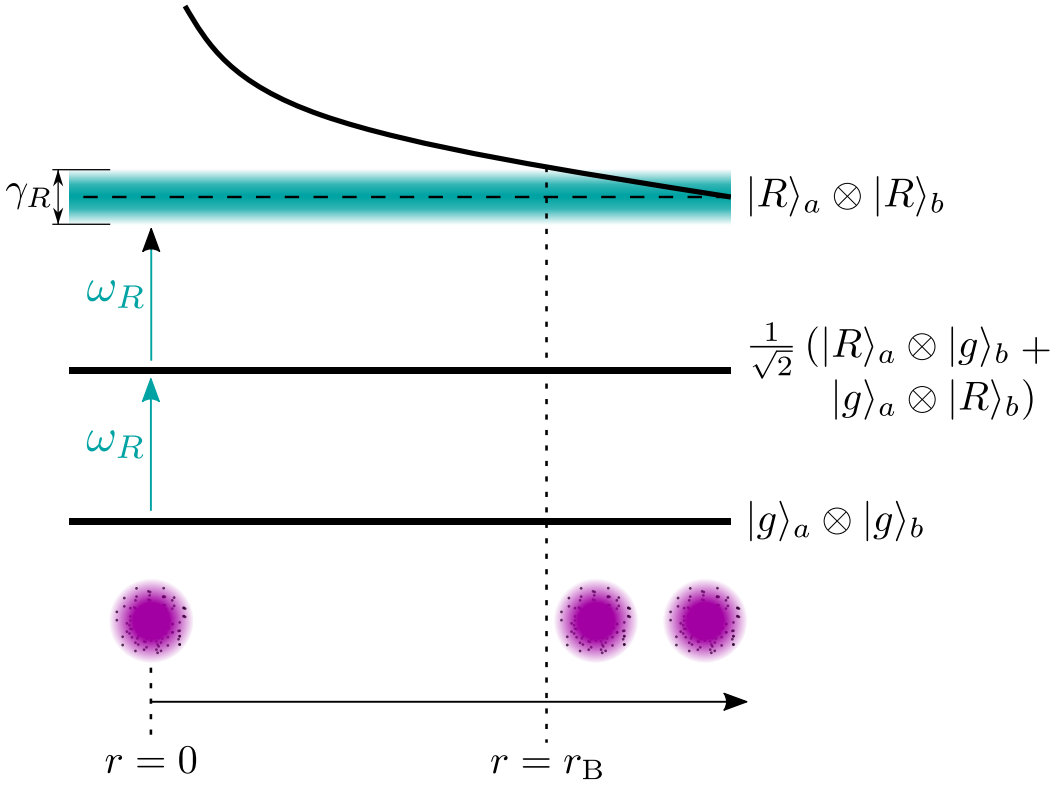


Figure 2.9: The Rydberg blockade mechanism. The van der Waals interaction of the existing Rydberg atom ($|R\rangle_a$) shift the excitation energy required to generate a second ($|R\rangle_b$). At distances from the first Rydberg atom $r < r_B$ this energy shift (solid black) is greater than the excitation laser's ($\omega_R$) linewidth ($\gamma_R$), thus no additional Rydberg atom can form within this radius.

This blockade effect is put to use in our experiment, as experiments are primarily conducted on a single Rydberg exciton. As the axial diameter of the dipole trap used is much larger than $r_B$, without additional confinement as described in N. L. R. Spong's thesis [44], the blockade effect alone is not sufficient to ensure a single exciton forms.

### 2.3.2 Stored Light Polaritons

Assuming a sufficiently cold and dense atomic cloud has been prepared, a coherent excitation of an atom to a long lifetime Rydberg state can occur. In our experiment, an excitation event occurs as shown in figure 2.11.

Prior to any excitation, the collective wavefunction of this cloud is given as

$$|g\rangle = |g_0, g_1, g_2 ... g_i ... g_{\mathcal{N}}\rangle, \tag{2.36}$$

where $g = 5S_{1/2}$ and $\mathcal{N}$ is the total number of atoms in the cloud. The excitation process commences with is a single photon addressing the $D_2$ transition falling

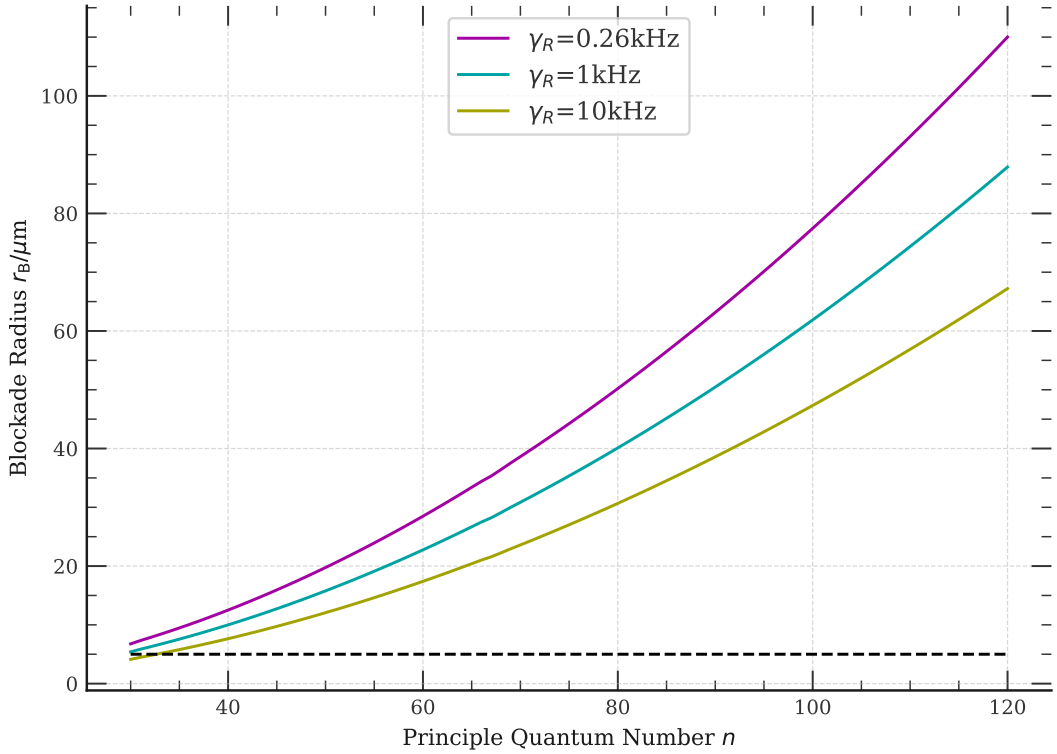


Figure 2.10: Principle quantum number vs blockade radius for excitation laser linewidths of 0.26 kHz (purple), 1 kHz (cyan) and 10 kHz (gold). The dashed black line shows the radial $1/e^2$ diameter of the 852 nm tweezer trap. The lower linewidth limit defined by the purple line is taken from [115].

incident on the atomic cloud. This excites an unspecified atom to the first excited state $e_x = 5P_{3/2}$. As no particular atom is targeted for excitation by the probe beam, the wavefunction for the cloud becomes a superposition over all atoms in the trap, given by

$$|e_x\rangle = \frac{1}{\sqrt{\mathcal{N}}} \sum_{j=1}^{\mathcal{N}} e^{i\mathbf{k}\cdot\mathbf{R}_j} |g_1 g_2 ... e_{x_j} ... g_{\mathcal{N}}\rangle, \tag{2.37}$$

$\mathbf{k}$ and $\mathbf{R}_j$ are the photon wavevector and atom position respectively. By ensuring that the 480 nm coupling beam is switched on before a photon is injected into the cloud, the excited atom will be excited up to a Rydberg state $R = nS_{1/2}$ before the decay $|e_x\rangle \rightarrow |g\rangle$ can occur. Thus, the atom is excited to a Rydberg state [117]

$$|R\rangle = \frac{1}{\sqrt{\mathcal{N}}} \sum_{j=1}^{\mathcal{N}} e^{i\mathbf{k}\cdot\mathbf{R}_j} |g_1 g_2 ... r_j ... g_{\mathcal{N}}\rangle. \tag{2.38}$$

As this Rydberg atom exists as a superposition over all atoms present, it becomes robust to atom loss as per-atom effect on coherence and state population drastically decreases. Once this collectively stored excitation is created, a variety of experiments can be performed, taking advantage of the long-lived Rydberg states and

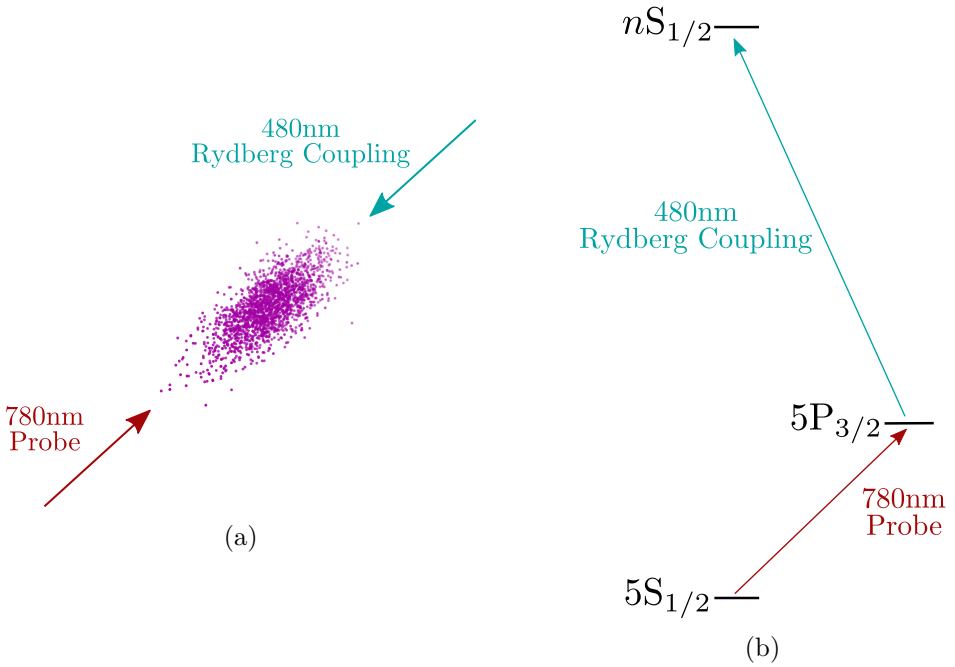


Figure 2.11: A weak 780nm probe beam excites an unspecified atom in an atomic cloud to state $5P_{3/2}$ whilst being illuminated by a coupling beam addressing the transition $5P_{3/2} \rightarrow n_{1/2}$. **(a)** shows the two counter-propagating beams addressing the atomic cloud and **(b)** shows the energy level diagram of the process.

large dipole moments within the Rydberg manifold [118, 44]. At the end of an experimental sequence, the Rydberg coupling laser is re-illuminated and the collectively encoded excitation is coherently transferred back down to $|e_x\rangle$, at which point the initially stored 780nm photon is re-emitted. As the phase information in the wavevector is retained throughout the excitation process (exponent in (2.38)), the probe photon is coherently re-emitted and as such it's path can be predicted and aligned with a single photon counting device such as a Single Photon Avalanche Diode (SPAD). Only a single state $|R\rangle$ is coupled back down to the lower lying states so if a transfer to an adjacent Rydberg state occurs, there will be an incomplete transfer of population back to $|e_x\rangle$. Thus, the observable in our experiment is the probe photon after an experimental sequence has concluded. Aside from the maintenance of overall coherence of the Rydberg excitation, the probability of observing this probe photon is dependant on the degree to which the atom is transferred out of the coupled Rydberg state.

Despite the advantages of collective encoding mentioned, several limiting factors persist in reducing the lifetime of these collective excitation such as AC-Stark shifts induced by laser intensity and atomic motional noise, as well as collisions with background gas [119]. Nonetheless, at a background pressure of $10^{-10}$ mbar

and a temperature of 50 $\mu$K, the effective lifetime due to these effects (excluding the radiative lifetime) is $\sim$ 2 s [119]. As will be detailed later in chapter 3, the experiment described here boasts a high repetition rate of 10 kHz making this lifetime ceiling more than sufficient for our purposes.

As mentioned in section 1.3, qutrits present advantages compared to qubits for certain applications. One of these aforementioned applications is secure communication. At present, qutrits have been experimentally demonstrated on a variety of platforms such as individual cold atoms in states outside the Rydberg manifold [120], CQED [121], Nitrogen Vacancy centres [122], trapped ions [123] and superconductors [69]. Implementations of qutrits using Rydberg atoms at time of writing, however, has been limited. Instead, Rydberg states have been of primarily considered as either a qubit state [124] or an auxiliary state used solely to mediate interactions between qubits [125].

In a separate vein, past investigations on the apparatus described in chapter 3 focused on demonstrations of long range interactions between adjacent collective excitations [56]. Motivated by this, the long term goal of this project would be to generate two Rydberg excitations, each of which serving as a qutrit, and demonstrate a transfer of quantum information between them. The first stage of this is to generate a single qutrit and perform unitary operations on this in isolation. The following chapter details the experimental apparatus required to perform these proposed experiments on ultra-cold Rydberg ensembles, and the processes undertaken to progress towards experimental readiness for future investigations.

# 3 | Experimental Apparatus

As stated in section 1.2, the experimental apparatus used in the Rydberg Quantum Optics research group has gone through multiple iterations. The current setup consists of the following elements crucial to experimentation:

**A laser system** where active frequency correction is employed to achieve the narrow linewidths necessary to address atomic transitions in a controlled manner.

**A vacuum chamber** suitable for Ultra-High Vacuum (UHV) conditions in which atoms can be cooled to $\mathcal{O}(10\ \mu\text{K})$ and studies on Rydberg atoms can be performed.

**Control hardware** with which the frequencies and intensities of the laser light being employed can be varied throughout an experimental sequence.

**Control software** to pre-program the control hardware to actuate at the correct times during a sequence.

The equipment for the current generation of the experiment was designed and assembled by S. Ball and H. Busche [57, 56], the setup described here boasts only modest alterations. These are:

- The replacement of the gate valve between the upper and lower chambers with a cross shaped pipe containing windows through which a probe beam could be shone.
- The substitution of the original upper 2D MOT cell with a new, shorter and non Anti Reflection (AR) coated, cell.
- The addition of focusing optics to compensate for the lack of AR coating on the upper cell.
- The reconstruction of the laser system (with the exception of the locks) to streamline and simplify the design for ease of usage.

This chapter begins by describing the equipment used for experimentation: the laser systems, vacuum components and control equipment. Following this, the process by which the experiment was returned to UHV conditions following an unplanned vacuum break is described before, finally, the optimisation of the initial cooling stages are outlined.

## 3.1 Lasers

In order to coherently induce atom-light interactions in an experiment, having precise control of frequency and intensity of laser light being utilised is imperative. As such, frequency locking and optical intensity control are implemented. This section details the methods used to achieve this necessary control.

### 3.1.1 Overview

The choices of laser utilised in this experiment are informed by the two main tasks required in a sequence: atom cooling and trapping and excitation to Rydberg states. To achieve the former, three lasers are required: one each to address the cooling and repump transitions, and one to form the FORT trap. For the two-step Rydberg excitation process utilised here, only one additional laser is required due to the excitation in the first step being induced by the laser used for atomic cooling. The beam diagram for the cooling and repump lasers is shown in figure 3.1. Details on the lasers, optical channels and locking techniques are given in later sections.

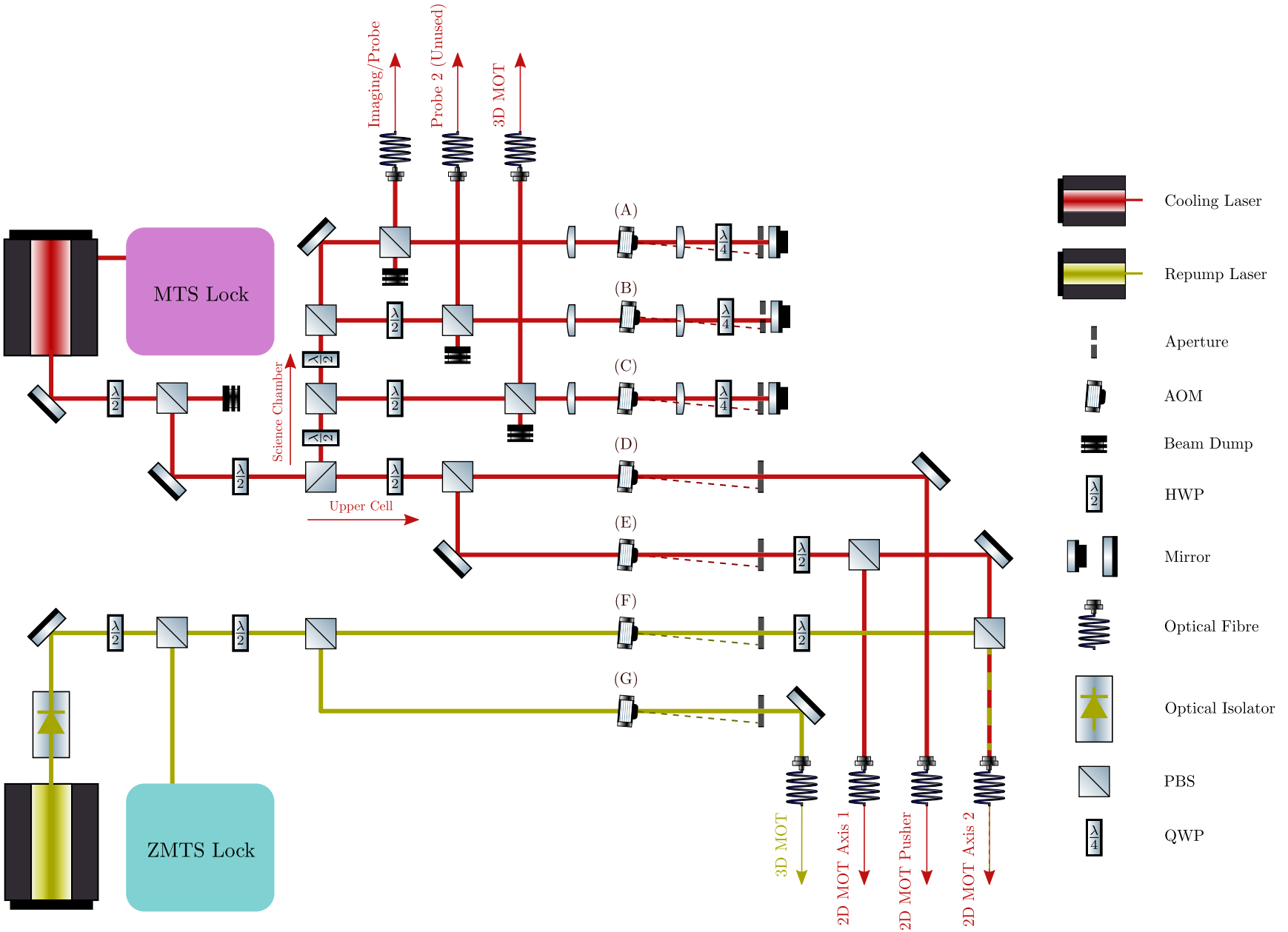


Figure 3.1: Beam diagram showing the optical setup of the cooling and repump lasers. The Acousto-Optic Modulator (AOM) channels (A-G) shown here correspond to those listed in figure 3.4.

### 3.1.2 Cooling Laser - 780 nm

The laser used to address the $|F = 2\rangle \rightarrow |F' = 3\rangle$ transition is a commercial 780.241nm Bragg Grating ECDL*. The output from this comparatively low-power diode ($\sim$ 80 mW) is fed into a Tapered Amplifier (TA)†, capable of a higher 2.4 W output. Back reflections into the ECDL are prevented by in internally mounted optical isolator, with a second internally mounted isolator placed after the TA to prevent back reflections into the amplifier. This output light is split downstream by using Half Wave Plate (HWP) and Polarising Beam Splitter (PBS) pairs to control the powers reflected and transmitted through the beam splitters. Light from the main beam output is split for two probe channels, 2D and 3D MOT cooling and a red detuned pushing beam. The second probe channel was designed to be implemented in two site experiments for the study of Rydberg-Rydberg interactions [126], thus was not used in this work. Furthermore, as the effect of the pushing beam was not characterised, it's description is also not included in this work. The 2D cooling light is split after passing through an AOM before the light for each axis is passed through a polarisation maintaining fibre to the main experiment. The cooling light for one of these axes (axis 2 in figure 3.1) is combined colinearly with repump light and passed into the same fibre. The 3D cooling light is combined with repump light by a bespoke two-input three-output fibre splitter‡ adjacent to the main vacuum chamber. The detunings for the different channels are detailed in section 3.1.6. An auxilliary output from the ECDL before amplification is utilised to lock the laser using the Modulation Transfer Spectroscopy (MTS) locking technique [127, 128]. The laser is locked 140 MHz below resonance with a double pass AOM.

### 3.1.3 Repump Laser - 780 nm

As shown in figure 2.2, the ground state splitting of the hyperfine $|5S_{1/2}, F = 1\rangle$ and $|5S_{1/2}, F = 2\rangle$ states is several GHz wide. This sizeable splitting makes it impossible to address both the cooling and repump transitions with a single laser source, thus a second laser is dedicated to this task. We use a second commercial ECDL§ capable of outputting 90 mW at 780 nm after replacing the original diode¶ with a new one‖. An external optical isolator is used to prevent back reflections into the diode, and is depicted in figure 3.1. Unlike the cooling photonic channels,

*Toptica DL Pro
†Toptica TA Pro
‡Manufactured by Evanescent Optics
§Toptica DL Pro
¶Toptica LD-0790-0120-AR-1
‖Toptica LD-0790-0120-AR-2

the repump light used is kept exclusively on resonance as the only requirement of the repump laser is to efficiently transfer atoms back into the $|5S_{1/2}, F = 2\rangle$ state. There is, however, a requirement for switching of repump light during a sequence. Thus the repump light is split into two channels, one each for the 2D and 3D MOTs, and passed through AOMs to actuate this switching. To keep the repump light resonant, a small fraction of light is split from the main beam after the isolator and is passed into a tunable Zeeman Modulation Transfer Spectroscopy (ZMTS) locking scheme [129], which is a modified version of conventional MTS, at 78 MHz below resonance. This frequency is chosen to align with a crossover resonance 78 MHz below the repump transition, giving a reliable and unmoving frequency offset. Further details of the AOMs utilised is detailed in section 3.1.6 below.

### 3.1.4 Rydberg Excitation Laser - 480 nm

The second step in excitation to a Rydberg state after the initial $|5S_{1/2}\rangle \rightarrow |5P_{1/2}\rangle$ excitation is to drive the $|5P_{3/2}\rangle \rightarrow |nS_{1/2}\rangle$ transition into the Rydberg manifold as depicted in figure 2.11. To achieve this, a 480 nm Second Harmonic Generation (SHG) laser* capable of outputting 1.2 W is utilised. This laser system is constituted by internally mounted ECDL† and TA‡ and SHG bow-tie cavity.

One of the attractive features of Rydberg atoms is the long radiative lifetimes, allowing for prolonged study of coherent dynamics [118]. This advantage can, however, be seen as a double edged sword, as by having comparatively long lifetimes, the resonances of the $|5P_{3/2}\rangle$ state into the Rydberg manifold are very narrow, as shown in figure 3.2. Values of linewidths were obtained using the ARC python library [130]. As such, to address such narrow transitions one needs to be able to lock this laser to a narrow resonance for high $n$, and do so in a frequency range without easy access to atomic transitions. In the past, this has been achieved in our experiment using EIT spectroscopy [57, 131], however this is now achieved using a Pound-Drever-Hall (PDH) lock on an evacuated ultra-stable, high-finesse cavity [132, 116].

*Toptica TA-SHG Pro
†Toptical DL Pro
‡Toptica TA Pro

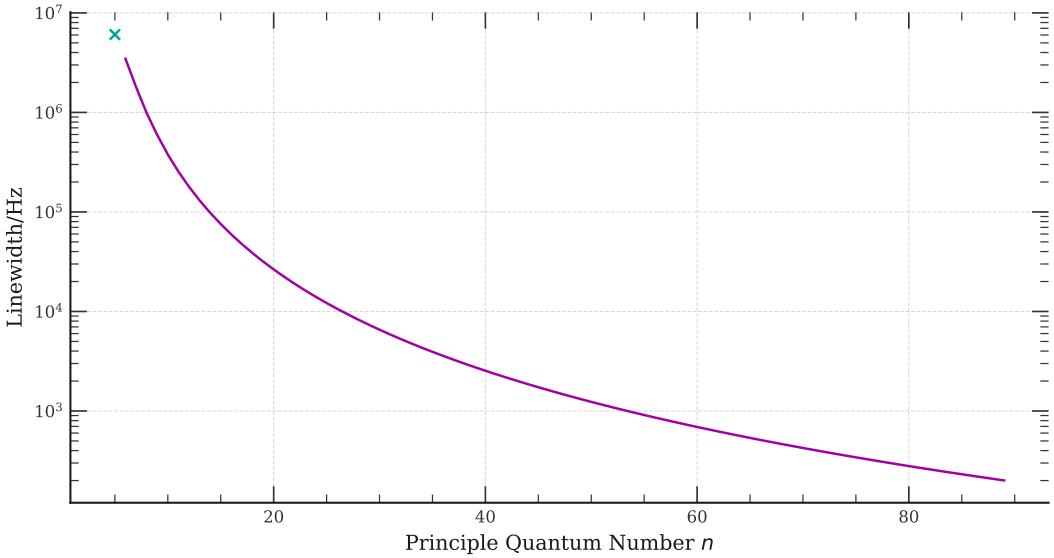


Figure 3.2: Principle quantum number $n$ vs linewidth $\Gamma_n$ of transition $|5P_{3/2}\rangle \rightarrow |nS_{1/2}\rangle$. The cyan cross in the top left of the plot shows the linewidth of the $|5P_{3/2}\rangle$ state. Values of linewidths were obtained using the ARC python library [130].

### 3.1.5 Dipole Trapping Laser - 852 nm

As detailed in section 2.2.2, an additional laser is required to set up a FORT. In our experiment, this is an 852 nm TA* seeded by an ECDL†. As this emits at a wavelength extremely far from any atomic resonances, the frequency fluctuations that would be eliminated by locking the laser have no substantial impact on dipole trap depth, thus this laser is not locked.

### 3.1.6 Intensity and Frequency Control

In this experimental setup, laser intensities and frequencies are controlled with AOMs. The crucial elements of these components are a crystal and piezoelectric transducer. By applying a high voltage AC electric field on the piezoelectric transducer whilst in contact with the crystal, a sound wave can be generated across the medium [133]. This sound wave then induces Brillouin scattering and the crystal acts as a diffraction grating with frequency modes

$$\Delta f = \frac{nc\lambda}{2\eta c_s \sin(\theta)}, \tag{3.1}$$

for refractive index and speed of sound through the medium of $\eta$ and $c_s$. By utilising these diffracted orders downstream in the experiment, one can control the

*Toptica TA Pro
†Toptica DL Pro

laser powers in each optical channel by controlling the electrical power supplied to each AOM.

Due to the fast repetition rate of the experiment, the change in optical output from the AOMs cannot be assumed to be instantaneous and needs to be accounted for. The rise and fall of optical power can be well modelled as a sigmoid error function of the form

$$s_{err}(t) = \frac{1}{2}\left[1 + \mathrm{erf}\left(\frac{t - t_0}{\sigma_t}\right)\right] \tag{3.2}$$

where $\sigma_t = r_{10:90}/1.163$ and $r_{10:90}$ is the 10%-90% rise time. An example pulse for $r_{10:90} = 10$ ns is shown in figure 3.3. The other important factor of the AOMs is

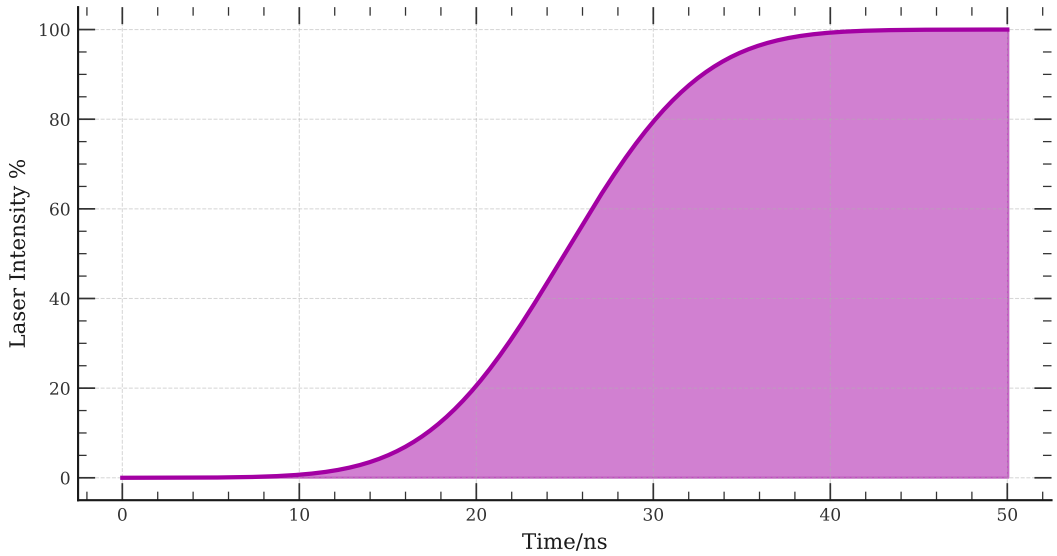


Figure 3.3: Example AOM intensity change for a rise time $r_{10:90} = 10$ns.

of course the frequency detuning they induce in the incident beams. As shown in figure 3.1, AOMs (A-C) are arranged in a double-pass configuration, unlike AOMs (D-G) which are set up for only a single pass. The double-pass AOMs are set up this way due to inter and intra repetition frequency changes, which are achievable without much loss for double-pass configured AOMs as the retro-reflected beam remains anti-parallel to the outgoing beam regardless of input frequency. This means that in the case of perfect alignment, coupling into a fibre should not be affected by a change in frequency. The single pass AOMs are configured so to maintain an efficient conversion ratio of input to frequency shifted light, as there is no need to change frequencies for these AOMs during or between repeats. A diagram showing the detunings for AOMs (A-E) is shown in figure 3.4. In this diagram, the laser of frequency $\omega_C$ is locked 140 MHz below resonance and positively detuned (gold frequencies) back up toward resonance. The black frequencies show the detunings from the $D_2$ resonance for each AOM (A-E). AOM (A) is used for three purposes:

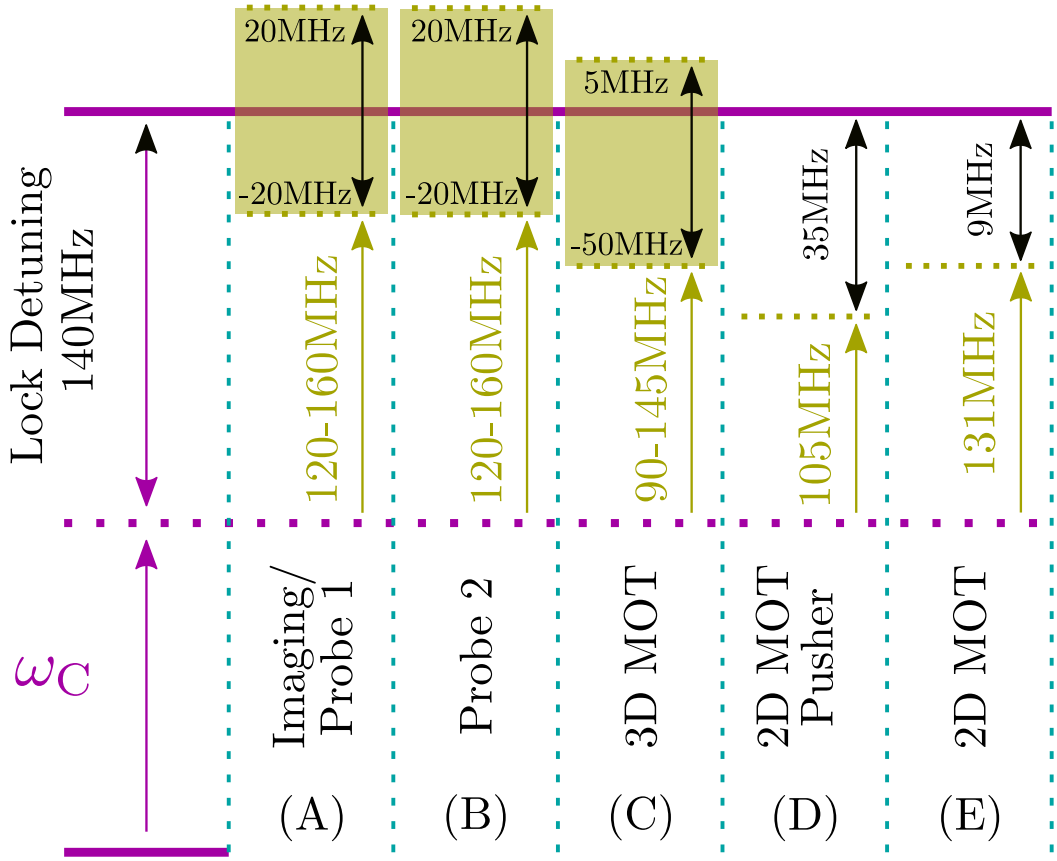


Figure 3.4: AOM frequencies with lettered labels corresponding to the AOMs shown in figure 3.1. $\omega_C$ is the cooling frequency output by the cooling laser, which is locked 140 MHz below resonance (lock detuning). The frequencies in gold show the input frequencies for each AOM and the black frequencies show the resulting detunings from resonance. AOMs (A-C) are set up in a double-pass configuration to allow for inter and intra repetition frequency variation. AOMs (D-E) are arranged for only a single pass, thus output a constant frequency at all times. AOMs (F-G) are not shown here, as both are locked below resonance and set up for a single pass to exclusively shift back up to resonance.

absorption imaging as described in section 3.4.2, the first step in the two-step excitation of an atom to a Rydberg state as described in section 2.3.2 and dipole trap characterisation. This last usage is not detailed here, and can be found in [126]. As previously stated, AOM (B) is used for past two site experiments [126, 132], thus went unused in this work. Regardless, the scanning range is the same as (A), as characterisation of the second trap was required in the same fashion as the first. AOM (C) provides the detuning for the 3D MOT cooling light, which changes multiple times in a single run (see sections 3.2.3 and 3.4.3 for details) in addition to the intensity variation required throughout. AOM (D) provides the detuning of the red-detuned pushing beam. This component was not properly characterised and subsequently utilised in the preparation of this work, thus precluding any ex-

ploration here. AOM (E) provides frequency and intensity control to both axes of the 2D MOT, which are split for separate fibre channels after the AOM frequency shifting.

AOMs (F-G) are not shown here as they exclusively shift the light back onto resonance for the repump transition. AOMs that achieve the same purpose of detuning and shifting back onto resonance to provide intensity control are employed for the 480 nm Rydberg excitation laser, but are not shown here. Additionally, the 852 nm FORT is intensity controlled via an AOM, but as no locking is present for that beam, this shift is not in reference to a specific transition.

Once passed through the AOMs and into polarisation maintaining optical fibres, the light described above is sent to the main experimental apparatus. The following section details this setup, and how an experimental sequence is implemented.

## 3.2 Experimental Design

Our experimental apparatus in which cold atom experiments are performed was primarily designed by Hannes Busche and Simon Ball [126, 57], where 3D designs of the setup are presented. It consists of a 2D MOT which cools atoms from thermal temperatures horizontally to form a cold beam before being transferred by either gravity or gravity + pushing beam to the science chamber. Here, atoms are trapped and cooled to $\sim 50\ \mu$K before a Rydberg excitation and further experimentation is performed. This section details the equipment and techniques used to achieve this, as well as details on how a sequence is controlled and a typical cooling sequence.

Following an unforeseen vacuum break in early 2022, components were changed from Busche and Ball's original design. Aside from equivalent substitutions (atom dispensers and an electrode feedthrough) a gate valve separating the upper and lower chamber was removed and replaced with a cross shaped DN40 vacuum tube (see figure 3.12) and the glass 2D MOT cell was changed. Though the absence of the gate valve required no adjustment to experimental operation, the change in 2D MOT cell required significant changes and are detailed in section 3.2.1 below.

### 3.2.1 Upper Cell

Prior to ultra-cold atom trapping, one needs to undertake the task of preliminary cooling from thermal temperatures and transporting atoms to the main experi-

mental trap. This is typically achieved by one of two methods: Zeeman slowing [134, 135, 136, 137] and 2 dimensional MOT trapping (2D MOT) where traditional MOT cooling is applied in two cardinal directions only to generate a cold beam [138]. Superficially a main advantage of Zeeman slowing, high slow-atom flux, appears to align well with the high repetition rate of our setup [139]. There are, however, some significant drawbacks that outweigh this advantage. Firstly, this slowing technique results in a large background pressure [140], which itself has to be mitigated. This is typically done with an *in-vacuo* mechanical shutter to physically block off the initial cooling stage from the science chamber, but can result in mechanical vibrations to which atomic clouds can be extremely sensitive [141]. This is not to say that this issue can't be overcome, as van der Stam *et. al.* [136] show. Furthermore, though the absolute atom flux may be lower from a 2D MOT, the number of atoms loaded into an optical trap can be made comparable between the two methods [139]. A feature of note in our setup compared to others [142, 143] is the vertical arrangement of the cell with a red detuned pushing beam. Though a horizontal arrangement was initially considered in 2016, for safety concerns and for ease of optical access along the dipole trap axis (see section 3.2.2), a vertical arrangement was constructed. As atoms naturally fall under gravity toward the science chamber, a blue detuned pusher beam for the purposes of providing sufficient velocity to atoms in the direction of the main trap was not necessary; instead, the pushing beam is red detuned to retard upward moving atoms as the atomic dispensers release atoms at thermal temperatures from a cup facing vertically upwards. Following the vacuum break in early 2022, the upper chamber was reconstructed with a new glass cell, which required adjustments to the optics utilised. The two key differences between the previous and current cells are no AR coating on the new cell and one fewer cooling volume (three down from four) due to a reduction in cell height. The vertical and horizontal cross sections of the upper chamber are shown in figure 3.5.

In the upper cell, 2D MOT light of $1/e^2$ diameter = 9 mm is split between three cooling volumes using HWP-PBS pairs and circularly polarised with Quarter Wave Plate (QWP)s. Following the change in upper cell to one with no AR coating, long focal length (1 m) focusing optics were added (lenses after the QWPs in figure 3.5) to ensure that the laser intensity remained constant between the outgoing and returning beams. Further details on the choice of optics can be found in Oliver D. W. Hughes' upcoming thesis, but the effect of these optics was characterised and is detailed in section 3.4.1. Two strips of seven permanent magnets* each provide a constant field of 16 G/cm the way down the chamber. Atoms are released into the chamber from the cup dispensers located at the bottom of the chamber and

*Eclipse Magnets N750-RB

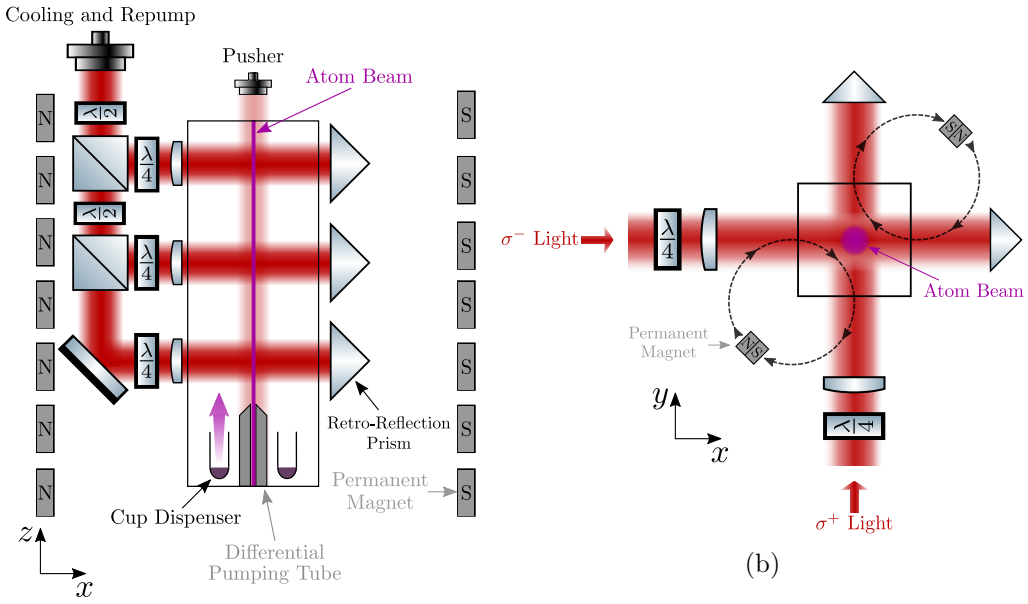


Figure 3.5: Upper cell diagrams in the $x-z$ **(a)** and $x-y$ **(b)** planes. **(a)**: Light is split between the three cooling volumes with HWP-PBS pairs. Light is then circularly polarised to address specific angular momentum projection $|m_F\rangle$ states and passed through the cell. The light is then retro-reflected using a total internal reflection glass prism which, in addition to efficiently reflecting the incoming light, provides a $\frac{\pi}{2}$ phase shift to the incoming light thus ensuring the atoms see the same circular polarisation in both the outgoing and retroreflected beams. **(b)**: The magnetic fields, and corresponding circular polarisations to drive the red-detuned Zeeman split $|m_F\rangle$ states, are displayed for each axis.

shaped into a beam by the three cooling volumes. They then pass through the narrow aperture (0.8 mm diameter) differential pumping tube. This differential pumping tube is utilised to help prevent a build up of vapour pressure in the lower chamber by background atoms released from the dispensers, keeping them confined to the upper chamber. Once passed out of the upper cell, cold along both horizontal directions, the atoms fall into the science chamber for further cooling and experimentation.

### 3.2.2 Science Chamber

In order to experiment on atomic samples at low temperatures, an optically accessible chamber capable of maintaining UHV conditions of the order $\mathcal{O}(10^{-10}\text{mbar})$ is required. The chamber utilised is a stainless steel, non-magnetic spherical octagon* allowing for optical access via eight viewports (with two additional viewports

*Kimball Physics MCF600-SphOct-F2C8

along the $y$ axis). A cross section of the chamber in the $x-z$ plane, as well as light sources of import, is shown in figure 3.6. The vacuum chamber provides optical

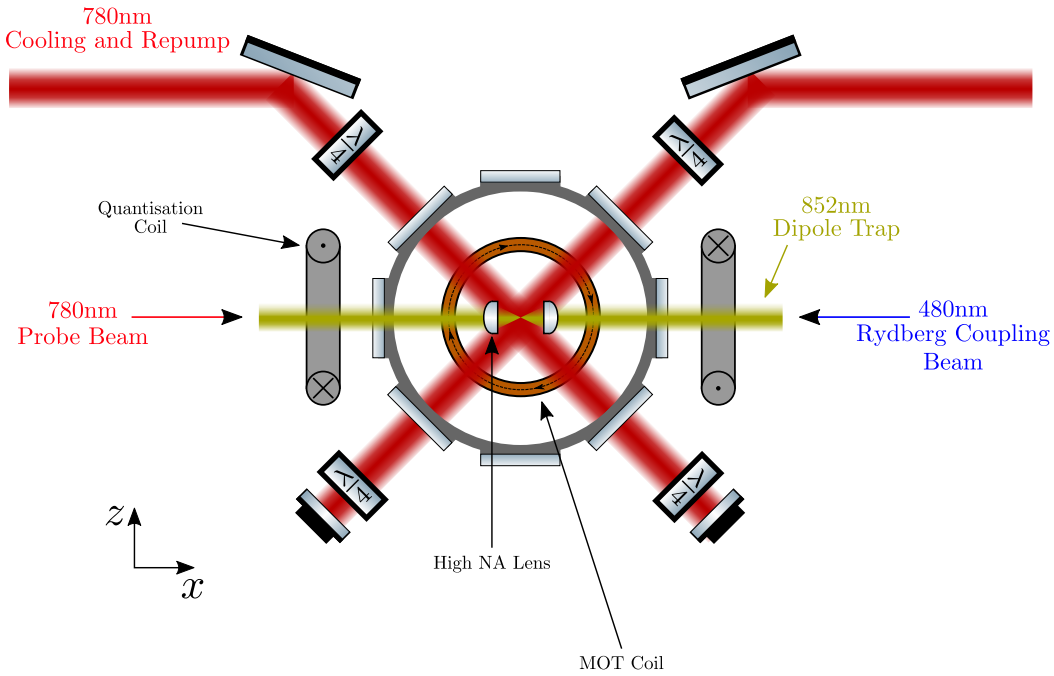


Figure 3.6: Cross section of the science chamber in the $x-z$ plane. The vacuum chamber provides optical access via the eight viewports shown, as well as two additional viewports along the $y$ axis. MOT beams are passed through the diagonal viewports to leave the horizontal axis free for the 852 nm FORT tweezer trap which is focused down with a pair of high NA (NA=0.5) lenses. The beams utilised in the Rydberg excitation sequence described in section 2.3.2 are also shone down this axis. *In-vacuo* MOT coils (copper ring) are used to generate a strong magnetic field (35G/cm) close to the atoms with a current indicated by the dashed black line. *Ex-vacuo* Helmholtz quantisation coils are used to provide a quantisation axis during state preparation for Rydberg excitation.

access via the eight viewports shown, as well as two additional viewports along the $y$ axis. MOT beams are passed through the diagonal viewports to leave the horizontal axis free for the 852 nm FORT tweezer trap. Horizontal rectangular-line shaping masks are placed on the upper MOT viewports to restrict the MOT size and reduce scatter off *in-vacuo* components. The tweezer trap employs a pair of high NA lenses (NA = 0.5, working distance = 7 mm) separated by 14 mm to focus the dipole trap light down to a beam waist of $w_0 = 4.5 \pm 0.3$ $\mu$m [57]. The lenses are cut (not shown here) to allow the MOT beams to pass The beams utilised in the Rydberg excitation sequence described in section 2.3.2 are also shone down this axis. *In-vacuo* MOT coils (copper ring) are used to generate a strong magnetic field (35 G/cm) close to the atoms, with a coil current as shown by the black dashed line. The *ex-vacuo* Helmholtz-configured quantisation coils are used to provide a

quantisation axis for the purposes of atomic excitation in Rydberg atom formation, as well as for any transitions induced within the Rydberg manifold. Additionally, *ex-vacuo* Helmholtz configured shim coils are used to move the magnetic field zero point in order to fine-tune the overlap point of the cooling beams and magnetic field minimum.

Though the high NA lenses and MOT coil are shown in figure 3.6, additional *in-vacuo* components are employed to study Rydberg dynamics. These are shown in the $y-z$ cross section of the science chamber shown in figure 3.7. The MOT

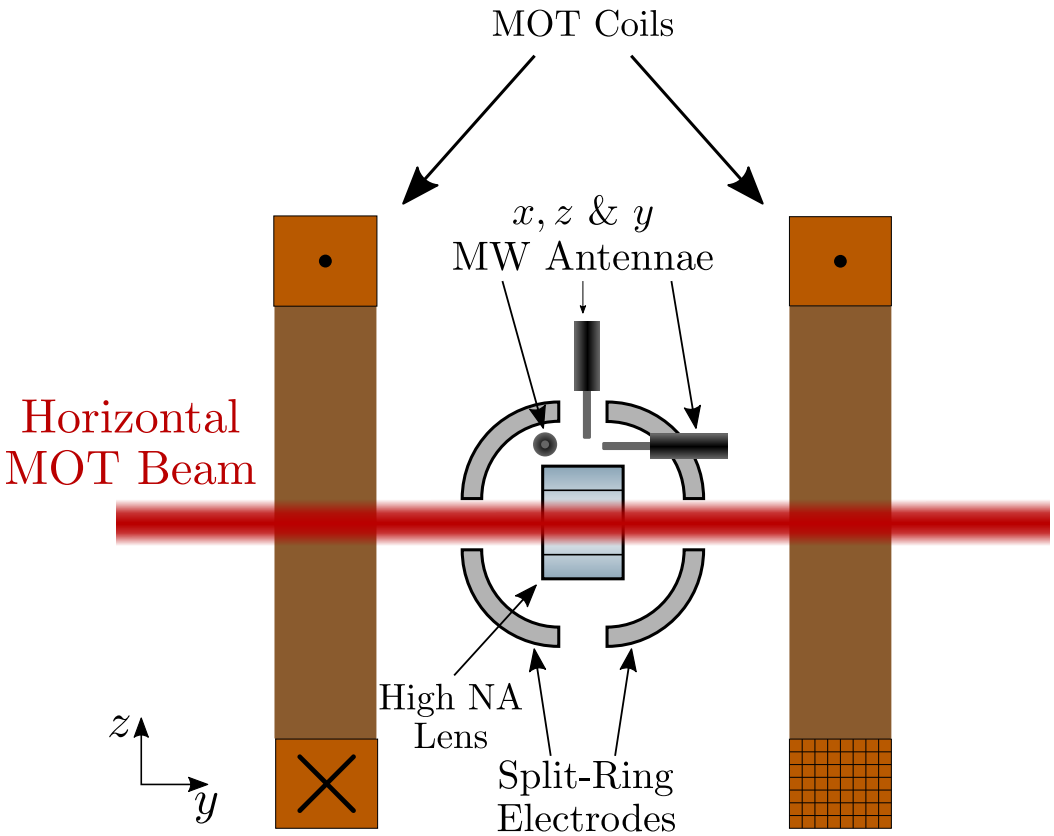


Figure 3.7: Cross section of the science chamber in the $y-z$ plane showing *in-vacuo* components. Adjacent to each high NA lens is a quartet of DC split-ring electrodes (for a total of eight). Between the lenses are a set of three microwave stub antennae designed for a frequency range of DC − 40GHz. The rectangular MOT coils are shown in copper-orange, with the bottom right cross section split to show the 8x7 grid arrangement of the coils.

coils shown here are each composed of a set of 55 square wires wound in a 7×8 grid, with one wire missing from the grid in each in order to connect between each coil cluster and to external feedthroughs. Between the high NA lens pair are two key components of interest. The first is the quartet of split-ring electrodes adjacent to each lens (for a total of eight electrodes). These are used to generate

DC fields in any superposition of the three cardinal directions as has been implemented elsewhere [144, 145]. The second component of interest is the set of three microwave stub antennae oriented parallel ($x$) and perpendicularly ($y$) to the quantisation axis defined by the quantisation coils shown in figure 3.6 as well as vertically ($z$). These 16 mm antennae are each designed to output microwave fields in the frequency range DC − 40 GHz with the antenna length intended to produce a quarter-wave stub antenna, for linear polarisation in the plane of emission [146], at 18.5 GHz. By driving phase-controlled microwave fields through these antennae*, one can coherently address high-lying Rydberg transitions in the manifold near ionisation. As these Rydberg-Rydberg transitions have exceptionally large dipole matrix elements, generating Rabi frequencies $\mathcal{O}(10\text{ MHz})$ where $\pi$ pulses occur on nanosecond timescales (at the limit of our AOM rise times) is quite achievable [58, 44, 126].

In order to take advantage of the nanosecond timescales that the equipment described above is capable of operating at, one needs to employ control technology capable of driving such an experiment. The experimental control hardware and software used to achieve this are described in section 3.2.3 below.

### 3.2.3 Experimental Control

Like many other experiments in the Quantum Light and Matter group at Durham University, the experimental apparatus described in this chapter is controlled by the LabView virtual interface: Durham Experimental Terminal (DExTer) [147]. The software front-end of DExTer splits an experimental sequence into discrete timesteps of length specified by the user. In each timestep, one can address either digital or analogue voltage outputs to address physical actuators. In this experiment, digital controls are used to switch: single-pass AOMs, quantisation coils, 3D shim coil voltages and any diagnostic triggers. As DExTer was originally designed with a timing resolution of $\approx 800$ ns [147], heavy modifications were made to allow for a set of fast digital outputs addressable in 5 ns increments [57]. This allows for further control over the microwave sources, SPAD arrays and probe AOMs. After an initial calibration with the component in question, the analogue voltage outputs are used to control the double-pass AOM powers and frequencies and 3D MOT coil currents.

In order to address components at each timestep, DExTer controls an Field Pro-

*From MW Sources: Anritsu MG3696A and Agilent E8257D PSG

grammable Gate Array (FPGA)* with 96 digital in/outputs, and 8 each of analogue inputs and outputs. This FPGA is configured to read instructions step-by-step in an experimental sequence specified with DExTer, varying the voltages for each of the digital and analogue outputs in a fashion akin to an interpreted coding language. In keeping with this comparison to coding languages, in order to achieve the speed-up needed to address components on 5ns timescales a shift from an 'interpreted' to a 'compiled' type instruction set is made. This is implemented by pre-loading a fast sequence, labelled a 'sub $\mu$s' sequence in DExTer, onto the FPGA's RAM and the FPGA is overclocked from 40 MHz to 200 MHz. This restricts the range of operations significantly [57], and control of only 16 digital outputs during a sub $\mu$s sequence is possible.

Despite being an integral part of the experimental apparatus, thus warranting a description here, no results described in this work make use of the fast digital controls or indeed photon counts from the aforementioned SPAD arrays. This was partially caused by unfortunate damage to the brittle ceramic insulation of one of the split-ring electrode feedthroughs that resulted in an unplanned vacuum break. Section 3.3 below details the process of restoring the experiment to UHV conditions suitable for ultra-cold Rydberg experiments.

## 3.3 Ultra-High Vacuum Setup

In order to effectively conduct experiments on atoms that maintain quantum dynamics throughout, a great deal of environmental control is required. The most significant of these control measures is the evacuation of the chamber in which experiments are conducted to prevent scattering of atoms of interest. The relationship between trap lifetime and pressure is inversely proportional to pressure [148] with dipole traps existing with lifetimes of nearly a minute at background pressures of $10^{-10}$ mbar [119]. Thus, maintaining a vacuum of sufficient quality is vital to perform experiments even on $\mu$s timescales. In early 2022 the ceramic insulation on an electrode feedthrough on the main chamber cracked, causing the experiment to be brought up to atmosphere. This section details the component preparation, characterisation (where appropriate) and installation as well as all stages of the re-evacuation process to return the apparatus to a state of experimental readiness.

*National Instruments PCIe 7842R

### 3.3.1 Main Tasks

The main tasks to be completed before beginning the re-evacuation process were as follows:

1. Source and replace the broken feedthrough alongside the Rubidium dispensers.
2. Clean any dirty vacuum facing components.
3. Characterise the ion pump maintaining the vacuum in the system

After these tasks were performed, the re-evacuation process constituted:

1. Initial pump down and leak test.
2. A bake out to clear the chamber interior.
3. A further leak test and leak sealing.
4. A second bake out and leak check.
5. Ion pump conditioning.
6. Dispenser activation
7. A final third bake out.

Due to an error in the dispenser activation (section 3.3.8), a second bakeout was required and the above steps were repeated. As most of the implementation was near identical between the occasions, figures and pictures can be assumed to be for the first evacuation only unless stated otherwise.

### 3.3.2 Components

One of the in-vacuo components used to manipulate Rydberg atoms in the experiment is the split-ring DC electrodes surrounding the aspheric lenses at the centre of the chamber. These electrodes allow for the induction of Stark shifts into atomic energy levels as well as to simulate noise for measuring robustness to dephasing [44, 118]. The electrodes are connected to a set of feedthroughs from atmosphere into vacuum. The broken feedthrough was replaced with a new four channel feedthrough*. As this was cleaned before being shipped, this was not included in the components cleaned in section 3.3.4.

*LewVac FHP5-25C4-16CF

Due to the geometry of the upper 2D MOT chamber and the presence of the differential pumping tube connecting the cell to the main chamber, the constraints of dispenser shape and atomic emission direction were restrictive. This meant that using wire dispensers such as those produced by SAES* was unfeasible. As such, an equivalent to the old dispenser† was utilised‡.

A question prior to the initial vacuum break was that of the reliability of the combination Non-Evaporable Getter (NEG) and Sputter Ion Pump (SIP), pictured in figure 3.8. To avoid ambiguity in description, the combination of the SIP and NEG elements will be referred to as the ion pump§.

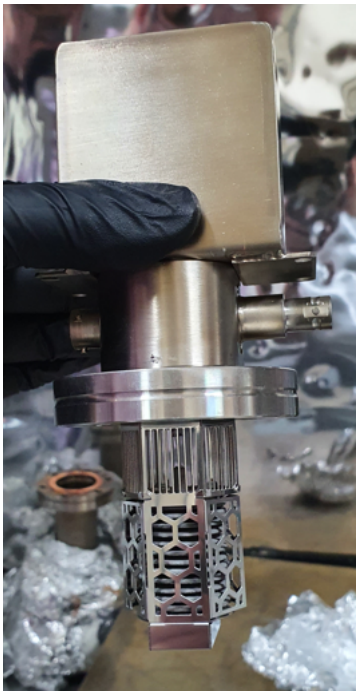

Figure 3.8: NEXTorr SIP and NEG elements.

As such, a characterisation of this component was performed on an external vacuum pumping rig to evaluate its functionality. This characterisation is detailed in section 3.3.3.

As the ion pump present on the vacuum chamber is only suitable for pressures already $< 10^{-7}$ mbar, the system was brought to this point using external equip-

*such as the Rb/NF/4.5/12/FT
†Alvatec Alvasource AS-3-Rb-250-F
‡AlfaVakuo AS-Rb-3F-275 275mg cup dispenser
§SAES Getters NEXTorr D100-5

ment. The initial roughing out evacuation to bring the system down to $10^{-4}$ mbar was achieved with a dual stage rotary pump*. In order to drop the pressure further, into the operating range of the ion pump, a turbo pump† powered by a dedicated power supply‡ was used. This pump is documented to sustain a pressure of $10^{-10}$ mbar when used in tandem with a rotary pump, however pressures only as low as $8 \times 10^{-9}$ mbar are reported (section 3.3.6) using this external pump combination.

### 3.3.3 Ion Pump Characterisation

In the months preceeding the vacuum break, the power supply§ that controlled the ion pump displayed inconsistent readings for pressure, and often showed an arcing warning despite no appreciable change to the vacuum setup. As such, it was deemed necessary to cross-check the pressure readings given by the pump to that of an external ion gauge. This was done by running a full conditioning and activation of the NEG followed by the activation of the SIP element to directly compare pressure readings.

The NEG element¶ (lower cage in figure 3.8) of the ion pump is a porous ZrVFe alloy [149] that relies on chemical adsorption of getterable atoms and compounds (such as $CO_2, O_2$ and $N_2$) to its surface to lower the pressure of its surroundings. When brought up to atmosphere, the surface of the NEG is fully saturated with adsorbable compounds, preventing any further function when placed in a vacuum system. The conditioning and activation of the NEG are undertaken to de-saturate the surface of the element, allowing for further in-vacuo adsorption to occur.

The NEG conditioning is performed to induce outgassing of physisorbed molecules from the ion pump as a whole, reducing the total number of molecules needing to be adsorbed once the system is sealed off from an external pump. This was achieved using fibreglass heater tape and is pictured in figure 3.9.

Note that this conditioning setup is from a later point in the vacuum system repair, but is functionally identical to the initial conditioning. Here the temperature of the fibreglass tape is monitored and fed back to a control box via green and white Thermo-Couple (TC) wires such as the one rising up the fibreglass and stuck to the

*Pfeiffer Vacuum Duo 3DC
†Pfeiffer Vacuum TMU 065
‡Pfeiffer Vacuum TCP 015
§NEXTorr NIOPS-03
¶SAES Getters St-172

Figure 3.9: Ion pump conditioning setup with heater tape and control thermocouples.

ion pump with high temperature orange kapton tape. The pressure of the system is monitored using an external Ion Gauge (IG)*.

The activation of the NEG element achieves the opposite to the conditioning, as instead of inducing outgassing from the pump, activation induces the diffusion of sorbed particles from the surface and into the bulk of the NEG. Thus, the surface of the element is again exposed for adsorption of colliding particles. In line with documentation from SAES Getters, the conditioning and activation processes were performed as follows:

1. Bring the ion pump to 160 °C using external heating (fibreglass tape).

*Arun Microelectronics NGC2D Ion Gauge Controller

2. Pump the system until a pressure of $\sim 10^{-7}$ mbar is measured.
3. Run ion pump NEG in the pre-set conditioning mode (4.5V, 25% power to heating element) for a full 24 hours
4. Slowly bring the temperature of the pump down below 100 °C (achieved 48 °C in 8.5 hours).
5. Run timed activation (9 V, 5 A, full 45 W power) for 1 hour.

Based on these steps, the pressure and temperature vs time graphs for this process are shown in figure 3.10.

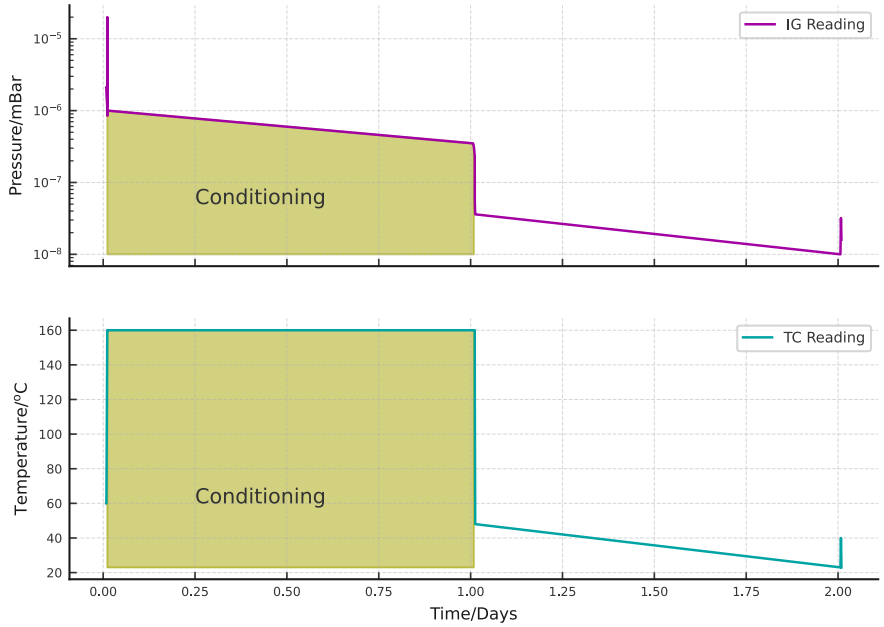


Figure 3.10: Pressure (upper) and temperature (lower) vs time during the first conditioning cycle. The conditioning cycle is highlighted in gold and the activation process is present as the small spike in pressure and temperature after 2 days.

Following this process, the gate valve to the external turbo pump was closed and the SIP was turned on. After a period of monitoring the pressure reading on the external IG and that on the NIOPS-03, the reading of the latter approached that of the former ($1.6 \times 10^{-8}$) after a few minutes. Thus the ion pump was deemed to be working sufficiently well, and the pressure reading from the power supply suitably reliable, to proceed in using these components on the experiment.

### 3.3.4 Cleaning

Certain components and tools utilised in the vacuum repair process were handled and used outside the controlled confines of the repair. As such, a thorough clean in order to remove particulates such as water and oils stuck to the surfaces of materials was required to avoid contamination of vacuum facing equipment. This was performed in an ultrasonic ($\sim$ 40 kHz) bath* by performing the following steps:

1. In a large jug or beaker, create a mixture of 95% de-ionised water and 5% Decon-90. Place the beaker in the bath filled with tap water. An example is shown in figure 3.11
2. Run the ultrasonic bath for 30 minutes.
3. Drain bath and repeat the above steps for acetone then methanol in place of Decon 90 as the chemical in the 95% water, 5% chemical mixture.

The cleaned components were: screwdrivers and allen keys for vacuum facing components, the DN40 cross-piece pictured in figure 3.12 and the welding wire used to connect the dispensers to the air-side feedthroughs (see section 3.3.5 for details on spotwelding procedure).

### 3.3.5 Assembly

Before being integrated into the experiment, the dispensers were spot welded to the welding wire cleaned in the ultrasonic bath. This process relies on the rapid heating of two conductors at a point of contact, causing them to melt and fuse together. By attaching the welding wire and a dispenser to an anode and a cathode of a high voltage source, welding occurs when the two pieces are simply brought into contact. NB: as the quality of the join made is variable between welds, the resistance of the wire-and-dispenser combination in a circuit is not consistent; therefore the operating currents required to heat atoms to evaporation are not the same between dispensers.

In order to maintain a differential pressure between the upper and lower chambers such that atoms preferentially move into the lower chamber, a narrow-aperture differential pumping tube is incorporated to separate the two chambers. This tube connects to the adjacent vacuum component via a DN16 flange, thus necessitating

*Decon FS200B


Figure 3.11: The replacement component for the gate valve between the upper and lower chambers of the experiment in the ultrasonic bath for cleaning. The motivation for its inclusion is detailed in section 3.3.5.

a smaller diameter connection between the two chambers. In the previous configuration outlined in [56], this connection was to a gate valve to allow for the independent evacuation/venting of the chambers. Due to the weight of the many components supported via this set of DN16 connections, the upper chamber sagged to one side. This in turn reduced atomic flux to the lower chamber due to gravity as the differential pumping tube was angled off-axis from vertical, as noted by H. Busche [56]. As this sagging was attributed to the strain over the DN16 connections, a wider gate valve with a DN40 connection was to be incorporated into the setup in place of the existing valve. This, however, proved impossible due to a rubber seal on the valve degrading during cleaning. Nonetheless the more stable connection was deemed of greater import than the presence of a gate valve due to the long usage lifetimes ($\sim$ 5 years each) of the dispensers; which set the timescale for how frequently vacuum breaks need occur. To preserve the overall height of the chamber and prevent 2D MOT components from blocking 3D MOT beams, the

gate valve was substituted with a cross shaped tube, with viewports on the shorter of the two lengths. This component is pictured in figures 3.11 and 3.12.

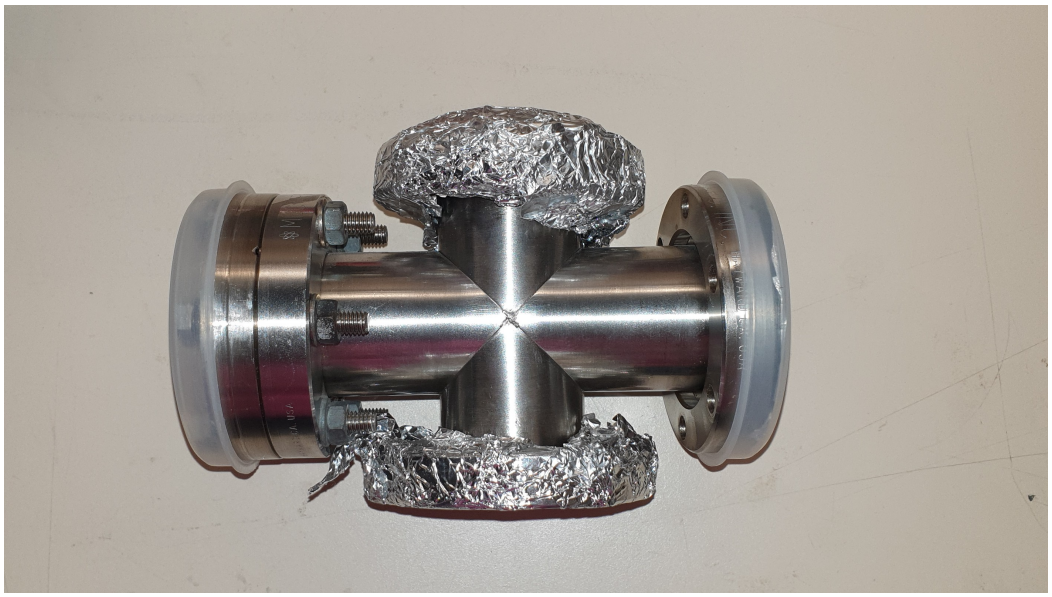

Figure 3.12: Cross piece added to vacuum chamber in place of a gate valve. The longer axis was used to connect the chambers and the shorter axis had viewports (AR coated at 780nm) added for incorporation of a weak probe for future atomic beam density and temperature measurements.

Once the necessary components had been sourced and cleaned where required, the vacuum chamber was connected to the external pumping rig. This setup is shown in figure 3.13.

In order to create a UHV suitable seal between components in the setup, rubber seals for lower quality vacuum systems are unsuitable due to gradual outgassing from the rubber. As such, an all metal alternative is utilised. Flanges on components in the system contain a protruding knife-edge on their faces, with gaskets of softer copper then sandwiched between two connecting flanges. When the connecting bolts between the two flanges are then tightened, the knife edges bite into the copper, creating a UHV suitable seal. In order to maintain an even pressure across the flanges throughout the tightening procedure, small turns are made in the pattern shown in figure 3.14 until no further turns can be performed. As the bolts connecting vacuum components will be heated to temperatures >100 °C, silvered bolts were used where possible to prevent bolts from seizing and making them impossible to remove following the bakeout process described in section 3.3.7.

Figure 3.13: Experimental Vacuum Chamber in bakeout oven, attached to the external pumping rig. The connection from the pumps is made using two sets of bellows attached via DN40 flanges (bottom left) and attaches to the chamber via gate valves on both the upper and lower chambers. The aforementioned pumps are not pictured here and are sat beneath the oven.

### 3.3.6 Pumping Down and Leak Testing

Once connected to the external rig, the chamber was evacuated via the upper and lower chamber gate valves for 12 days until a pressure of $6.1 \times 10^{-8}$ mbar was achieved. Pressure was not closely monitored during this period. The turn-on and off procedures for the specific vacuum pump setup used in our experiment can be found in appendix A.1. Following this initial pump down, all joins were tested for leaks using Helium and the Residual Gas Analyser (RGA)* attached to the external pumping rig. An example of this is shown in figure 3.15(a) and an example spike is shown in figure 3.15(b).

### 3.3.7 Baking Out

In order to desorb particles from the interior of the vacuum chamber and increase the capture rate of the external pumps, the chamber was placed in a home-built oven (the metal casing surrounging the chamber in figure 3.13). TC wires were then connected to the main body of the chamber in several places for temperature monitoring and control purposes. The control TC was attached to the base of the differential pumping tube, as the dispensers (described in section 3.3.8) were most

*SRS RGA100

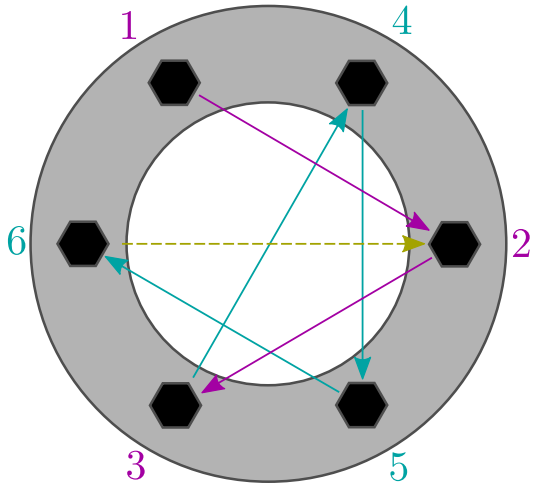


Figure 3.14: Tightening procedure for a standard DN16/ DN40 flange to ensure even pressure distribution throughout. The bolts are tightened in two sets of triangles (purple then teal), with the first bolt of the second three being the one directly opposite the last one of the first three. This pattern then continues round (gold) until no further tightening can be achieved.


(a) (b)

Figure 3.15: An example leak test using Helium. **(a)** The nozzle is pointed at joins between components to attempt to inject the gas into the chamber, which would then be detected on the RGA. **(b)** An example RGA Helium pressure spike. Though the pressure spike only reaches $\sim 10^{-10}$ Torr here, spikes up to $\sim 10^{-7}$ Torr can occur where 1 Torr $\approx$ 1.333 mbar. Note that this spike appeared after the process in section 3.3.7, and is shown here only as an example.

sensitive to temperature changes due to dispenser activation occurring at 160 °C. The chamber was then heated up over the course of several days and the pressure therein was monitored throughout. A graph of pressure and temperature vs time is shown in figure 3.16.

Due to the slow response time of the oven to adjust the temperature of the chamber, oscillations of $\sim$ 5 °C around the set value occured. As such, the oven was held at a temperature of 135 °C for the majority of the bake. The initial spike

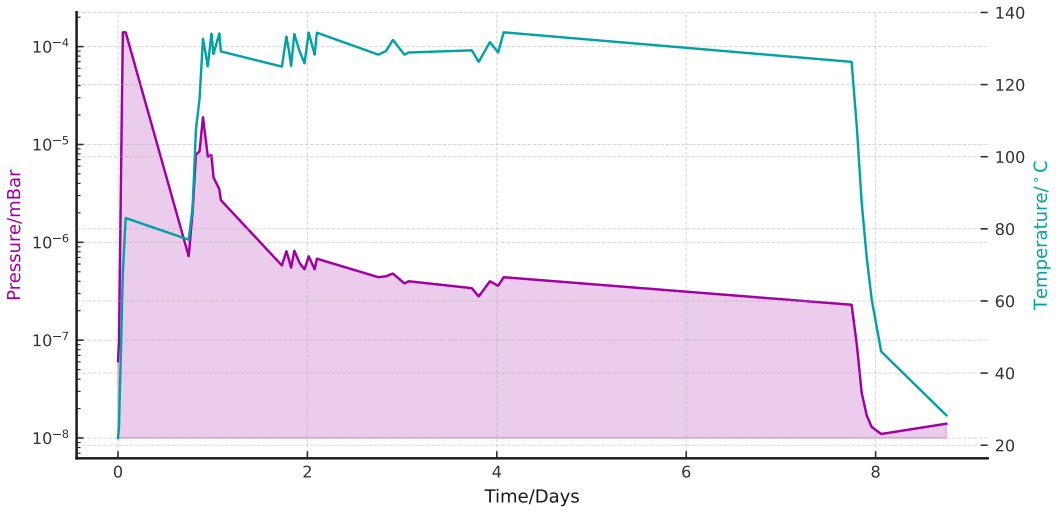


Figure 3.16: Pressure and temperature vs time graph for bake out period.Here, the temperature was held at 135 °C for the majority of the bake due to the ∼ 5 °C oscillation around the set temperature of the oven. The initial pressure spike can be attributed to the external vacuum equipment outgassing adsorbed particles after a long period without use.

in pressure at the start of the bake can be attributed to the external vacuum rig outgassing particles that had adsorbed to it's interior lining over several years due to lack of usage.

As previously stated in section 3.3.6, after the bakeout, a leak on one of the viewports was detected. The system was brought back up to atmosphere by venting the chamber to a nitrogen bladder, ensuring the chamber was brought back up to pressure with an inert gas. The viewport was then replaced the processes of assembly, leak testing, pumping down, baking out and leak testing again were repeated.

### 3.3.8 Dispenser Activation

This section is prefaced with the statement that **the described activation process initially performed was done so erroneously.** It is included here due to the pertinence of avoiding the mistakes made during the activation in the future. The errors in question were as follows:

1. Assuming a direct correspondence in activation process to that performed by Hannes Busche in the previous vacuum preparation. As the connections made by the spot welds for each dispenser are unique, the heating effect on the dispenser, and correspondingly the atomic flux from the cup, for a given current across the dispenser will vary.

2. Running the dispensers for several minutes at higher currents than the activation point.

These points will be given better context throughout the section, but are stated here due to their significance.

The AS-Rb-3F-275 cup dispensers are designed as shown in figure 3.17.

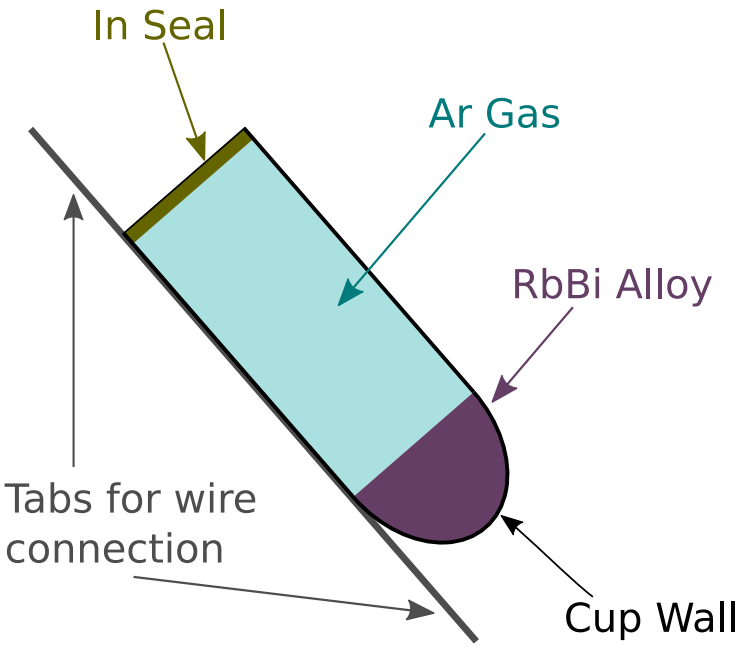


Figure 3.17: Diagrammatic cross section of a dispenser used in the vacuum setup. The Rubidium-Bismuth alloy reacts to release a Rubidium vapour. Due to the rapid oxidisation of the alloy when exposed to atmosphere, the dispensers are manufactured with an Indium seal, sealing a small quantity of inert Argon into the cup.

The cup contains a small amount of solid RbBi, which contains 275 mg of Rubidium at natural abundance. Due to rapid oxidisation of the alloy when in contact with air, the alloy is sealed in the cup, with a buffer gas of inert Argon, by an Indium seal. The dispensers are activated by heating to 450 K (177 °C)*, melting the In seal and ejecting the Ar buffer gas from the dispenser. This heating effect is achieved using resistive heating by running an electrical current across the tabs shown in figure 3.17. The activation is thus observed by monitoring the partial pressure of Ar during the process of incrementally increasing the electrical current running through a dispenser. The activation graphs for both the first and second vacuum repairs are shown in figure 3.18. NB: **The currents displayed in the initial vacuum repair were run to too-high values.**

*From AlfaVakuo dispenser manual.

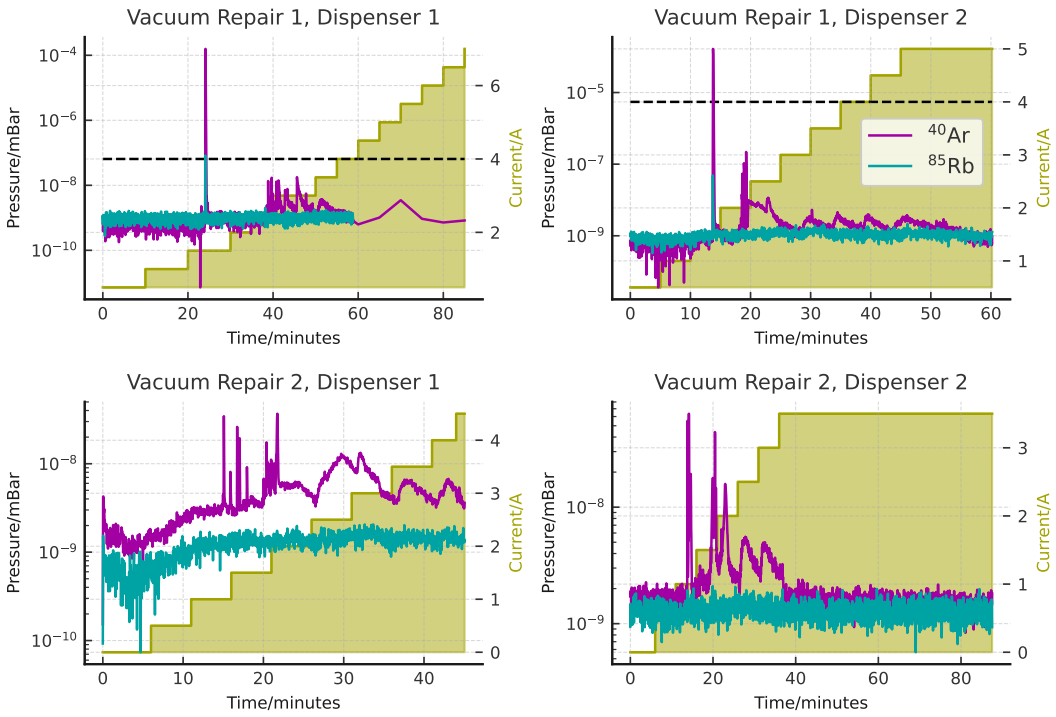


Figure 3.18: Diagrams showing partial pressures of Argon (purple) and $^{85}$Rb (blue) vs time, alongside the corresponding dispenser currents applied. The activation graphs for both the first (upper two) and second (lower two) vacuum repair processes are shown here. The dashed black lines in the upper two plots indicate a retrospective estimate on the current value (4 A) at which the activation should have concluded. Note that while the first dispenser during the second repair was activated at a current above this limit, it was sufficiently brief to avoid damage to the 2D MOT cell. Furthermore, briefly running the dispensers at 4.5 A to induce outgassing in the second repair would have prevented a subsequent pressure buildup once the chamber was returned to the lab.

Here, the currents were increased in steps over time and at a current (I) between 1 A<I<2 A, the In seals on the top of the dispensers melted to release the Ar trapped in the cups, which are shown as the spikes of the purple lines in the plots. In the initial repair, smaller spikes in $^{85}$Rb pressure were also observed, though these peaks as well as singular sharp pressure rises in Ar partial pressure for the second vacuum repair were absent. For the upper left plot, the RGA data capture mode was switched off for the last 25 minutes with only intermittent readings of the Ar partial pressure recorded over this time. For the lower two plots, due to the issues outlined in section 3.3.9 the dispensers were cautiously run up to much lower currents despite the lack of clear pressure spikes. It is likely that though the In seal had been broken, increasing the current up to 4.5 A for 5 minutes on both dispensers would have been of benefit as some additional outgassing occurred when the chamber was sealed off and returned to the lab, causing a pressure spike

($\sim 10^{-8}$ mbar) as measured by the ion pump power supply. Though the black dashed lines show a potential stopping point for activation in the upper two plots in figure 3.18, it is inadvisable to take these values as rote due to the variability of the connection quality between dispenser and welding wire. Instead, following the principle of concluding shortly after a pressure spike is observed is advised.

### 3.3.9 2D MOT Cell Malfunction

Due to running the currents (I) of the dispensers too high I>5 A for several minutes during the initial repair process, a large quantity of Rb was deposited on the interior wall of the upper 2D MOT cell. This is shown in figure 3.19.

Figure 3.19: Picture of the Rb deposits on the interior walls of the 2D MOT cell. Though the cell can still be seen through by eye, the transmission of a weak probe beam was attenuated by 60% in the worst affected areas.

Due to the large levels of attenuation of cooling light (from 40% up to 60% in the worst affected areas), multiple methods were employed to try and clear the walls of residue. These were: heating of the upper cell, Light Induced Atomic Desorption (LIAD) and high-power laser ablation. Though described here for completeness, none of these methods yielded the desired results of clearing the Rb deposits from the cell walls.

#### 3.3.9.1 Upper Cell Heating

By wrapping the upper cell in fibreglass heater tape and heating the cell up to 120 °C whilst keeping the main chamber at room temperature, the aim of this method was to simply desorb the deposits from the surface of the glass by thermal excitation, and allow the material to redeposit on the colder metal of the differential pumping tube and within the main chamber itself. This was attempted overnight, but no appreciable change to probe transmission through the cell was detected.

#### 3.3.9.2 Light Induced Atomic Desorption

Motivated by experiments where LIAD is used not only to prevent desorption from surfaces [150, 151, 152], but also control atomic density in a vapour [153, 154], an attempt at desorption using this method was performed. This was performed using unfocused 450 nm light from an unlocked CW diode* outputting a total optical power of 500 mW. As there was no change for even prolonged exposure at high intensity (achieved by placing diode close to the cell), this was also disregarded.

#### 3.3.9.3 High-Power Laser Ablation

The final measure that was attempted to limited, if not sufficient, success was ablation with a high power (<20 W) 1064 nm fibre laser†. The objective of this method is to apply an intense radiation field on a small area to desorb residue from the surface by thermal excitation. To characterise the effect of this method both in terms of required power and ablation time, the setup shown in figure 3.20 was constructed.

In this setup, the fibre laser and probe beam were aligned through a narrow aperture using the fibre laser's low power red guiding beam such that both beams overlapped on a spot on the near side of the cell to the lasers. The 1064 nm beam was then dumped and the probe beam was terminated by a power meter head. The power meter was then set to continuously record the transmission of the probe and the high power beam was switched on. An example of change of probe transmission vs time for the three powers investigated (2 W, 4 W and 6 W) is shown in figure 3.21.

As is the case for these curves, all probe transmission changes were of the form of exponential decay towards a steady state value. Though this shape was consistent

*Opt Lasers PLTB 450b
†IPG Photonics YLM-20-LP-SC

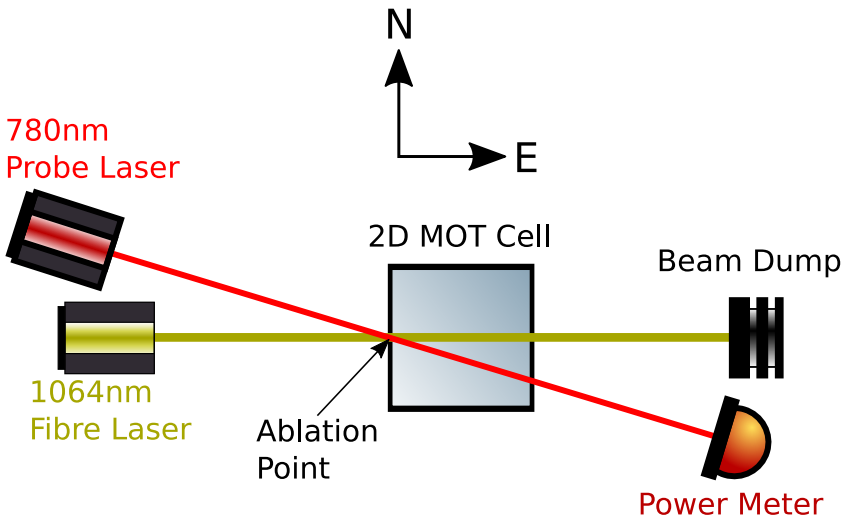


Figure 3.20: Beam diagram for laser ablation. Here, the fibre laser and probe were aligned using the fibre laser's low-power red guiding beam such that both beams passed through the same spot on the near side of the 2D MOT cell. The high power beam was then dumped and the transmission of the probe over time was recorded on a Throlabs PM100D power meter. When the ablation beam was turned on, the transmission through the cell over time was recorded.

across all runs, the efficacy of the method varied relatively substantially. Readings akin to those shown in figure 3.21 were repeated 5 times for each investigated power and the average percentage change to probe power between before and after the ablation process, as well as initial rates of change of transmission, are shown in figure 3.22.

Across the data sets taken, a large variation in the effect of ablation power on transmission was observed. Thus, though there was a notable improvement on probe transmission in the increase from 2 W to 4 W of ablation beam power, there was no clear improvement thereafter. Additional powers were not investigated as, in areas with large deposits, when a higher power beam ($\geq$6 W) was incident on the cell a gold residue formed at the ablation point. This effect was also observed by Sekiguchi *et. al.* [155] and is irreversible. To ensure this issue was not due to only a single spot being ablated for too long, the beam was scanned across the cell using an electronically controlled translation stage* to ablate a small area of the cell. Transmission of a probe through the cell still remained <50% at points, resulting in both a low radiation pressure on atoms in absolute terms, and a significant imbalance in pressures from outgoing and retro-reflected beams. Concluding this, the ablation did not yield the significant improvements on transmission through the cell that would be necessary to deem this procedure a success, therefore this method was also disregarded. After exhausting the available methods by which to

*ThorLabs MTS25-Z8

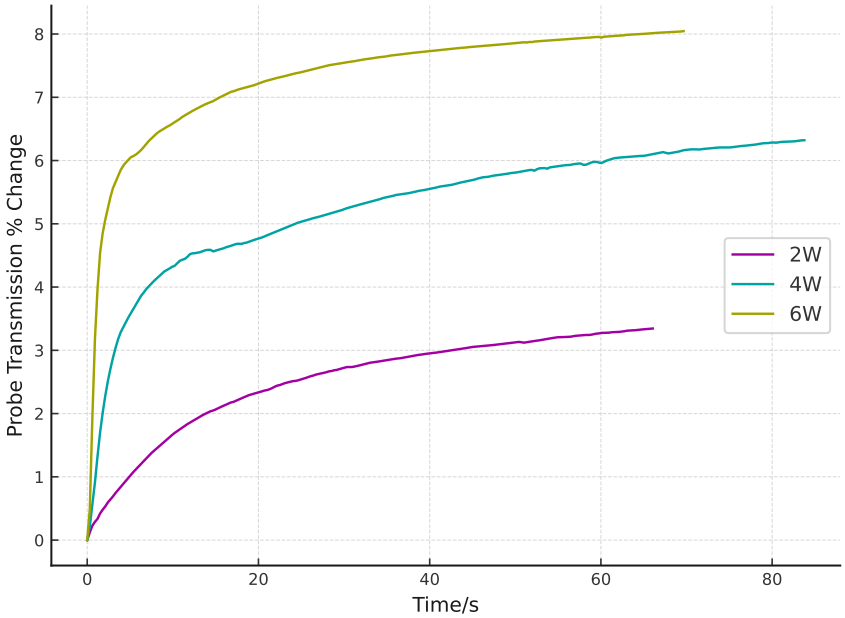


Figure 3.21: Example probe transmission change through the 2D MOT cell during the ablation process. Time t=0 is set to when the high-power beam is switched on. A case where all three curves are distinguishable is shown here, however this was not generally the case, and a substantial variation in efficacy for different beam powers was observed. This effect is illustrated in figure 3.22.

clear the cell walls, a replacement cell was identified, new dispensers were obtained and a second vacuum break was performed to replace these components.

### 3.3.10 Second Vacuum Break and Upper Cell Replacement

The replacement 2D MOT cell was a modified cell* with a total cooling volume of 30x30x100 mm. The cell had two notable distinctions from the original. Firstly, though the width of the cell was identical, it is shorter by one cooling volume; the old cell posessed 4 cooling volumes whilst the new one is long enough for only 3. Secondly, due to time constraints it was impossible to get the cell AR coated in time for the repair process. To account for this, a set of lenses were used to focus the beams down and maintain beam intensity between the outgoing and retro-reflected cooling beams. The adjusted optical setup incorporating these focusing optics is shown in figure 3.23. The CAD drawings and optimal focal length calculations are given in Oliver D. W. Hughes' thesis, but the characterisation of their effect is shown in this text in section 3.4.1. As the techniques used in this characterisation have not yet been established, it precludes its inclusion here.

*Precision Glassblowing 2DMOT CELL 2.75

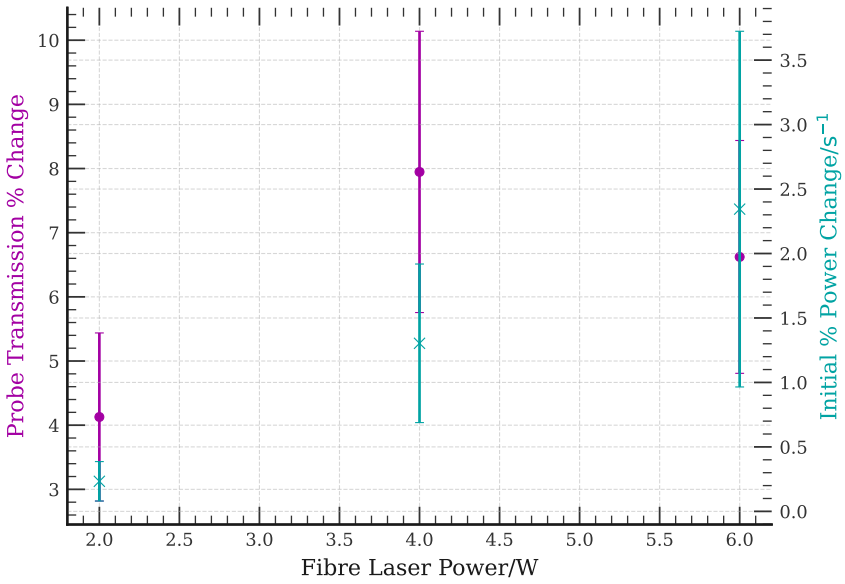


Figure 3.22: Ablation beam power vs probe transmission percentage change (purple) and initial rate of change (blue). Though there is a distinct positive effect in the initial increase of fibre laser power from 2 W to 4 W, the increase from 4 W to 6 W yields no distinguishable improvement.

The second vacuum repair process proceeded in similar fashion to the initial repair as listed in section 3.3.1. In this second evacuation, no leaks were found during the leak testing stage, meaning no additional breaks and re-evacuations were required in this second round. As such, this repair process could be viewed as an 'ideal' case and instead of showing each step individually, the entire repair process from atmospheric pressure to $10^{-10}$ mbar is shown in figure 3.24.

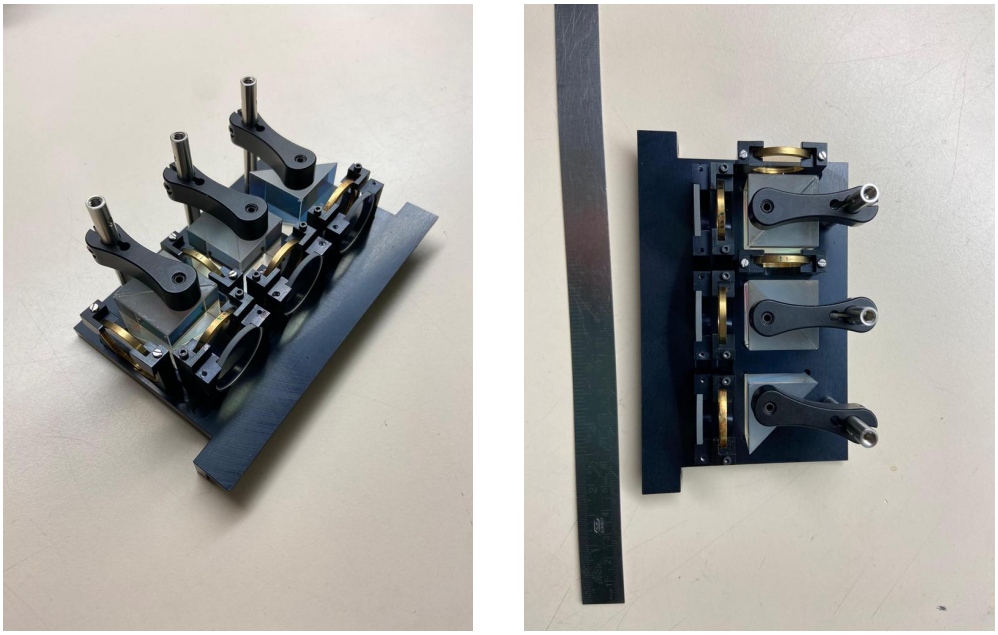

(a) (b)

Figure 3.23: New 2D MOT optics mounts incorporating long focal length ($f$=1m) lenses. Photos courtesy of O. D. W. Hughes.

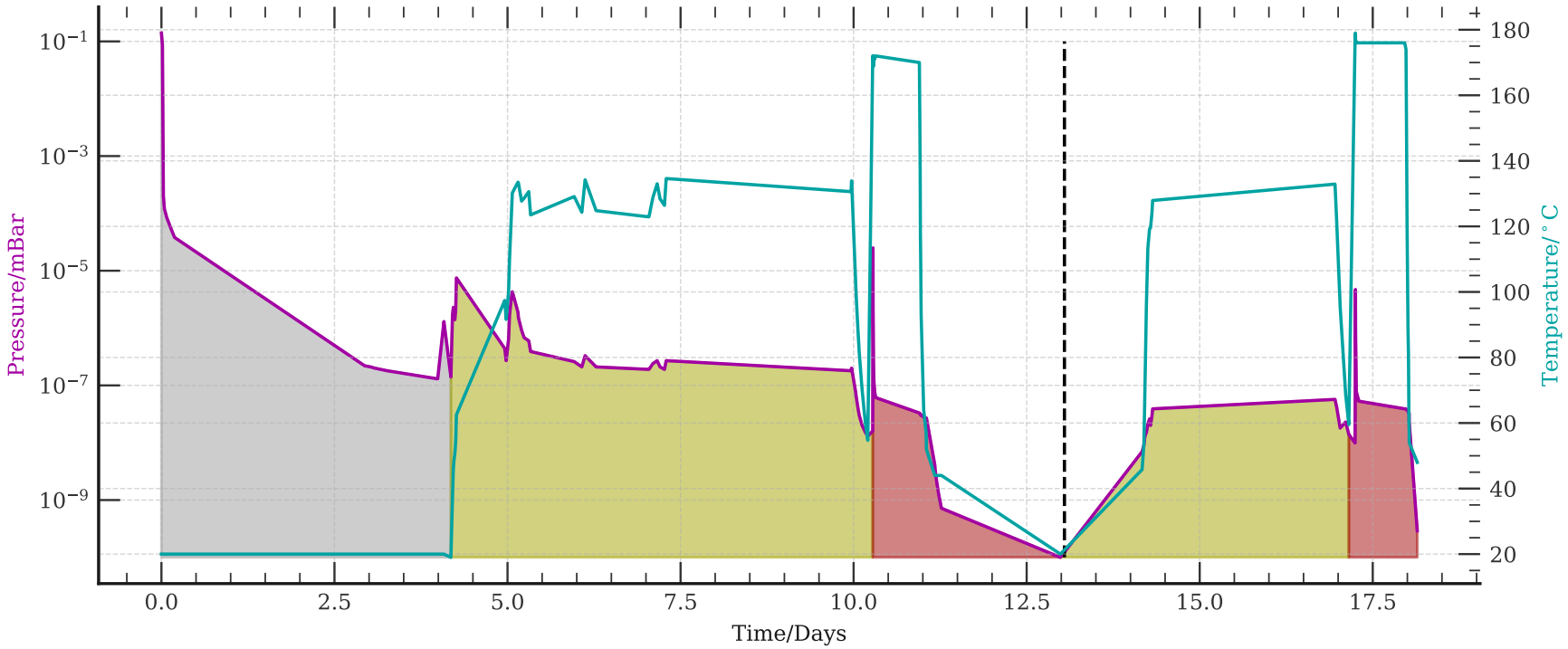


Figure 3.24: Pressure and Temperature vs Time for an Uninterrupted Vacuum Repair. The purple line shows the pressure in the system and the cyan line shows the temperature at each stage. The coloured shading under the pressure curve shows the process being performed at a that time. The grey shading indicates the initial pump down using the rotary and turbo pump combination, the gold shading corresponds to the bakeout procedure described in section 3.3.7 and the red shading to the NEG conditioning, activation and SIP pumping. The dashed black line indicates the time at which the dispensers were activated as in section 3.3.8. For the red shaded areas, the temperature shown by the cyan line corresponds to the temperature of the ion pump itself, as this area was locally heated with fibreglass heater tape whilst leaving the rest of the chamber at room temperature. Furthermore, the pressure readings during the SIP operation (the lower temperature portion of the red shaded areas) were taken from the NIOPS-03 ion pump control box, rather than from the external IG.

The above figure shows the variation of pressure and temperature throughout the vacuum repair process. The purple line shows the pressure during this process and the cyan line shows the corresponding temperature throughout. The shaded areas under the purple pressure curve show the process being performed at that time. The initial grey shading corresponds to the first pump down using the rotary and turbo pump combination as stated in section 3.3.2; the turn-on procedure for the setup is shown in appendix A.1. Next, the two gold shaded areas indicate the two bakeouts required during the process as described in section 3.3.7. The red shaded area corresponds to the process of NEG conditioning and activation and SIP pumping, which is outlined in section 3.3.3. The dashed black line shows the time at which the dispensers were activated (section 3.3.8) where the pressure remained low throughout, notwithstanding the spike due to the emission of Ar from the cups. During the two ion pump preparation stages of the vacuum repair, the temperature readings correspond to the temperature of the ion pump, rather than the entire chamber, as the area was locally heated as is shown in figure 3.9. The pressure readings during the low temperature portions of the red shaded areas are derived from the current reading on the NIOPS-03 ion pump control box, rather than the external IG.

The sharp pressure spikes at $t \approx 10.25$ and $t \approx 17.25$ days correspond to the initial stages of the NEG conditioning, where a significant amount of outgassing from the element occurs thus causing the spike in pressure. The small changes in temperature during the first bakeout are present due to the slow acclimation time of the vacuum chamber during the process, causing the oven to over-work in bringing the chamber to temperature, thus inducing a temperature over-adjustment and creating small oscillations of $\sim 10$ °C around the set value, as described in section 3.3.7.

The last significant deviation from the first vacuum break came in the form of another reside deposition on the interior walls of the upper cell. Unlike the first vacuum repair, the residue lining the cell was of a blue, rather than grey colour and is pictured in figure 3.25. This is indicative that the residue was not Rb as in the first vacuum break, but instead In that was blown out from the dispenser cups during the activation process. As such, by heating the upper cell to 140 °C overnight after this was observed, the deposit was cleared from the cell walls and the repair process was concluded. Following this repair, the chamber was sealed off from the external pumps and returned to the laboratory. Once back in-situ, work commenced to set up the chamber for ultra-cold atom experimentation. This section of the repair is described in section 3.4.

Figure 3.25: Blue residue deposited on the interior lining of the 2D MOT cell for the second dispenser activation.

## 3.4 Ultra-Cold Atomic Trapping

With a suitably well evacuated optically-accessible science chamber, atoms can be trapped and cooled to remarkably low temperatures using nothing but optical and magnetic fields using the landmark MOT [18]. Once cooled sufficiently, this cold cloud is compressed and cooled further with sub-Doppler cooling before a smaller, both spatially and in depth, FORT is used to prepare this smaller cloud for Rydberg atom formation and further experimentation.

This section details the techniques and processes utilised in the optimisation of

the first two of these stages: MOT and sub-Doppler cooling.

Once the (not so) simple task of initially forming and observing a MOT had been achieved, attention was turned to optimising the trap both for temperature and loading rate. Before considering these two metrics for optimisation, we first must consider the methods by which these can be measured; namely, these are MOT fluorescence and absorption imaging. The former method was used solely to optimise loading rates and the latter was used to optimise MOT position and temperature using Time Of Flight (TOF) measurements. These methods are described in sections 3.4.1 and 3.4.2 below.

### 3.4.1 Loading Rates

As a MOT loads over time, it tends towards a large steady-state population in a decaying exponential fashion. Due to the high repetition rate of our experiment, the focus in optimisation is not to maximise the steady state population, but instead the sharp initial loading rate. The setup used to achieve this was simply constructed, with a variable gain Photo-Diode (PD)* placed along the dipole trap axis with a short focal length ($f = 4$cm) lens affixed in order to maximise the signal into the PD. The dipole trap axis was selected to take advantage of the *in-vacuo* high NA lenses, thus increasing the effective solid angle detected by the PD. In order to convert a PD voltage $V_{PD}$ into a usable atom number $\mathcal{N}$, a number of factors must be considered. Firstly, a relationship between optical power and PD voltage must be established. This is given as†

$$V_{PD} = R(\lambda)GSP_{\mathrm{Det}}, \tag{3.3}$$

for PD responsivity at a given wavelength $R(\lambda)$, gain $G$, scale factor of resistances $\mathrm{S} = \mathrm{R_{Load}}/(\mathrm{R_{Load}} + \mathrm{R_S}) = 10^6/(10^6 + 50) \approx 1$ and detected optical power $P_{Det}$. Secondly, a relation for optical power detected to atom number is required [54]. By considering the decay rate of the $\mathrm{D_2}$ transition $\Gamma_{\mathrm{D_2}}$, photonic energy $E_{\mathrm{D_2}} = \hbar\omega_{\mathrm{D_2}}$ and atom number $\mathcal{N}$ and noting that even for a saturated transition only 50% excited population is possible, this is given by

$$P_{\mathrm{Tot}} = \frac{1}{2}\Gamma_{\mathrm{D_2}} E_{\mathrm{D_2}} \mathcal{N}. \tag{3.4}$$

By equating the detected power to total power multiplied by the fractional solid angle that the PD can detect over as well as a loss factor ($\zeta$) due to the lack of AR

*ThorLabs PDA36A-EC
†From the ThorLabs PDA36A-EC manual

coating on the *in-vacuo lenses*, the two equations can be related. In mathematical form, this is given as

$$P_{\text{Det}} = \zeta \frac{\Theta}{4\pi} P_{\text{Tot}}. \tag{3.5}$$

by substituting the form of $P_{\text{Det}}$ in (3.3) into (3.4) and rearranging for atom number $\mathcal{N}$, atom number can be expressed in terms of voltage as

$$\mathcal{N}(V_{PD}) = \frac{8\pi}{R(\lambda)GS\Theta\zeta\Gamma_{\text{D}_2}E_{\text{D}_2}} V_{PD} = \beta_{PD} V_{PD}. \tag{3.6}$$

The value of each parameter for the PD used in our experiment at 780 nm is given in table 3.1.

| Parameter | Symbol | Value |
|---|---|---|
| Responsivity at 780nm | $R(\lambda = 780\text{nm})$ | $0.478 \pm 0.001$ A/W |
| Gain at 60dB | G(60dB) | $1.500 \pm 0.075$ MV/W |
| Scale Factor | S | 1 |
| Solid Angle Detected | $\Theta$ | 2.083 sr |
| Loss Factor | $\zeta$ | $0.86 \pm 0.01$ |
| Transition Rate | $\Gamma_{\text{D}_2}$ | $2\pi \cdot 6.0666 \pm 0.0018$ MHz |
| Transition Energy | $E_{\text{D}_2} = \hbar\omega_{\text{D}_2}$ | $2.5492 \times 10^{-19}$ J |
| Total Conversion Factor | $\beta_{PD}$ | $13 \pm 1 \times 10^{6}$ V$^{-1}$ |

Table 3.1: Parameters used in equation 3.6 to convert a PD voltage to atom number. The loss factor $\zeta$ is taken from S. Ball's thesis and the optical loss through the non AR coated high NA lenses [57]. The solid angle $\Theta$ is taken as the solid angle through a single high NA lens. An error on transition energy is omitted for readability due to being negligible to calculation.

The loss factor $\zeta$ is taken from S. Ball's thesis and the optical loss of a single pass through a non AR coated high NA lens [57]. As all other surfaces are suitably AR coated, losses through other surfaces were considered negligible in comparison. The solid angle $\Theta$ is taken as the solid angle through a single high NA lens as it is assumed that any light emitted in this range will be suitably well collimated by the high NA lens and thus reach the detector. An error on transition energy is omitted for readability due to being negligible to calculation.

Using the setup described above and converting to atom number using (3.6), an example loading curve is given in figure 3.26.

By continuously loading and re-loading the MOT on $\sim 100$ ms timescales, loading curves such as those in figure 3.26 can prove a useful diagnostic tool for real-time optimisation of parameters such as beam powers, alignments and polarisations.

Using this technique, the effect of the 2D MOT's long focal length lenses on the subsequent 3D MOT loading was investigated. To do this, the following setup

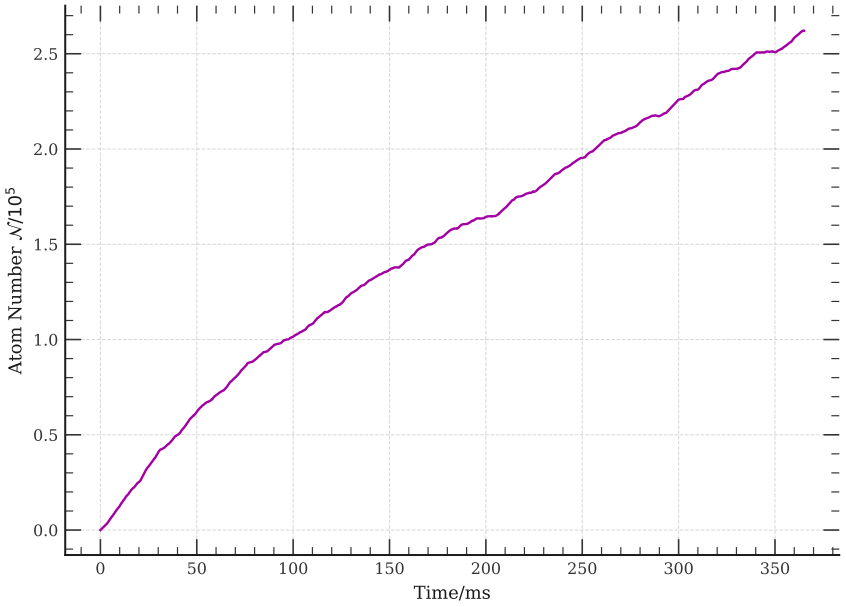


Figure 3.26: Example atomic loading rate over time in a 3D MOT.

procedure was conducted, using loading rate of the 3D MOT as the figure-of-merit being optimised at each step:

1. Overall power going into each axis was tuned.
2. Beam alignment between fibre output and cooling volumes was optimised for each axis.
3. The power distribution between the cooling volumes was adjusted.

The above optimisation procedure was performed initially with focusing lenses (with 35 mW in each axis) before averaged loading curves over 32 repeats were taken for a range of currents supplied to one of the cup dispensers. The optics were then removed and the beam alignments and power distribution (steps 2 and 3 in the above list) were re-optimised for the unfocused configuration, but no further adjustments for overall power were made, which remained at 35 mW throughout. The process of recording loading rates for a range of dispenser currents was repeated. Curves akin to that shown in figure 3.26 were recorded and fitted to a decaying exponential of the form

$$\mathcal{N}(t) = \mathcal{N}_\infty(1 - e^{-\alpha_\mathcal{N} t}), \tag{3.7}$$

for a steady state atomic population $\mathcal{N}_\infty$ and time constant $\alpha_\mathcal{N}$. As the initial loading rate is of import, a first order Taylor expansion can be performed to give an initial loading rate of

$$\frac{d\mathcal{N}}{dt} = \alpha_\mathcal{N}\mathcal{N}_\infty. \tag{3.8}$$

The loading rates for a range of dispenser currents both and with and without focusing optics are shown in figure 3.27. The loading rates for the cases where

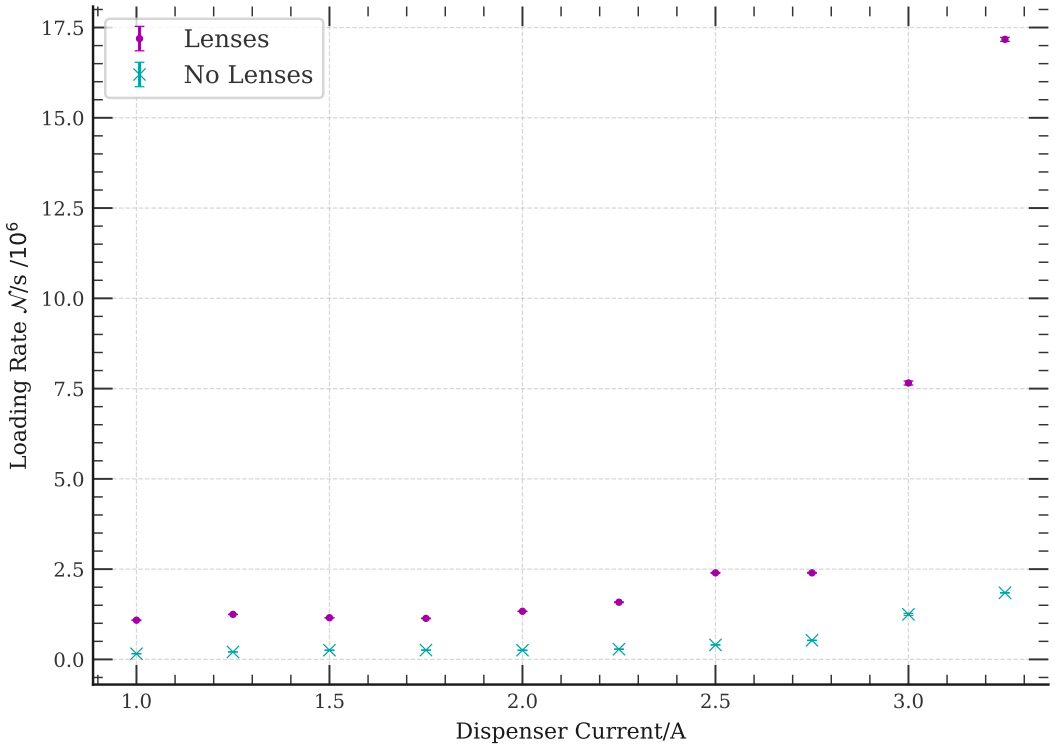


Figure 3.27: 3D MOT loading rates vs dispenser current both with (purple) and without (cyan) focusing optics. Errorbars shown here are derived from the numerical errors on the fitting parameters in (3.7).

focusing optics are (purple) and aren't (cyan) utilised on the 2D MOT are shown here. There is a clear improvement in loading rate both at low currents where loading from the 2D MOT is likely dominated by interactions with the background pressure of $^{87}$Rb and at higher currents when a distinct increase in loading rate occurs. The errors on the data are calculated from the numerical fitting of the loading curves to (3.7) and propagated forward from there.

Whilst this data is evidence that the 2D MOT is more efficient at the 35 mW of optical power per axis, this does not preclude the possibility that the loading rates when using focusing optics can be matched by a re-optimisation of overall power and power distribution in the 2D MOT for higher powers. Despite this possibility, the inclusion of the focusing optics allows for a lower, and consequently safer, optimal operating power and thus remain on the upper chamber for future experimentation.

### 3.4.2 Position and Temperature Optimisation

Wheras the previous technique relied on emission of light from atoms, absorption imaging relies on the attenuation of resonant light to derive properties of an atomic cloud. When resonant light passes through an optical medium, the intensity of the light at a given coordinate in the beam cross section $I(x, y)$ is attenuated according to the Beer Lambert Law [156, 2]

$$I(x, y) = I_0(x, y)e^{-n(x,y)\sigma_{\text{Cross}}}, \tag{3.9}$$

for an input intensity $I_0(x, y)$, column density $n(x, y)$ and absorption cross-section $\sigma_{\text{Cross}}$. For a weak, resonant probe of the closed $D_2$ transition, this cross-section becomes $\sigma_{\text{Cross}} = \sigma_0 = \frac{3\lambda^2}{2\pi}$ [2]. Rearranging for column density $n(x, y)$ using $\sigma_{\text{Cross}} = \sigma_0$ gives

$$n(x, y) = -\frac{1}{\sigma_0} \ln\left(\frac{I(x, y)}{I_0(x, y)}\right). \tag{3.10}$$

By taking two images, one with and one without a MOT present, 2D intensity mappings of $I(x, y)$ and $I_0(x, y)$ may be obtained. Then by comparing the two mappings using (3.10), a 2D column number density perpendicular to the direction of the imaging beam can be obtained. Experimentally, this is achieved using the setup shown in figure 3.28.

In this setup, a $4f$ imaging system utilising $f = 1$ m and $f = 40$ cm lenses is used to magnify the beam to 2.5 times its original size [157]. This is done such that the small MOT ($\sim$ 0.5 mm diameter) can be imaged clearly on the $6.58 \times 4.96$ mm CCD of the camera* with a pixel size of 10 $\mu$m. In order to reduce the effect of background light, an interference filter was used to eliminate optical noise on the CCD. Whilst the component served this purpose, intensity fringes were generated due to this and the lenses used, regardless of cleaning repetitions. An example of this issue is shown in figure 3.29, which is a simple background subtraction of an image with a MOT present from its corresponding control image without one.

Due to the irregularity of the patterning, and the size of the noise in comparison to the MOT features, this noise needed to be accounted for. As the vast majority of the intensity noise occurs on length scales much shorter than the MOT, the raw image files were processed with a Fast Fourier Transform (FFT), and high frequency components were filtered out from the images. Then, the data for each pixel of the camera for the MOT and control images were passed as arguments in (3.10) to calculate a number density. The number density of the cloud in the above plot is shown in figure 3.30. Whilst atom numbers can in principle be extracted from absorption images such as the one shown above, only the previously mentioned

*Andor Luca

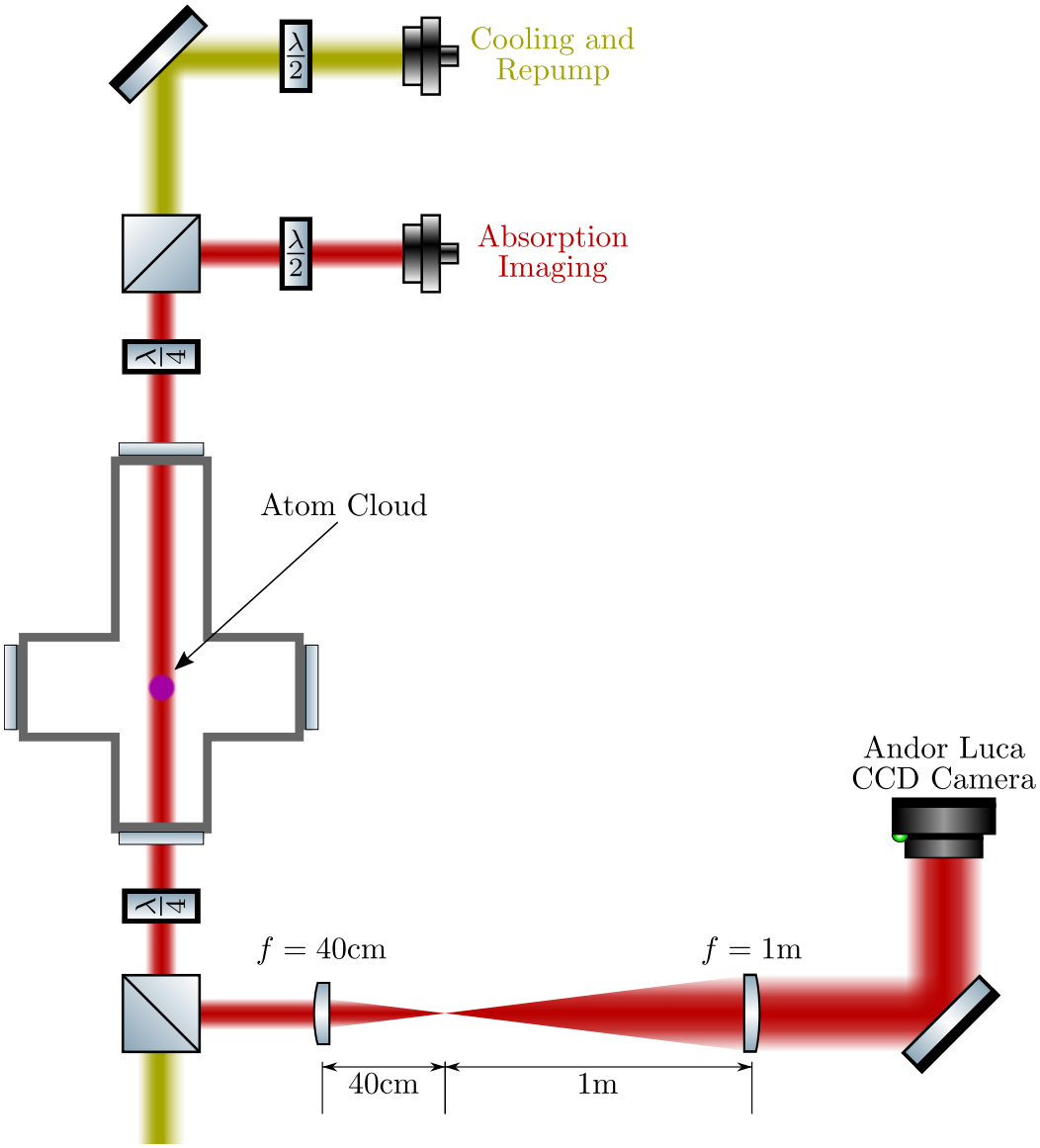


Figure 3.28: Beam diagram for the absorption imaging setup used to characterise MOT position and temperature.

fluorescence measurements were used to optimise this due to the ability to monitor this in real time, rather than in a stop-start fashion with the absorption imaging. The tool of absorption imaging offers a view at certain properties of the atomic cloud. First is atom number which has been discounted for the reasons stated, but the second and third: cloud position and size, served as invaluable diagnostic tools.

Cloud position was used to optimise the ideal currents of the shim coils in the plane perpendicular to the imaging plane such that the magnetic field zero position was well overlapped with the crossing point of the MOT beams. As described

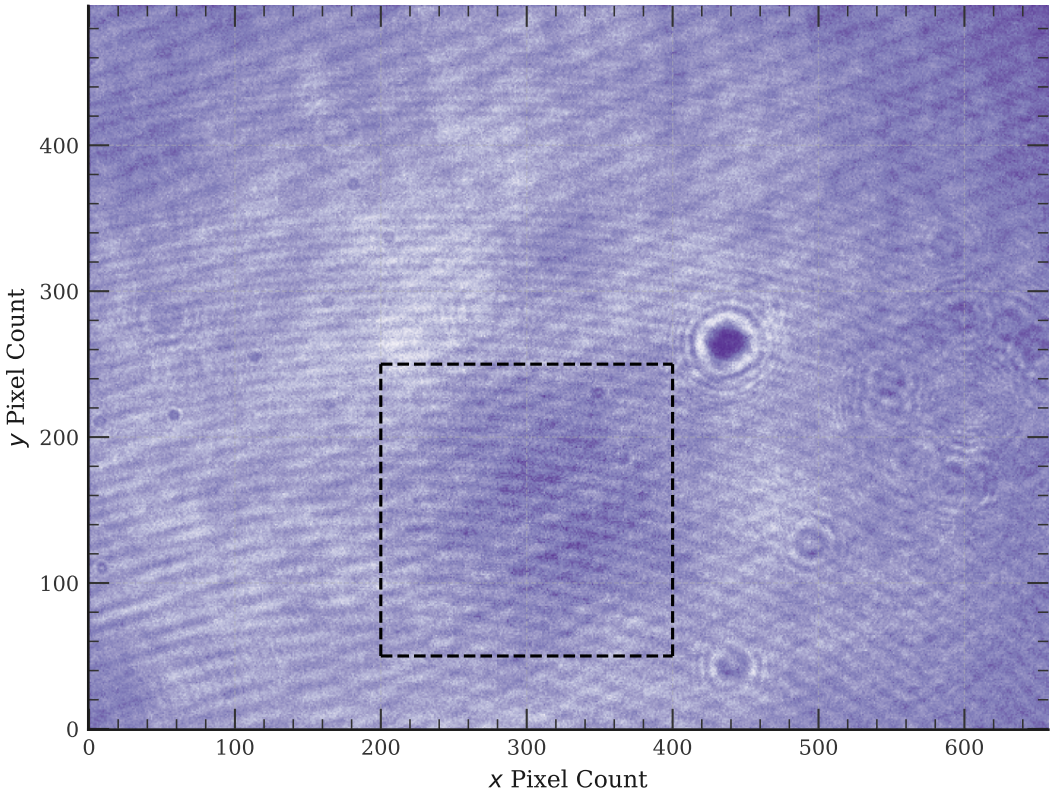


Figure 3.29: Example intensity noise in a background subtraction of an image with a MOT present from one with no MOT present. Later analysis reveals that the ROI outlined in black dashed lines is the MOT image.

in D. Boddy's thesis [158], this was performed by measuring the position of the centre of the cloud for a range of shim coil currents with a constant overall MOT anti-Helmholtz magnetic field and plotting shim coil current vs cloud centre position. By repeating this process for a variety of overall MOT magnetic fields and identifying the shim coil current at which the curves for different overall MOT fields overlap, the optimal shim coil current for a given axis can be identified. The plots for this above process for both the horizontal (East-West) and vertical directions perpendicular to the imaging plane are shown in figures 3.31 and 3.32 respectively.

Prior to using these optimal shim coil currents, whenever the MOT coil current was ramped down, the atom cloud would move and be kicked out of position. With these optimal shim coil currents, movement of the cloud as the field gradient ramped down to 0 was suppressed and the cloud was allowed to expand naturally, with the only motion being that of falling under gravity. With the cloud in this state, measurements of atomic temperature were possible.

When unconstrained by any optical or magnetic trapping, an atomic cloud with a

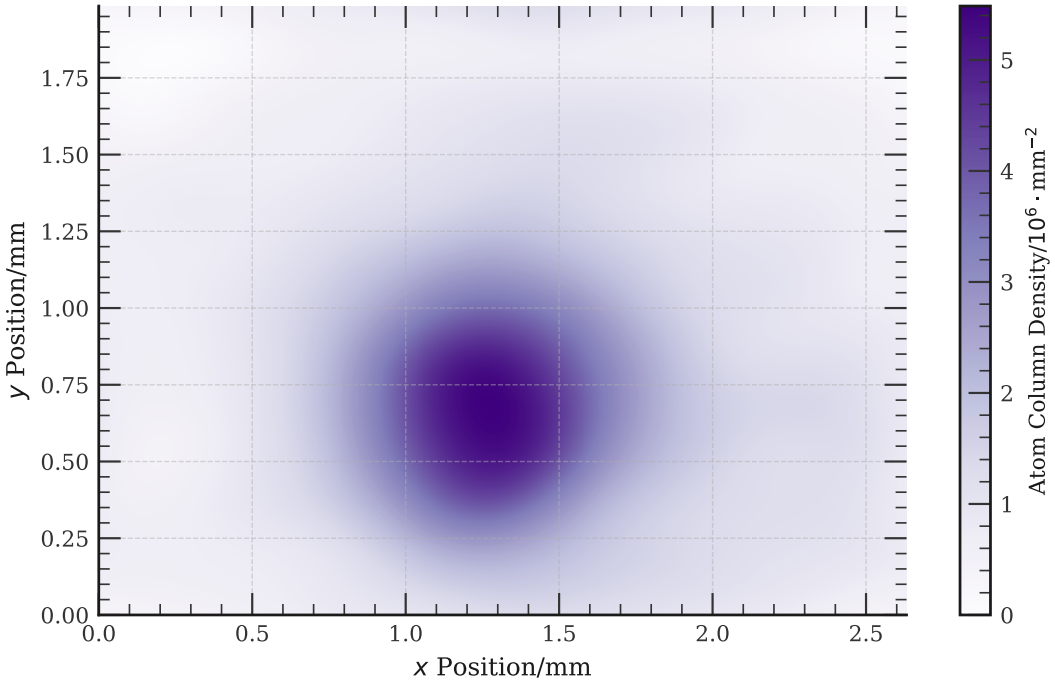


Figure 3.30: Example post-processing absorption image. Co-ordinate axes and number densities have been scaled to account for the magnification of the imaging system.

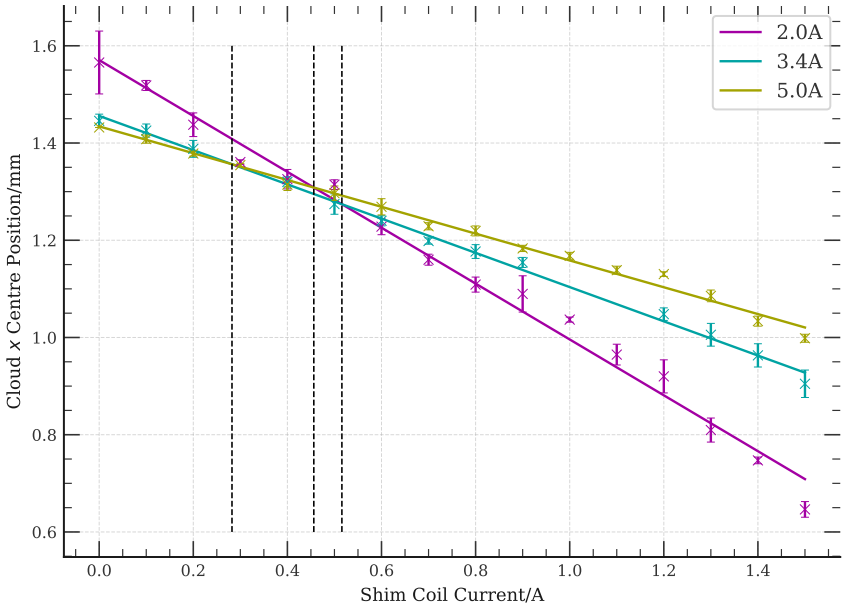


Figure 3.31: Shim Coil Current Optimisation in the East-West direction for anti-Helmholtz MOT coil currents: 2.0 A (purple), 3.4 A (cyan) and 5.0 A (gold). The dashed black lines show the crossing points of the fitting lines used to calculate the optimal value, taken as an average over all three points. In the east west direction, this is $I_{\mathrm{Opt-EW}} = 0.42 \pm 0.1$ A.

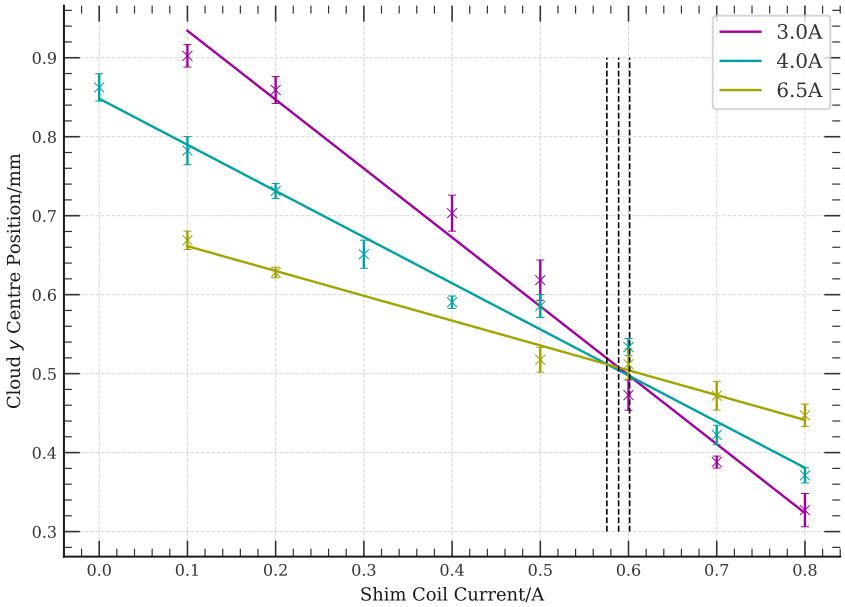


Figure 3.32: Shim Coil Current Optimisation in the Up-Down direction for anti-Helmholtz MOT coil currents: 3.0 A (purple), 4.0 A (cyan) and 6.5 A (gold). The dashed black lines show the crossing points of the fitting lines used to calculate the optimal value, taken as an average over all three points. In the up-down direction, this is $I_{\mathrm{Opt-UD}} = 0.59 \pm 0.01$ A.

density distribution along a given axis of the form of a 1D-Gaussian has a standard deviation in its distribution of $\sigma_t$ at time t. In this context, the standard deviation of the 1D density distribution is defined as the 'Gaussian radius' of the cloud, and defines its size. Considering the initial radius of the cloud at time $t = 0$ of $\sigma_t(t = 0) = \sigma_0$ with a velocity distribution of radius $\sigma_v$ [159], the radius of an atomic cloud at time $t$ is given by

$$\sigma_t = \sqrt{\sigma_0^2 + \sigma_v^2 t^2}. \tag{3.11}$$

As the temperature of the cloud relates to the velocity distribution by

$$T = \frac{M}{k_{\mathrm{B}}} \sigma_v^2, \tag{3.12}$$

for atomic mass $M$ [159], the temperature of an atomic cloud can be derived by its rate of ballistic expansion when unconfined. By taking absorption images of the atom cloud with varying wait times and calculating the clouds' corresponding values for $\sigma_t$, one can obtain a measure of the temperature of the atoms from (3.11) and (3.12). With optimised parameters for the cooling sequence (discussed in section 3.4.3), a set of absorption images with wait times varying from 2 ms $\leq t \leq$ 24 ms were taken and are plotted in figure 3.33.

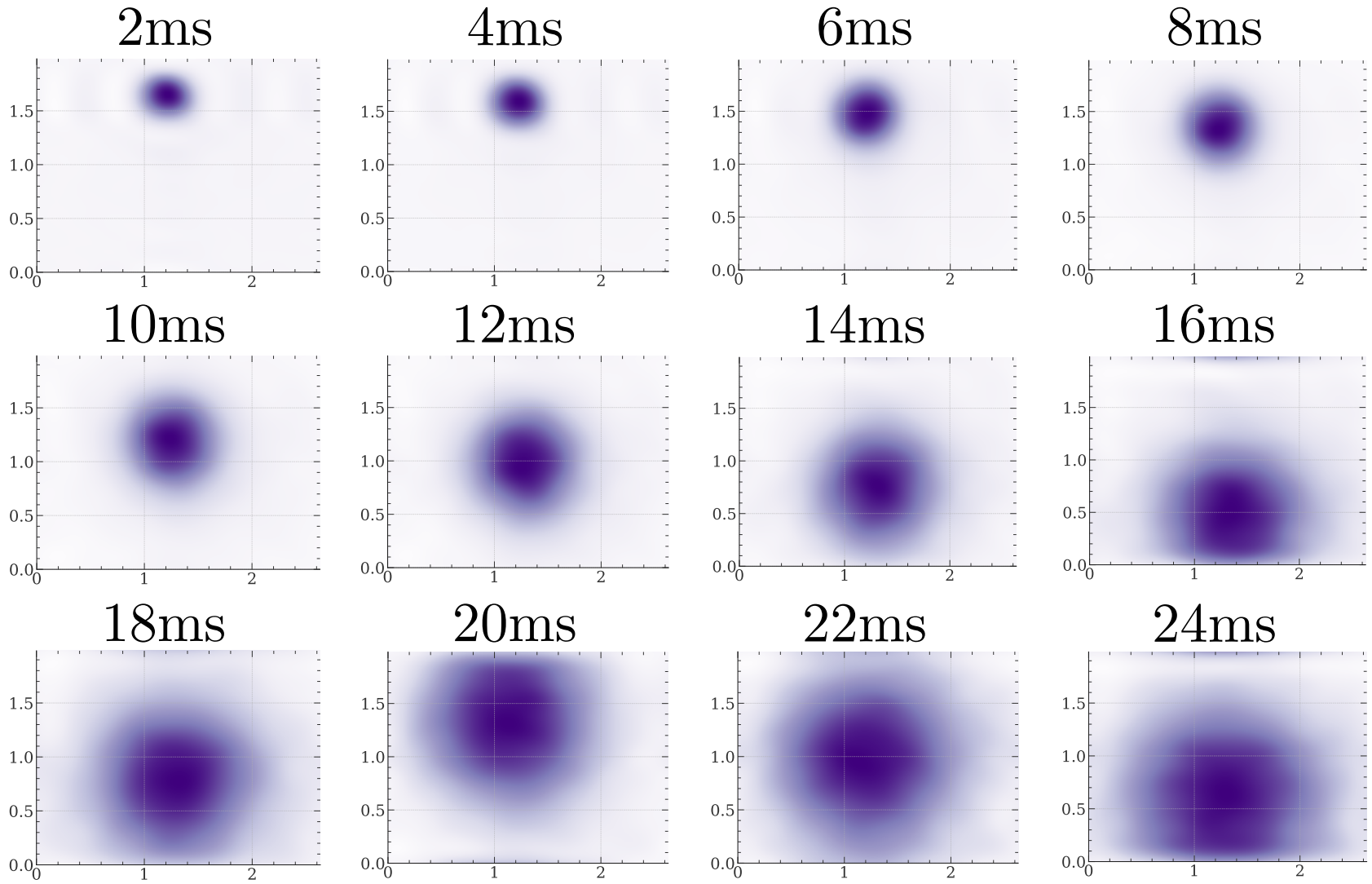


Figure 3.33: TOF absorption images of atomic clouds with expansion times 2 ms $\leq t \leq$ 24 ms. For the first 16ms, the absorption imaging beam was kept in the same position, thus the decrease in the cloud's y coordinate centre is indicative of it falling under gravity in this time. As the cloud moves out of range of the imaging beam after this time, the position of the imaging beam readjusted twice more (at $t = 18$ ms and $t = 20$ ms) to ensure the imaging light remains incident on the atomic cloud. Each image displayed here is an average over 100 repetitions, each repetition taking a background and image for a total of 200 images.

For the first 8 of these images up to a wait time of 16ms the imaging beam was not adjusted, therefore the cloud dropping further and further down the imaging window is indicative of the cloud falling under gravity. After 16 ms, the cloud reached a point where it was being imaged on the edge of the first imaging lens and thus the image was warped. At this point the beam was adjusted to re-centre the cloud on the camera's CCD and another image was taken. At $t = 20$ ms the beam was re-positioned for a final time and the final 3 images were taken. Each image shown here is an average over 100 repetitions, each one taking a MOT image and a background shortly after such that power drifts on the timescales of seconds would not affect the measurements.

To calculate the cloud size at each wait time, the 100 image pairs were split into 10 groups of 10 and equivalent images to those shown in figures 3.30 and 3.33 were generated. Then, the densities along the $x$ ($y$) axis were fitted to a 1D Gaussian at the cloud's centre $y$ ($x$) value and a value of $\sigma_t$ was extracted. This was repeated for all 5 groups and an average cloud size and associated error were calculated. This was repeated for all wait times shown in figure 3.33 and the results of this, along with a fitting to the expression in (3.11) and a residual plot, are shown in figure 3.34. From these plots, temperatures along the horizontal and vertical axes are given by $T_x = 33.0 \pm 1.1$ $\mu$K and $T_x = 33.2 \pm 1.2$ $\mu$K respectively. These temperatures are in line with those achieved in the previous iteration of the experiment [56, 58] as well as sufficiently low for loading a dipole trap and where motional dephasing lifetimes of Rydberg states $n > 60$ are comparable to a typical experimental run $\sim 10$ $\mu s$ [119, 160, 58] therefore was deemed sufficient for our purposes. The reduced $\chi^2_\nu$ for the two axes show reasonable agreement between data and theory, and future characterisation should aim to increase the number of samples taken.

### 3.4.3 Optimised Sequence

Though the results in the above section show how the ballistic expansion of an atomic cloud over 10 s of milliseconds can give an estimate on temperature, the sensitivity of cloud size to the myriad parameters present in a cold atom experiment can also prove useful in temperature optimisation. Indeed, at wait times $> 10$ ms, deviations of quantities such as magnetic field currents and cooling powers from optimal can result in a total loss of signal. The size of atom clouds at long TOF wait times therefore served as a final optimisation tool to tweak laser powers and detunings and magnetic field strengths for each stage of the experiment. The sequence to prepare the samples analysed in figure 3.34 is thus shown in figure

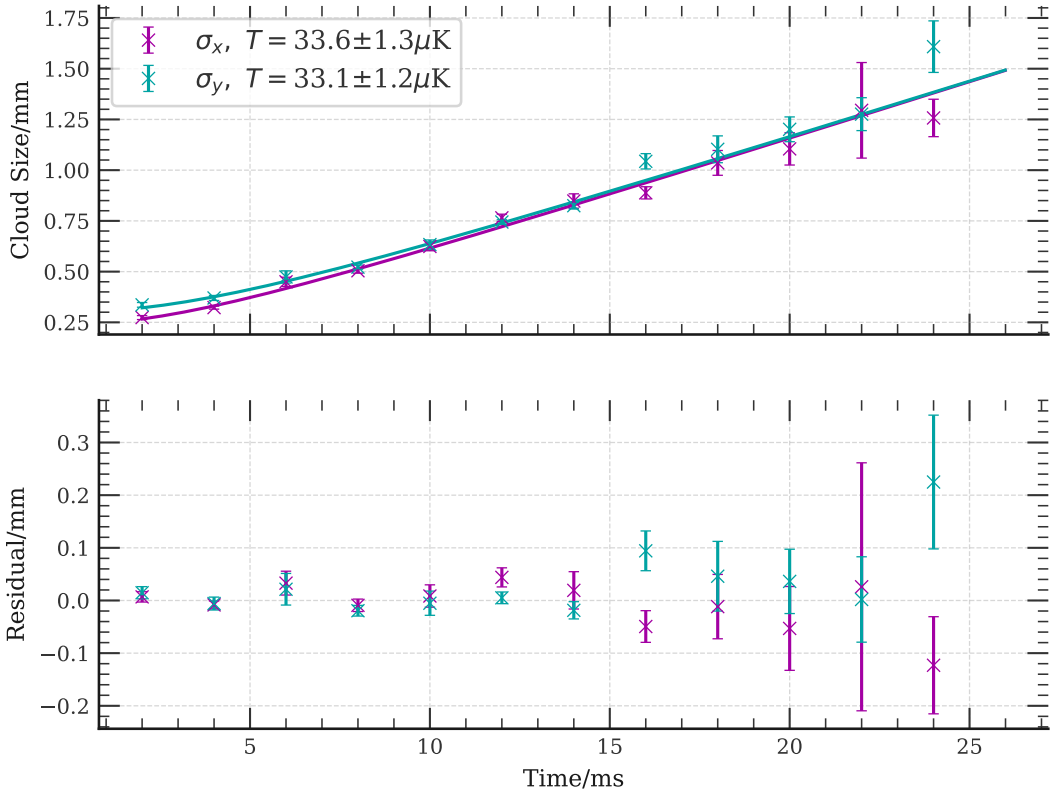


Figure 3.34: **Upper**: Wait time vs cloud size for time of flight temperature measurements for both horizontal (purple) and vertical (cyan) cloud radii. Fittings for both using (3.11) are shown in the solid lines of corresponding colour. The temperatures extracted from the horizontal and vertical radii are $T_x = 33.0 \pm 1.1$ $\mu$K and $T_x = 33.2 \pm 1.2$ $\mu$K respectively. **Lower**: Residual plots for both $\sigma_x$ and $\sigma_y$ from their respective fittings. The reduced $\chi^2_\nu$ for the $x$ and $y$ axis fittings are $\chi^2_{\nu,x} = 1.75$ and $\chi^2_{\nu,y} = 1.97$ respectively.

3.35. Here, laser intensities, detunings and magnetic field gradients are shown in purple, cyan and gold respectively. The sequence begins with an initial MOT load, the length of which is varied depending on the number of required atoms for an experiment. Following this initial load, the MOT field currents are ramped up and the cooling power is ramped down to compress the cloud and increase its density for further cooling. In particular, this compression proves vital for the subsequent optical molasses stage of cooling, where the anti-Helmholtz field gradient is ramped to zero and the atoms remain untrapped. During the ballistic expansion that occurs when the magnetic field is ramped down, the 3D cooling light is left on, to perform a short optical molasses cooling stage. Powers, detunings and fields were ramped where possible to prevent sudden changes of conditions for the atoms and, in the case of the magnetic field, to prevent current ringing. The duration of these ramps were empirically determined using the TOF absorption imaging previously described. Previous iterations of this sequence have a MOT kick stage

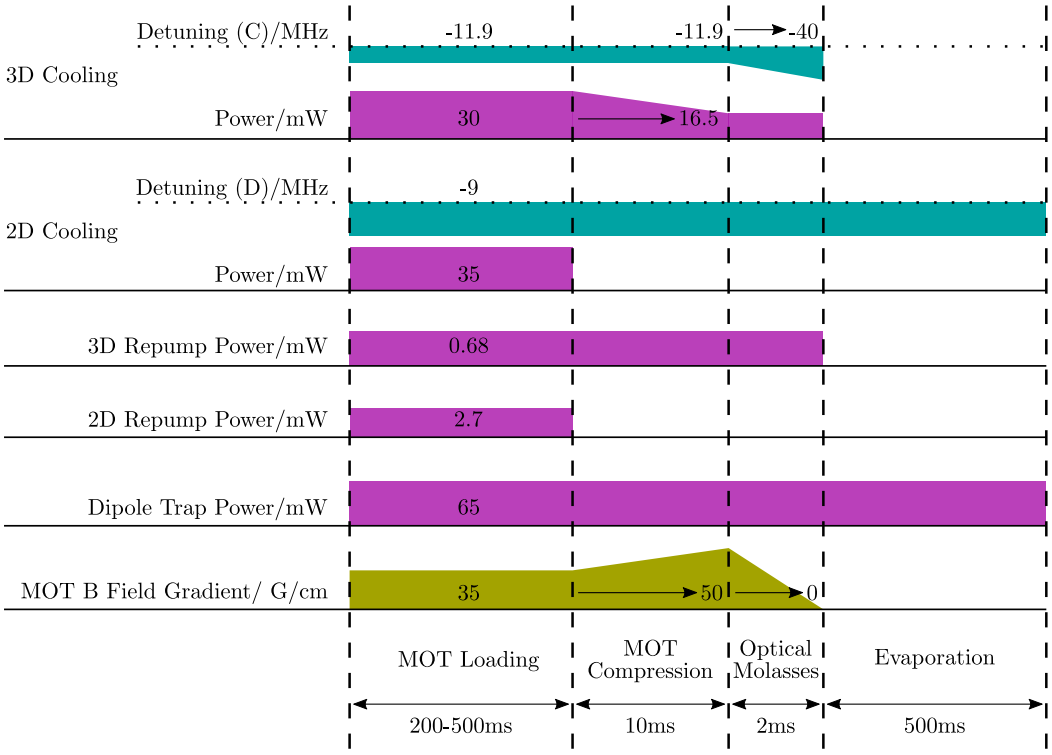


Figure 3.35: Laser intensities (purple), detunings (cyan) and field gradients (gold) throughout an experimental sequence. The lettering (C-D) correspond to that in figures 3.1 and 3.4. The sequence used to prepare the clouds shown in figure 3.33 is identical to this one except instead of an evaporation stage, the two pulses of the imaging beam are triggered with a separation of 50ms to allow the MOT cloud to dissipate.

to expedite the process of removing atoms not trapped in the FORT, however as no experimentation was performed on such a trap, the sequence was simplified to aid in its initial observation. As further repair work is done on this setup, this kick stage would be re-instated to further increase the repetition rate of the experiment. The power for the FORT listed here corresponds to that previously used by N. L. R. Spong [58]. The sequence used to cool atoms to 33 $\mu$K differs from this one shown in figure 3.35 only slightly, as the evaporation stage is replaced by two 100 $\mu$s pulses of resonant light from the image beam. These pulses are separated by a 50 ms wait to allow the MOT cloud to dissipate entirely.

### 3.4.4 Coda - Dipole Trap Fluorescence

Though the final cooling stage and step towards experimental readiness of FORT trapping was unsuccessful, first evidence of such a trap was observed by atomic fluorescence from the trap. This by no means passes for sufficient characterisation

to state that the experimental readiness has been achieved, and characterisation of trap depths, FORT trapped atomic populations, polariton formation and microwave pulses to induce atomic transitions in the Rydberg manifold are necessarily required to make such a statement.

## 3.5 Summary

In this section, the lasers and their locking techniques, alongside the frequency and intensity controls were described. Following this, the initial design including the first iteration of the 2D MOT and in-vacuo components were detailed. The UHV re-evacuation process was described including the changes of components, one of which being the 2D MOT cell. Finally, the optimisation of the 3D MOT temperature and loading rates were detailed.

Further experimental work on this setup is split into three sections: finalising the cooling process by thorough characterisation and optimisation of the FORT stage, Rydberg polariton formation and experimentation in the cloud from the FORT trap and the realisation of the proposed probe for the 2D MOT atomic beam.

# 4 | Qutrit Visualisation

In equivalence to classical computing, Quantum Information Processing focuses primarily on the dynamics of two level systems. Unlike classical computation, however, the quantum bit (qubit) exists not in a discrete space of $\{0, 1\} \subset \mathbb{Z}$ but continuously as a two level wavefunction $|\psi\rangle = \alpha|0\rangle + \beta e^{-i\phi_1}|1\rangle$ in $\mathbb{C}^2$ i.e. existing as a complex, continuously varying object rather than a binary real one. This change in properties allows for significant computational speedup for certain tasks such as the seminal Shor's and Grover's algorithms for prime number factorisation [161] and unstructured searches [162], as well as more recent quantum machine learning [163]. Despite the prevalence of two state dynamics, three states are a key feature in many quantum systems. As mentioned in section 1.3, examples of these include, Raman transitions, STIRAP, EIT and non-linear processes such as frequency doubling and FWM.

Visualisations of quantum systems are highly useful tools to ground abstract dynamics, both for educational purposes when seeing a problem for the first time, or as a framework to illustrate novel results to others. Techniques, such as the Bloch sphere, to visualise two-state processes are well established [93] but extending beyond this, there is growing interest in the visualisation of quantum circuits. Tools such as ZX-calculus allow for clear diagrammatic illustrations of complex processes [164, 165, 166, 167]. Furthermore, with a multi-disciplinary convergence around the development of quantum technologies, visualisation methods can greatly aid in the development of 'quantum literacy' for those without a background in the field [168]. When considering visualising three levels, there is no widely adopted equivalent for three levels although various schemes have been tried [169, 170]. In addition, in the field of quantum computing there is growing interest in three level systems or quantum trits (qutrits) [171, 59, 172, 62, 173]. As the dynamics in a qutrit have the scope to be much richer than their two level counterparts, a framework in which to visually represent a qutrit could provide a useful aid to help intuit the behaviour of a system. Despite the potential use of such a framework,

constructing one is a non-trivial undertaking.

This chapter begins by outlining the most prevalent method of visualising a qubit: the Bloch sphere, before moving on to build on the representation presented in [174] to allow for a description of an arbitrary qutrit state on an 'octant' plot for use both as an educational tool and one for researchers to illustrate novel results. This begins by describing pure states and considering a phase-sensitive interference process in section 4.2. Then in section 4.3 this is extended to fully express an arbitrary mixed qutrit state. Using this framework, a set of common three level protocols are modelled and displayed to visually illustrate their dynamics.

**This chapter is based on the following publication:**

- Max Z. Festenstein. "An Intuitive Visualisation Method for Arbitrary Qutrit States". In: (Apr. 2023). arXiv: 2304.01741

## 4.1 Qubit Visualisation

A two level quantum bit (qubit) wavefunction can be expressed as

$$|\psi\rangle_2 = \begin{pmatrix} \alpha \\ \beta e^{-i\phi} \end{pmatrix}, \tag{4.1}$$

where $\alpha, \beta, \phi \in \mathbb{R}$ and $0 < \phi < 2\pi$. This state can be equivalently expressed as a density matrix of the form

$$\rho_2 = |\psi\rangle_2\langle\psi|_2 = \begin{pmatrix} \alpha^2 & \alpha\beta e^{i\phi} \\ \alpha\beta e^{-i\phi} & \beta^2 \end{pmatrix}. \tag{4.2}$$

This, as well as any other valid density matrix, must be Hermitian, that is $\rho = \rho^\dagger$ as well as positive semi-definite. For both pure ($\mathrm{Tr}(\rho_\mathrm{N}^2) = 1$) and mixed ($\mathrm{Tr}(\rho_\mathrm{N}^2) < 1$) states for N levels, is composed of a linear sum of generator matrices for the Special Unitary Group (SU) (SU(N)). For a qubit of 2 levels, these generator matrices constitute the SU(2) group. In analogy to how any arbitrary N dimensional vector in $\mathbb{R}^\mathrm{N}$ is a linear sum of N orthogonal basis vectors, any N×N pure state density matrix is a weighted sum of basis generator matrices for the SU(N) group. Unlike real space basis vectors, however, the number of generators scales not linearly with N orthogonal vectors for an N dimensional space, but with $\mathrm{N}^2 - 1$ generator matrices for an N×N density matrix. In the case of a density matrix in SU(2) (i.e. a qubit density matrix), these generators are the three Pauli spin matrices. Alongside the

identity matrix which is not itself in SU((2), these are given as

$$\sigma_0 = \mathbb{1} = \begin{pmatrix} 1 & 0 \\ 0 & 1 \end{pmatrix} \quad (4.3a) \qquad \sigma_x = \begin{pmatrix} 0 & 1 \\ 1 & 0 \end{pmatrix} \quad (4.3b)$$

$$\sigma_y = \begin{pmatrix} 0 & -i \\ i & 0 \end{pmatrix} \quad (4.3c) \qquad \sigma_z = \begin{pmatrix} 1 & 0 \\ 0 & -1 \end{pmatrix}. \quad (4.3d)$$

By then assigning each of these generators to an axis in $\mathbb{R}(3)$, any Two Level System (2LS) can be expressed as a vector in this space i.e. within the Bloch sphere. A pure state with coefficients of the SU(2) generators $a_j$ will obey the relation $\alpha_x + \alpha_y + \alpha_z = 1$ and thus lie on the surface of this sphere. A mixed state with $\mathrm{Tr}(\rho^2) < 1$, however, has any loss of coherence represented by reducing the magnitudes of these weightings such that $\alpha_x + \alpha_y + \alpha_z < 1$. This reduces the overall size of the state vector, placing Bloch vector describing the state within the Bloch sphere rather than on its surface. For the pure and mixed states

$$\rho_{\text{pure}} = \frac{1}{4}\begin{pmatrix} 3 & \sqrt{3}\mathrm{e}^{\frac{2}{3}\pi i} \\ \sqrt{3}\mathrm{e}^{-\frac{2}{3}\pi i} & 1 \end{pmatrix}, \quad (4.4a) \qquad \rho_{\text{mix}} = \frac{1}{4}\begin{pmatrix} 3 & \frac{\sqrt{3}}{2}\mathrm{e}^{\frac{2}{3}\pi i} \\ \frac{\sqrt{3}}{2}\mathrm{e}^{-\frac{2}{3}\pi i} & 1 \end{pmatrix}, \quad (4.4b)$$

examples of visualisations with Bloch spheres are shown in figure 4.1.

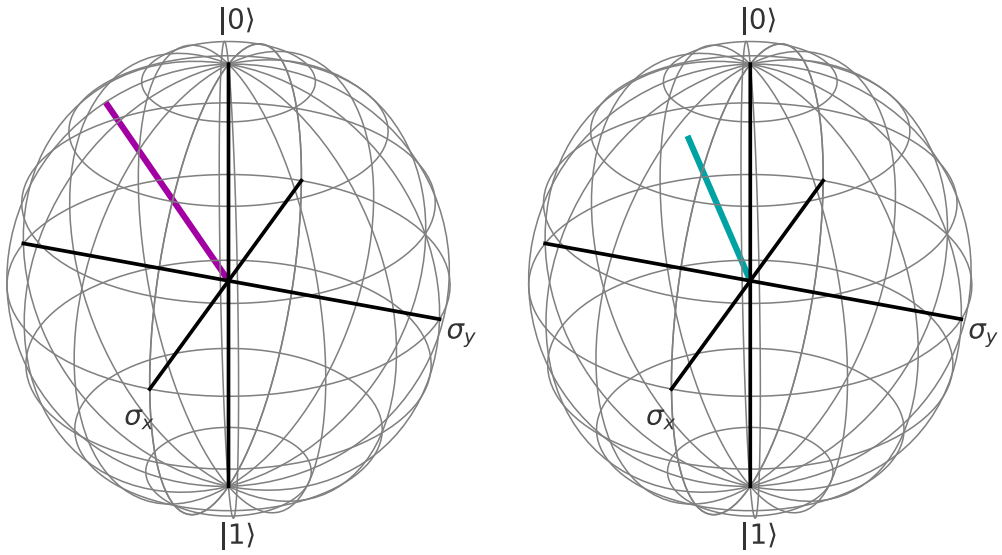


(a) (b)

Figure 4.1: Bloch vectors for the pure (a) and mixed (b) qubit states given in (4.4a) and (4.4b).

An advantage in the SU(2) case is the presence of a double-cover isomorphic mapping from SU(2) onto the three dimensional Special Orthogonal Group (SO) (SO(3)). Isomorphic means a two-way structure preserving correspondence between the two spaces, double-cover referrs to the fact that two points in SU(2) correspond

to a single point in SU(3). The SO(3) group concerns rotations in 3D space, which results in an evolution of the quantum state (an object in SU(2)) being visually represented as a rotation of the state vector around a sphere in real space. A brief derivation of this rotation procedure is given below.

As any Hamiltonian that can be used to dictate the time evolution of a 2 (or more generally N) level quantum system is itself in the SU(2) group, a 2 level Hamiltonian can be expressed as

$$\hat{\mathrm{H}} = \underline{\mathrm{a}} \cdot \underline{\sigma}, \tag{4.5}$$

for the set of Pauli matrices (and identity matrix) $\underline{\sigma} = \{\mathbb{1}, \sigma_x, \sigma_y, \sigma_z\}$ and a vector of coefficients $\underline{\mathrm{a}}$. Utilising these matrices, the Heisenberg Picture time propagator can be represented as

$$\mathrm{U}(t) = e^{-i\mathrm{H}t} = e^{-i\underline{a}\cdot\underline{\sigma}t}, \tag{4.6}$$

where the coefficients $a_j,\ j \in \{0, x, y, z\}$ are the weighting of each of the Pauli matrices. The quantum rotation operator $\mathrm{R}(\Theta)$, which is used to describe rotations of a qubit around the Bloch sphere, has a similar form to this

$$\mathrm{R}(\Theta) = e^{-i\mathbf{J}\cdot\mathbf{n}\Theta}, \tag{4.7}$$

where $\mathbf{J}$ is the angular momentum of the object being considered, $\mathbf{n}$ is the rotation vector and $\Theta$ is the angle of rotation. In our case we have that $\mathbf{J} = \frac{1}{2}\underline{\sigma}$, therefore by re-considering the unitary (4.6) as a rotation operator of the form in (4.7), we can state that

$$-i\hat{\mathrm{H}}t = -i\mathbf{J} \cdot \underline{n}\Theta, \tag{4.8}$$

which then becomes

$$\underline{a} \cdot \underline{\sigma}t = \underline{\sigma} \cdot \underline{n}\Theta. \tag{4.9}$$

As the rotation vector is normalised, the vector $\underline{\mathrm{a}}$ can be described as $\underline{a} = |a|\underline{n}$. Therefore to equate the two expressions, the angle $\Theta$ can be set as

$$\Theta = |a|t. \tag{4.10}$$

Then, by grouping even and odd terms of its Taylor expansion, the operator $\mathrm{R}(\Theta)$ can be expressed as

$$\mathrm{R}(\Theta) = \sigma_0 \cos(\Theta) - i\underline{n} \cdot \underline{\sigma} \sin(\Theta). \tag{4.11}$$

An important part of this simplification is the fact that $\sigma_j \cdot \sigma_k = \delta_{jk}\mathbb{1}$, which allows all but the scalar terms to be removed from the infinite series. An example of a rotation using the Hamiltonian

$$\hat{\mathrm{H}}_{\mathrm{eg}} = \begin{pmatrix} 0 & \Omega \\ \Omega & \Delta \end{pmatrix}. \tag{4.12}$$

where $\Delta = 0.2\ \Omega$ is shown in figure 4.2.

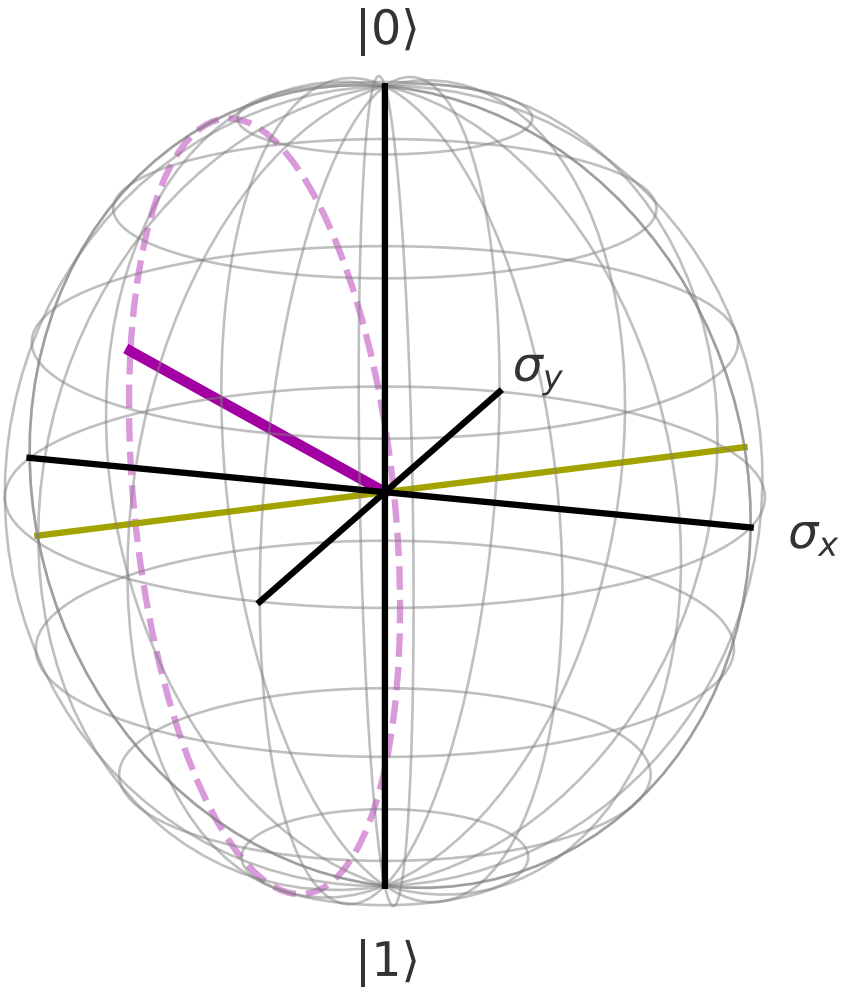


Figure 4.2: Example of a qubit rotation around the Bloch sphere for the test Hamiltonian given in (4.12) with $\Delta = 0.2\ \Omega$. Here, the solid purple line shows the initial Bloch vector for the density matrix in (4.4a), the dashed purple line shows the path it traces as the system evolves in time and the gold line shows the rotation axis defined by the Hamiltonian.

The Bloch sphere is described here in detail to illustrate some of the advantages it offers in understanding the dynamics of the density matrix:

1. It provides a complete description of a 2LS with a clear distinction between pure and mixed states.

2. It is straightforward to interpret with only a basic understanding of QIP.
3. The effect a given Hamiltonian will have on the time evolution of the matrix is straightforward to intuit.
4. Similar (dissimilar) states as measured by either overlap integral for wavefunctions or trace distance for density matrices lie near each other (near opposite poles) on or in the sphere.

Therefore any visualisation method for a Three Level System (3LS) should aim to emulate some or all of these advantages.

## 4.2 Qutrit Visualisation - Pure States

In the 2 level case, an arbitrary density matrix $\rho$ can be expressed as a weighted linear sum of the Pauli matrices, i.e. $\rho = \sum_j \alpha_j \sigma_j$ for coefficients $\alpha_j \in \mathbb{R}$. These 3 Pauli matrices are the generator matrices for the Special Unitary group in two dimensions (SU(2)) and, for 3 levels, the corresponding set of generator matrices for the SU(3) group are the eight Gell-Mann (GM) matrices [175]. The density matrix for any single particle qutrit state can then be expressed as $\rho = \sum_j \mathrm{a}_j \lambda_j$ with coefficients $\mathrm{a}_j \in \mathbb{R}$.

Considering 2 levels, the SU(2) each of the generator matrices, which correspond physically to spin staes, are expressed along 3 orthogonal axes and the qubit state a vector in this space; i.e. a vector on or within the Bloch sphere. Thus for SU(2) it is straightforward to interpret the information being displayed due to the near-direct correspondence of state in $\mathbb{C}^2$ to a position in $\mathbb{R}^3$. Futhermore, this representation offers the ability to distinguish similarity between states; i.e. two similar (dissimilar) states $|\psi\rangle$ and $|\phi\rangle$, where $\phi\psi \approx 1(0)$, will lie close (on opposite poles) to each other on the Bloch sphere. In the 3 level case, however, displaying the full parameter space in a format that is straightforward to interpret becomes a non trivial task due to the 8 independent parameters of the object being described. As such, to reduce the complexity of the initial task, pure states are first considered due to the more straightforward dynamics and reduced dimensionality.

In order to understand the terms being expressed in the visualisation, it is useful to define the 3 level state vector

$$|\psi\rangle_3 = \begin{pmatrix} \alpha \\ \beta \mathrm{e}^{-i\phi_1} \\ \gamma \mathrm{e}^{-i\phi_2} \end{pmatrix} \alpha, \beta, \gamma \in \mathbb{R}. \tag{4.13}$$

This vector can be used to represent a pure state density matrix as in sections 4.1 and, as stated, any arbitrary density matrix $\rho$ can be expressed as a linear sum of the SU generator matrices. For 3 levels, the corresponding set of generator matrices for the SU(3) group are the eight Gell-Mann (GM) matrices [175].

$$\lambda_0 = \mathbb{1} = \frac{1}{3}\begin{pmatrix} 1 & 0 & 0 \\ 0 & 1 & 0 \\ 0 & 0 & 1 \end{pmatrix} \tag{4.14a}$$

$$\lambda_1 = \begin{pmatrix} 0 & 1 & 0 \\ 1 & 0 & 0 \\ 0 & 0 & 0 \end{pmatrix} \tag{4.14b}$$

$$\lambda_2 = \begin{pmatrix} 0 & -i & 0 \\ i & 0 & 0 \\ 0 & 0 & 0 \end{pmatrix} \tag{4.14c}$$

$$\lambda_3 = \begin{pmatrix} 1 & 0 & 0 \\ 0 & -1 & 0 \\ 0 & 0 & 0 \end{pmatrix} \tag{4.14d}$$

$$\lambda_4 = \begin{pmatrix} 0 & 0 & 1 \\ 0 & 0 & 0 \\ 1 & 0 & 0 \end{pmatrix} \tag{4.14e}$$

$$\lambda_5 = \begin{pmatrix} 0 & 0 & -i \\ 0 & 0 & 0 \\ i & 0 & 0 \end{pmatrix} \tag{4.14f}$$

$$\lambda_6 = \begin{pmatrix} 0 & 0 & 0 \\ 0 & 0 & 1 \\ 0 & 1 & 0 \end{pmatrix} \tag{4.14g}$$

$$\lambda_7 = \begin{pmatrix} 0 & 0 & 0 \\ 0 & 0 & -i \\ 0 & i & 0 \end{pmatrix} \tag{4.14h}$$

$$\lambda_8 = \frac{1}{\sqrt{3}}\begin{pmatrix} 1 & 0 & 0 \\ 0 & 1 & 0 \\ 0 & 0 & -2 \end{pmatrix} \tag{4.14i}$$

The density matrix for any single particle qutrit state can then be expressed as $\rho = \sum_j \mathrm{a}_j \lambda_j$ or, (including $\mathbb{1}$) in a single density matrix as

$$\rho = \begin{pmatrix} \frac{1}{3} + \mathrm{a}_3 + \mathrm{a}_8/\sqrt{3} & \mathrm{a}_1 - i\mathrm{a}_2 & \mathrm{a}_4 - i\mathrm{a}_5 \\ \mathrm{a}_1 + i\mathrm{a}_2 & \frac{1}{3} - \mathrm{a}_3 + \mathrm{a}_8/\sqrt{3} & \mathrm{a}_6 - i\mathrm{a}_7 \\ \mathrm{a}_4 + i\mathrm{a}_5 & \mathrm{a}_6 + i\mathrm{a}_7 & \frac{1}{3} - 2\mathrm{a}_8/\sqrt{3} \end{pmatrix}. \tag{4.15}$$

Compare this matrix to that of the pure state density matrix for the vector (4.13).

$$\rho_3 = |\psi\rangle_3\langle\psi|_3 = \begin{pmatrix} |\alpha|^2 & \alpha\beta \mathrm{e}^{i\phi_1} & \alpha\gamma \mathrm{e}^{i\phi_2} \\ \alpha\beta \mathrm{e}^{-i\phi_1} & |\beta|^2 & \beta\gamma \mathrm{e}^{i(\phi_2-\phi_1)} \\ \alpha\gamma \mathrm{e}^{-i\phi_2} & \beta\gamma \mathrm{e}^{-i(\phi_2-\phi_1)} & |\gamma|^2 \end{pmatrix}. \tag{4.16}$$

The comparison between the off diagonal terms in the two matrices is direct, as those $\rho_{j\neq k}$ in (4.15) can simply be re-expressed by Euler's formula and changing the independent parameters from $\Re(\rho_{j\neq k})$ and $\Im(\rho_{j\neq k})$ to $|\rho_{j\neq k}|$ and $\phi_{j\neq k}$. Furthermore, the off-diagonal terms $\rho_{12}, \rho_{21}$ display only a phase difference, rather than an independent phase. Therefore in the pure state case no unique information can be represented and this term is omitted from the visualisation, leaving only 2 phasors. Superficially, it appears that the diagonal terms in (4.16) display an extra variable compared to $\mathrm{a}_3$ and $\mathrm{a}_8$ in (4.15). This is not the case, however, as the trace condition $\mathrm{Tr}(\rho) = 1$ is present. The result is that any one diagonal

term can be derived from the other two i.e. $\rho_{jj} = 1 - \rho_{kk} - \rho_{ll}$, preserving the number of required parameters. The comparison between the two forms of the density matrix is made as the latter equation (4.16) is the form that is graphically represented, thus it is necessary to understand the correspondence between the two.

For the pure state case, the description illustrated in [174] is sufficient to fully describe the system. The model used there relied on two plots side by side to show phase and state population separately. The first adjustment made in this representation is to condense the information to a single plot by projecting the phase information as rotated lines centred at the end of the population vector, akin to hands on a clock. An example of a state represented this way is shown in figure 4.3.

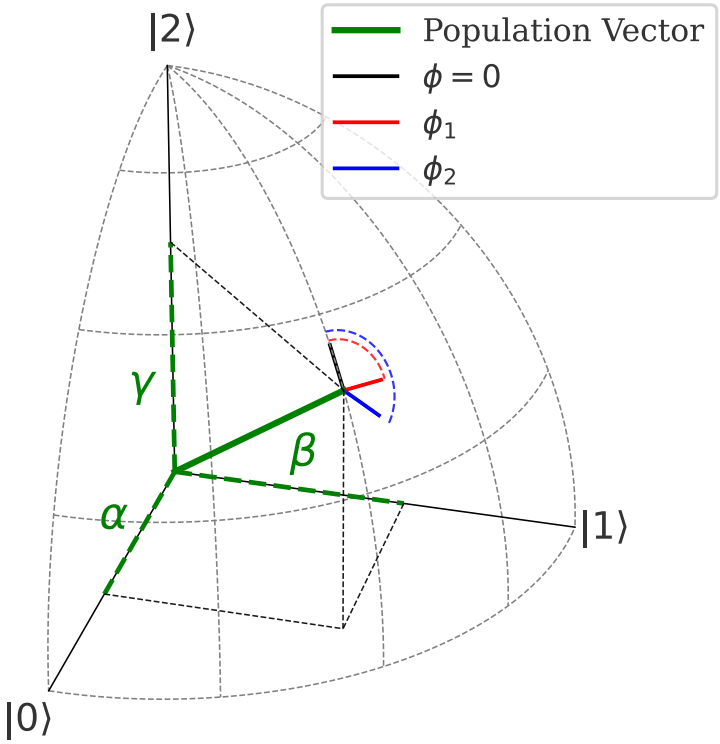


Figure 4.3: Graphical Representation of the density matrix derived from the qutrit vector $|\psi\rangle = \frac{1}{\sqrt{3}}(|0\rangle + e^{-i\frac{\pi}{2}}|1\rangle + e^{-i\frac{3\pi}{4}}|2\rangle)$

There are two exceptions to the general requirement of needing 2 hands to represent a pure state. The first is the trivial case of being entirely in a single eigenstate where there would be no hands present at all; the second is when a superposition is present between only two states, resulting in only one non-vanishing coherent term and correspondingly one clock hand for a vector along any of 3 quadrants between eigenstates. To properly describe a superposition between $|1\rangle$ and $|2\rangle$, the phase

difference $\phi_{12} = \phi_2 - \phi_1$ acts as this single phase term and would warrant inclusion in this instance. To provide a more dynamic example of the evolution of a pure state, a test case using the Hamiltonian

$$\hat{\mathrm{H}} = \begin{pmatrix} 0 & \frac{\Omega_1(t)}{2}(t) & 0 \\ \frac{\Omega_1(t)}{2} & 0 & \frac{\Omega_2(t)}{2} \\ 0 & \frac{\Omega_2(t)}{2} & 0 \end{pmatrix}, \tag{4.17}$$

where $0 \leq t < 75; \Omega_1 = \frac{0.02}{2\pi}, \Omega_2 = 0$ and $75 \leq t \leq 150; \Omega_1 = 0, \Omega_2 = \frac{0.02}{2\pi}$, is shown in figure 4.4. Note that the upper subplots of this figure are, in isolation, described in [174]. In this case, oscillation of population between states appears as harmonic motion of the blue population vector between the two addressed states akin to a pendulum swing, unlike the 2D case where the state precesses around the surface of the Bloch sphere.

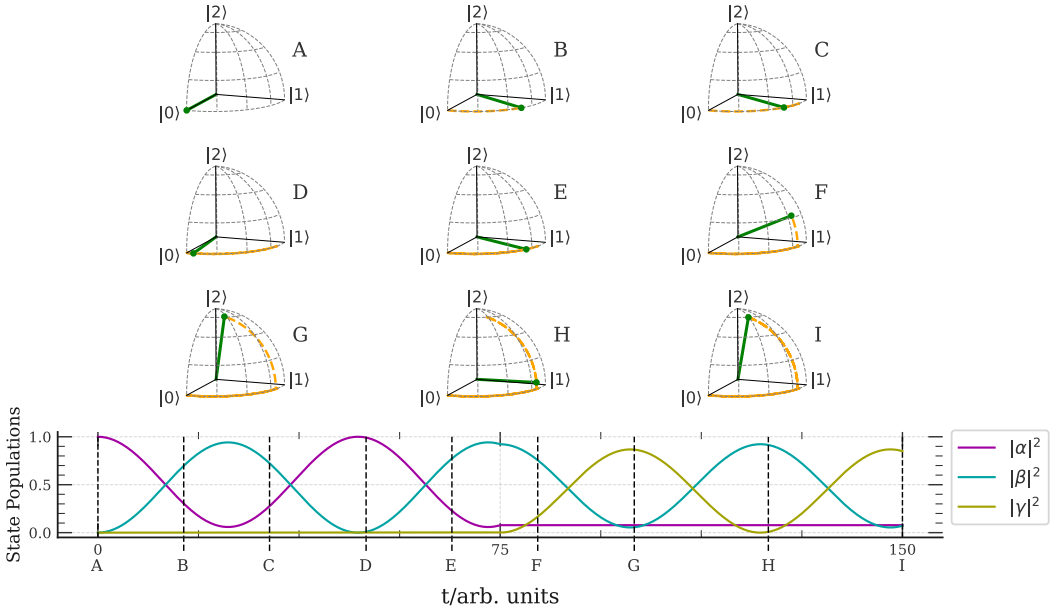


Figure 4.4: **Upper**: Octant plots displaying Rabi oscillations in a 3 level system. No clock hands are included here due to the lack of any oscillation or decay in the resonant case free of decay modes. **Lower**: A more traditional state population vs time evolution of the qutrit as a reference. The times where octant plots are drawn are marked with lettered black dashed lines.

Initially, when the transition between $|0\rangle \rightarrow |1\rangle$ is addressed (A-E) this induces Rabi oscillations between these states, which is visually represented by the population vector oscillating in the x-y plane. When $t > 75$ this Rabi oscillation occurs between $|1\rangle \rightarrow |2\rangle$, which corresponds to oscillation in the y-z plane. As the population transfer to $|1\rangle$ is incomplete when this oscillation occurs, the population vector retains an x axis ($|0\rangle$) component and doesn't experience a full transfer into $|2\rangle$ at the peak of oscillation.

Though this visualisation method shows an individual qutrit state clearly, one shortcoming of the method is the lack of obvious distinction between orthogonal or distant states as measured by trace distance

$$\mathrm{Td}(\rho,\nu) = \frac{1}{2}\mathrm{Tr}\left(\sqrt{(\rho-\nu)^\dagger(\rho-\nu)}\right), \tag{4.18}$$

for two density matrices $\rho$ and $\nu$ where $\sqrt{\ }$ denotes trace norm rather than element-wise square roots. Indeed, it is possible for the representations of two orthogonal states to share the population population vector; as is the case for $|\psi\rangle_+ = \frac{1}{\sqrt{2}}(|0\rangle + |1\rangle)$ and $|\psi\rangle_- = \frac{1}{\sqrt{2}}(|0\rangle - |1\rangle)$. An example of how trace distance between states varies for the starting density matrix from the pure state

$$|\psi\rangle = \frac{1}{\sqrt{3}}\begin{pmatrix}1\\1\\-i\end{pmatrix}, \tag{4.19}$$

by varying only the populations in each state whilst maintaining the same phase is shown in figure 4.5.

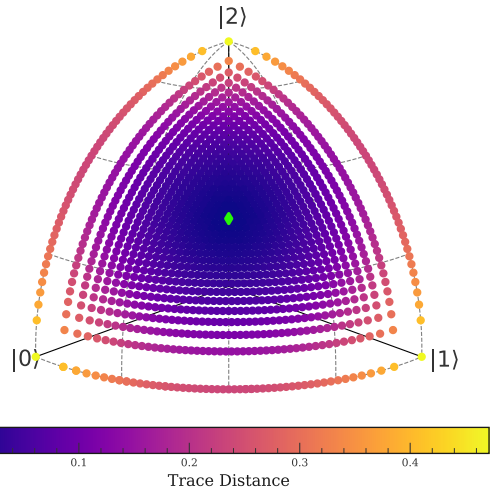


Figure 4.5: Trace distance, as defined in (4.18), between states of equal phase on an octant plot. The green diamond denotes the position of the octant vector for the state in (4.19).

In this plot, the distance between states increases as expected out from the centre, showing that for equal phases, the distance between states can be interpreted as distance between vectors on the octant. For the phase variant case previously mentioned this interpretation is no longer valid.

### 4.2.1 Two-Pulse Sequence

In order to show the effect of phase on a sequence, and how the octant plot can be illustrative in understanding it, a simple two pulse sequence was modelled using the Hamiltonian in (4.17) where the values of $\Omega_1$ and $\Omega_2$ are pulsed according to the sequence in figure 4.6.

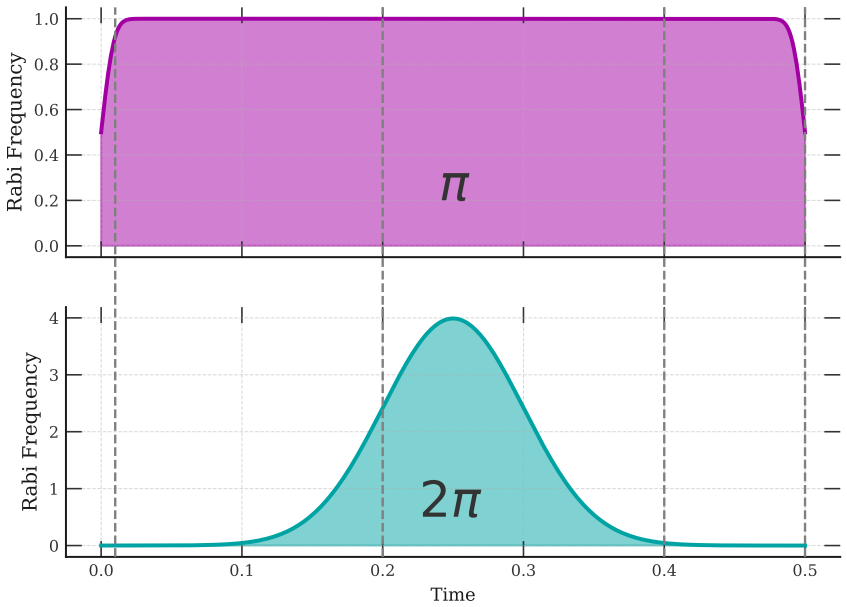


Figure 4.6: Pulse sequence for a simple simultaneous excitation scheme. A $\pi$ pulse is applied to address the $|0\rangle \rightarrow |1\rangle$ transition (blue), and is applied weakly such that the pulse take the entire duration of the sequence to execute. Simultaneously to this, a stronger $2\pi$ pulse addresses the $|1\rangle \rightarrow |2\rangle$ transition (gold) with a Gaussian intensity profile. The grey dashed lines mark the times with corresponding octant plots in figure 4.7.

This straightforward sequence consists of two pulses: a constant pulse addressing the $|0\rangle \rightarrow |1\rangle$ transition that acts as a $\pi$ pulse over the entire duration of the sequence, and a stronger pulse addressing the $|1\rangle \rightarrow |2\rangle$ transition with a Gaussian profile. In the simulation performed, two cases were considered. The first was for the case where no $\Omega_2$ pulse is applied, and the qutrit is allowed to evolve stimulated only by the $\Omega_1$ pulse. The second is when this second $\Omega_2$ pulse is applied. The results for the cases of $\Omega_2 = 0$ and $\Omega_2 \neq 0$ are shown in the upper and lower rows of figure 4.7 respectively.

The sequence in the left column proceeds with a straightforward transfer of population from $|0\rangle$ to $|1\rangle$. As soon as the qutrit leaves the eigenstate $|0\rangle$ and the phasor $\phi_1$ becomes well defined it is immediately set to $\phi_1 = \frac{\pi}{2}$. This is occurs because of the factor of $-i$ that is imprinted on the qutrit by the Schrödinger equation

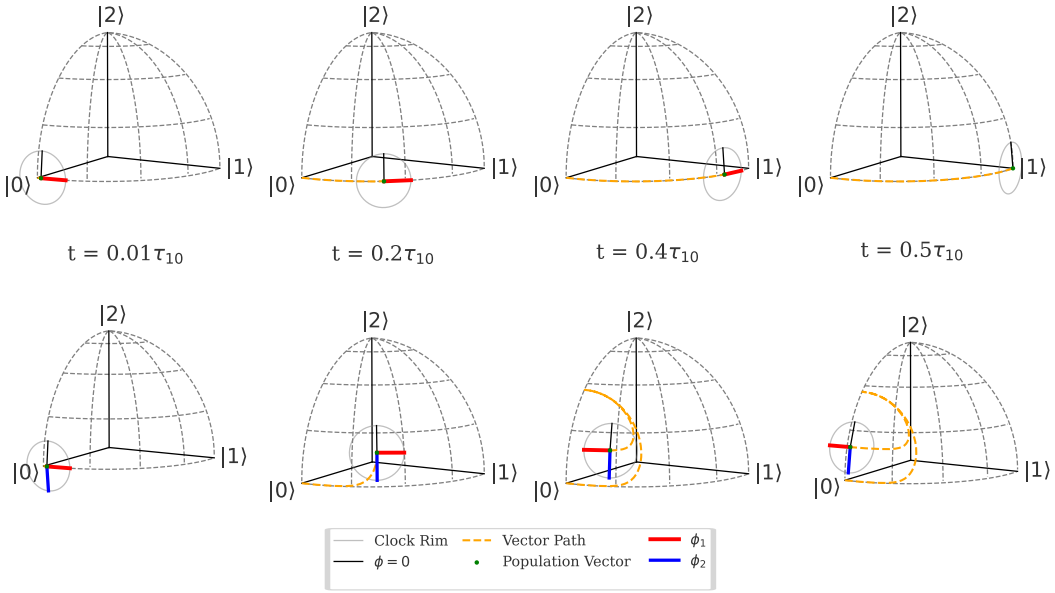


Figure 4.7: Octant plot for the sequence shown in figure 4.6 for $\Omega_2 = 0$ (upper row) and $\Omega_2 \neq 0$ (lower row).

which dictates the time evolution of the system. As the Hamiltonian being applied is entirely real and with no diagonal terms, no further phase evolution occurs and $\phi_1$ remains unchanged for the duration of the sequence. For the $\Omega_2 \neq 0$ case in the lower row, the stimulation of the $|1\rangle \rightarrow |2\rangle$ transition causes all population to transfer out of $|1\rangle$ (as traced by the orange line of the vector path) and into a superposition of $|0\rangle$ and $|2\rangle$. As $\phi_1$ is no longer defined, when population reenters $|1\rangle$, the phase is derived from $\phi_2$ with an additional $\frac{\pi}{2}$ radians again imprinted by the Schrödinger equation. Thus, the overall phase shift in $\phi_1$ is $\pi$ radians from the start of the sequence. This phase shift results in the qutrit evolving under its interaction with the driving field in the opposite direction to the $\Omega_2 = 0$ case and finishes the sequence with no population in $|1\rangle$.

## 4.3 Qutrit Visualisation - Mixed States

In an effectively noiseless, decay-free setting, the description in the previous section is adequate to fully describe any pure 3 level state. This, however, cannot generally be assumed. It is possible to engineer a system to be effectively pure by, for example, utilising either dressed [78] or long-lived atomic states [55], but to create a visual description that fully encapsulates an arbitrary state, we must look to extend the description in section 4.2 to mixed states.

To do this, we consider a more general density matrix than that of the pure state

in (4.16)

$$\rho = \begin{pmatrix} |\alpha|^2 & \mathrm{A}e^{i\phi_1} & \mathrm{B}e^{i\phi_2} \\ \mathrm{A}e^{-i\phi_1} & |\beta|^2 & \mathrm{C}e^{i\phi_{12}} \\ \mathrm{B}e^{-i\phi_2} & \mathrm{C}e^{-i\phi_{12}} & |\gamma|^2 \end{pmatrix}. \tag{4.20}$$

The diagonal elements remain unchanged due to the condition $\mathrm{Tr}(\rho) = 1$ and in the case of standard decay mechanisms and optical driving fields for atomic systems which are the focus of the thesis, the $\rho_{12}, \rho_{21}$ phase $\phi_{12}$ can still be assumed to only show the phase difference between $|1\rangle$ and $|2\rangle$ though outside of atomic systems where extraneous decay mechanisms or 3 driving fields may be possible, this relation is not generally the case. The magnitudes of the off-diagonal terms, however, can no longer be assumed to remain the same due to the introduction of decoherence processes. Therefore the extent of state mixing must be accounted for if the visualisation is to be a complete description. To ensure that no information about the system is lost, the magnitudes of the coherent terms are encoded into the description as the size of the clock hands. In order to remain clear to the reader regardless of the absolute size of populations in the off-diagonal coherence states, these magnitudes ($\mathrm{R}_{jk}$) are normalised as

$$\mathrm{R}_{jk} = \frac{|\rho_{jk}|}{\sqrt{|\rho_{jj}||\rho_{kk}|}}. \tag{4.21}$$

As the magnitudes of the $\rho_{12}, \rho_{21}$ coherences are not themselves related to any other parameter, displaying a third hand to describe this term in the visualisation reveals unique information and warrants inclusion. In the pure state case $|\rho_{j\neq k}| = \sqrt{\rho_{jj}\rho_{kk}}$ (e.g. $\rho_{01} = \alpha\beta$) and in a perfect statistical mixture $\rho_{\mathrm{mix}} = \mathrm{D}_0|0\rangle\langle 0| + \mathrm{D}_1|1\rangle\langle 1| + \mathrm{D}_2|2\rangle\langle 2|$ this coherent term becomes $|\rho_{01}| = 0 \; \forall \; \mathrm{D}_j \in \mathbb{R}$. Thus, in general, $0 \leq \mathrm{R}_{jk} \leq 1$. When a density matrix represents a complete statistical mixture as in $\rho_{\mathrm{mix}}$, this loss of coherence is represented not as a change in length of the octant plot's vector, but as a vanishing of the clock hands from the diagram. With the addition of the description of the state coherences, the diagram possesses the necessary 8 degrees of freedom (accounting for the trace condition $\mathrm{Tr}(\rho) = 1$ removing a degree of freedom) required to fully express the SU(3) generator matrices that constitute any arbitrary qutrit state. A final adjustment to this description for cases where population decays out of the three levels (such as when coupled to a heat bath) would be to shorten the length of the population vector to account for the reduction of overall population in the system being considered. Examples of this effect are not shown here and the discussion will be kept to decay between levels $|0\rangle$, $|1\rangle$ and $|2\rangle$. This description allows a reader to easily interpret: the populations in each eigenstate, the relative phases between them and the degree of state purity via the size of the magnitudes $\mathrm{R}_{jk}$. The normalisation of $\mathrm{R}_{jk}$

terms presents another shortcoming of this visualisation method: by displaying the relative sizes of the off-diagonal coherence state magnitudes, the diagram lacks a measure of the absolute sizes of these off-diagonal terms. Thus the absolute sizes require deduction based on the position of the population vector of the octant and the sizes of the hands $R_{jk}$. Note that even in the case of a fully mixed state the population vector will always remain n the surface of the octant, and only the sizes of hands $R_{jk}$ will vary according to the degree of state mixing.

An example plot for the mixed state

$$\rho = \frac{1}{3}\begin{pmatrix} 1 & \frac{3}{4}e^{i\frac{\pi}{2}} & \frac{1}{2}e^{i\frac{3\pi}{4}} \\ \frac{3}{4}e^{-i\frac{\pi}{2}} & 1 & e^{i\frac{\pi}{4}} \\ \frac{1}{2}e^{-i\frac{3\pi}{4}} & e^{-i\frac{\pi}{4}} & 1 \end{pmatrix}. \tag{4.22}$$

is shown in figure 4.8.

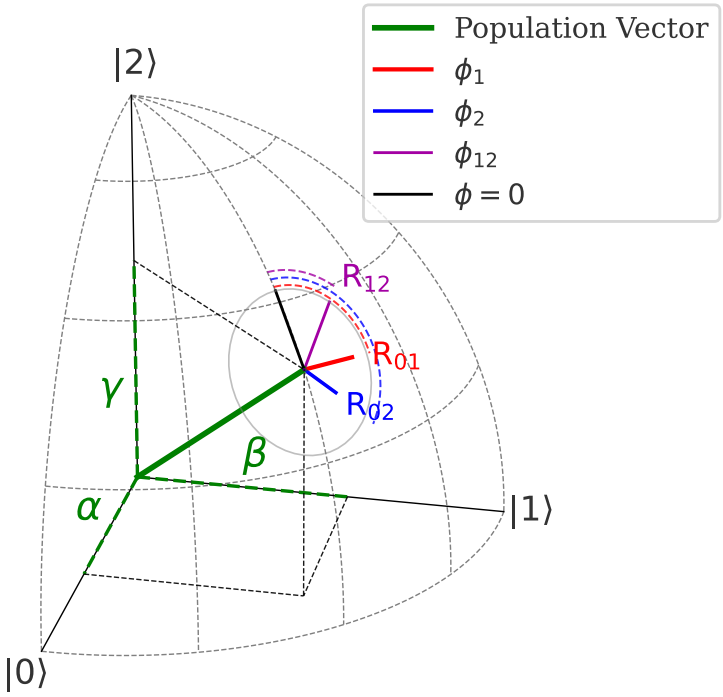


Figure 4.8: Example octant plot for the mixed state given in (4.22).

For the remainder of this work, the three level system under consideration is that of a three level atom, and is shown in figure 4.9.
In this system, state mixing is introduced via radiative decay between neighbouring states, causing a pure state density matrix to evolve into a statistical mixture over time. Mathematically, this is implemented by shifting from a time evolution of a state vector governed by the Schrödinger equation to a Lindbladian master equation

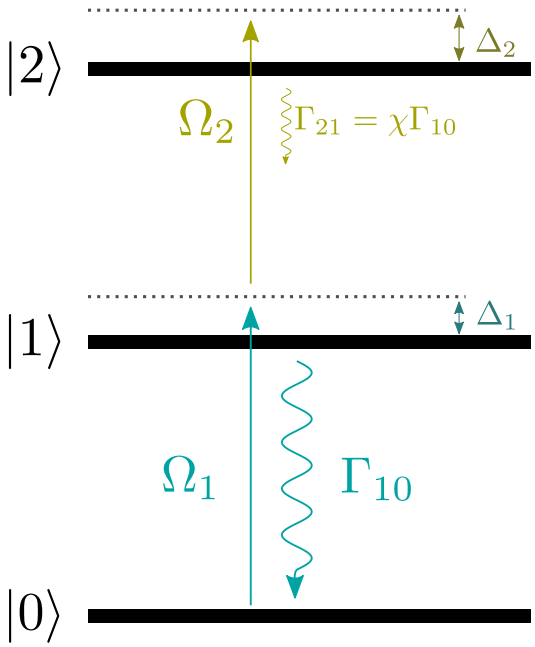


Figure 4.9: Atomic level scheme showing the variables, states and laser fields being considered in modelling. These are: the probe beam ($\Omega_1$) addressing the $|0\rangle \rightarrow |1\rangle$ transition, the coupling beam ($\Omega_2$) addressing the $|1\rangle \rightarrow |2\rangle$ transition, a pair of detuning terms ($\Delta_1$ and $\Delta_2$) and the decay rates $\Gamma_{10}$ and $\Gamma_{21}$. The coefficient $\chi$ is varied between simulations to adjust the extent of the loss of coherence in $\rho_{12}$+c.c..

of the form

$$\frac{d\rho}{dt} = -i[\hat{\mathrm{H}}, \rho] + \sum_{j=1}^{2} \Gamma_{j,j-1} \left( \mathrm{C}_j \rho \mathrm{C}_j^\dagger - \frac{1}{2}\{\rho, \mathrm{C}_j^\dagger \mathrm{C}_j\} \right), \tag{4.23}$$

with collapse operators $\mathrm{C}_j = |j-1\rangle\langle j|$ and $\hbar \equiv 1$. As in figure 4.9 , the mixed state processes are performed with a strong decay mode between $|1\rangle \rightarrow |0\rangle$ with strength $\Gamma_{10}$, corresponding to decay modes present in atomic systems between neighbouring states. As this decay mode is the key defining feature of the system, values of other frequency parameters are quoted in terms of $\Gamma_{10}$, with times in $\tau_{10} = \frac{1}{\Gamma_{10}}$. The decay term $\Gamma_{21}$ is modelled to be a small fraction ($\chi$) of $\Gamma_{10}$ to simulate a long lived upper state such as a Rydberg state. In line with atomic physics, the Rabi frequencies $\Omega_1$ and $\Omega_2$ in figure 4.9 correspond to probe and pump laser radiation fields addressing an atom respectively. By introducing a detuning of a laser field to the simulation, detuning terms ($\Delta_1$ and $\Delta_2$) can be introduced to the diagonals of the system Hamiltonian

$$\hat{\mathrm{H}} = \begin{pmatrix} 0 & \frac{\Omega_1}{2} & 0 \\ \frac{\Omega_1}{2} & -\Delta_1 & \frac{\Omega_2}{2} \\ 0 & \frac{\Omega_2}{2} & -\Delta_{12} \end{pmatrix}, \tag{4.24}$$

where $\Delta_{12} = \Delta_1 + \Delta_2$. The direct connection to atomic physics is made here such that the examples described later in this section can be accurately described in better context.

With this description now complete, some common 3LS processes are outlined as examples to show how system dynamics can be understood using this visualisation. These processes are: EIT, FWM, STIRAP and two-photon Raman transitions.

### 4.3.1 Electromagnetically Induced Transparency

The EIT process is characterised by a sharp increase in probe transmission through a medium under certain resonance conditions. This is present in the response of the medium as a reduced (or zero) excitation via the transition the probe stimulates. The Hamiltonian under consideration is that shown in (4.24) and, in the simplest case where $\Delta_1 = \Delta_2 = 0$, the system forms a dark eigenstate only in terms of $|0\rangle$ and $|2\rangle$, and retains only a coherence in $\phi_2$. This is in line with the values of $\rho_{01}$ and $\rho_{12}$ given in [176] for the case of zero detuning. When $\Delta_{1,2} \neq 0$ we see that the eigenstates, though still analytically solvable, become much more complex and all contain a non-zero population in $|1\rangle$. The time evolution for a resonant (left column) and detuned (right column) EIT sequence is shown in figure 4.10 for $\Omega_\mathrm{p} = \Omega_\mathrm{c} = 2\ \Gamma_{10}$. The Hamiltonian (4.24) acts on the system throughout both cases.

Similiarly to the case in section 4.2.1, the off-diagonal coherence states are initially populated with a $\frac{\pi}{2}$ phase shift imprinted by the Schrödinger equation. This results in the $\rho_{02}$ term immediately acquiring the necessary phase for the dark state rather than tending towards it over time. As the sequence progresses for the resonant case, an initial transient population transfer occurs into $|1\rangle$, with all three coherences present. As the sequence continues, this is transferred into $|2\rangle$ with any residual population in $|1\rangle$ decaying. Alongside this decay of state population out of $|1\rangle$, the coherence terms $\rho_{10}$ and $\rho_{12}$ also decay to zero, leaving only the $\rho_{02}$ coherence. This coherence remains at the value $\phi_{02} = \pi$, leaving the overall qutrit state in the EIT dark state

$$|\psi\rangle_\mathrm{D} = \frac{1}{\sqrt{(\frac{\Omega_2}{\Omega_1})^2 + 1}} \begin{pmatrix} \frac{\Omega_2}{\Omega_1} \\ 0 \\ -1 \end{pmatrix}. \tag{4.25}$$

For the case of $\Omega_\mathrm{p} = \Omega_\mathrm{c} = 2\ \Gamma_{10}$, this state is of the form

$$|\psi\rangle_\mathrm{D} = \frac{1}{\sqrt{2}}(|0\rangle - |2\rangle). \tag{4.26}$$

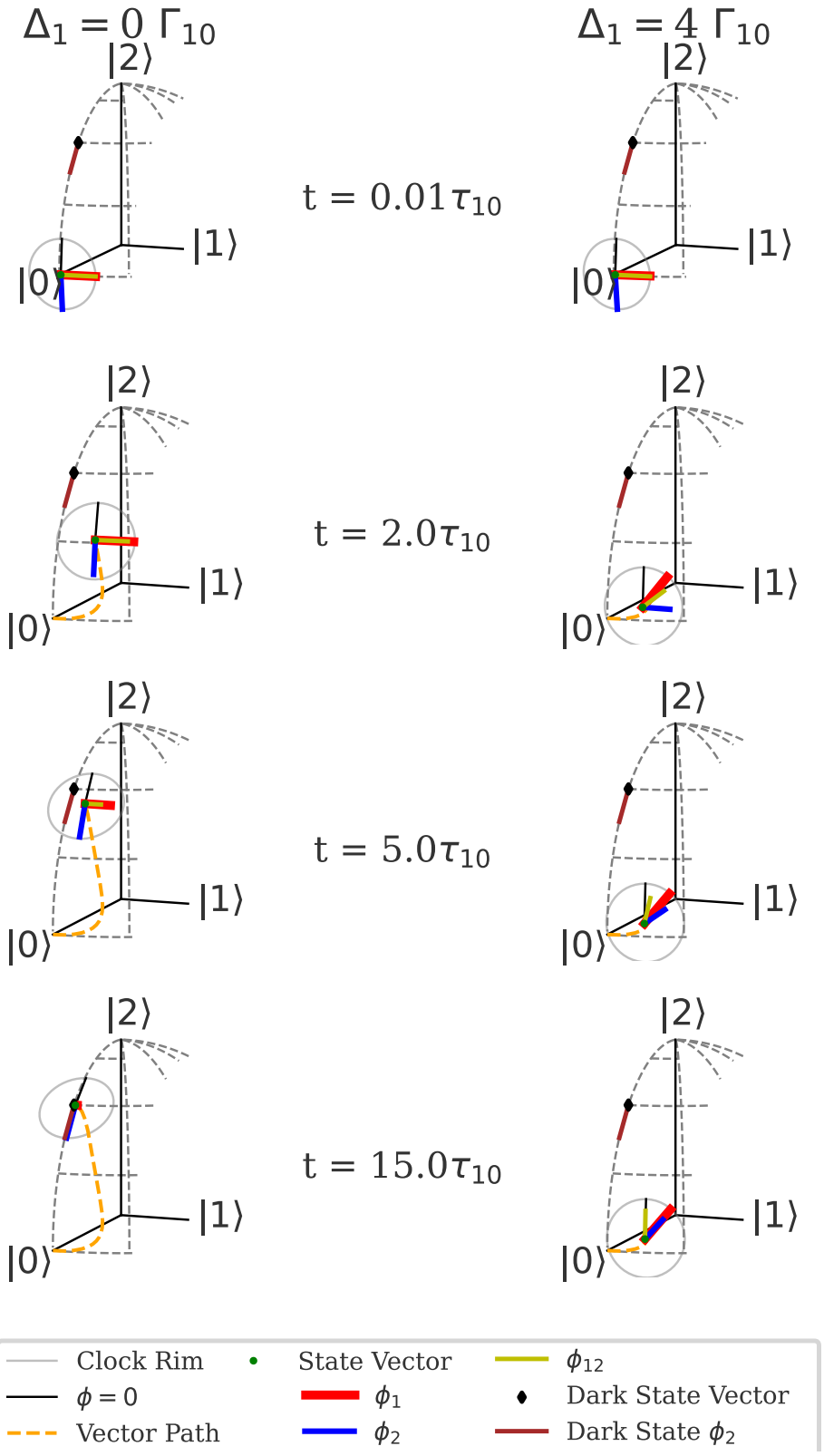


Figure 4.10: Time evolution of a qutrit state for resonant (left) and off-resonant (right) EIT. Here, $\Omega_p = \Omega_c = 2\ \Gamma_{10}$ and $\Gamma_{21} = 35 \times 10^{-6}\ \Gamma_{10}$. The solid black and pink lines shows the population vector and $\phi_2$ for the EIT dark state $|\psi\rangle_D$ in (4.26).

For the off resonant case, the phases on the coherences $\phi_1$ and $\phi_2$ both tend towards $\phi_1 = \phi_2 = \frac{\pi}{4}$, leaving the third phase difference term $\phi_{12}$ tending toward 0 throughout the simulation. As this becomes increasingly phase matched with the driving field, the response of the off-diagonal coherence state to the driving field evermore decreases, preventing population from being driven into $|2\rangle$. Furthermore, in a similar vein to the resonant case, the coherences decrease over time albeit more gradually due to the comparatively small population being excited from $|0\rangle$. Using the octant plot, the dynamics of the EIT process can be clearly visualised. In particular, the coherences can be seen to decay without needing to interpret the small magnitudes of the coherence terms in a density matrix which, if not displayed analytically but instead with floating point variables (as is common for outputs in numerical simulations), may be hard to effectively and easily quantify at a glance. Not only is this magnitude easier to interpret than a numerically displayed complex number in any given off-diagonal, but the phase information is as well; the way that the $\phi_2$ phasor immediately becomes set to $\phi_2 = \pi$ once it is well defined, and that the phasor $\phi_{12} \to 0$ as $t \to \infty$ exemplify this in particular.

### 4.3.2 Four Wave Mixing

The sequence of Four Wave Mixing (FWM) presented here again takes advantage of the decoherence effect of the decay modes in the system in figure 4.9 to clearly display the rich dynamics at play. FWM is a process of great experimental relevance, with applications such as heralded single photon generation [82] and indeed coherent readout of stored photons such as the setup described in chapter 3 [55, 83]. FWM can in principle be performed with four states as in a diamond configuration as in [84], but 3 level ladder systems remain of significant interest [85, 86, 87] and are thus worth discussion here. The pulse scheme considered here is to simulate the storage and retrieval of a photon in an atom and is split into three parts each of equal time t = $\tau_{10}$. In the initial storage (write) time of $0 \leq t \leq \tau_{10}$, both driving fields are present, with the aim being to transfer population into the long-lived $|2\rangle$ state. In the second stage (hold) in the range $\tau_{10} < t < 2\tau_{10}$, no fields are present and the atom is free to decay via the decay modes $\Gamma_{10}$ and $\Gamma_{21}$. In the final stage (read) at times $2\tau_{10} < t < 3\tau_{10}$, driving by the Rabi frequency $\Omega_2$ is resumed, allowing the state to de-populate $|2\rangle$ and decay back to $|0\rangle$ via the strong $\Gamma_{10}$ decay mode. The values of $\Omega_1$ and $\Omega_2$ during this trio of write, hold and read steps are shown in figure 4.11. Throughout this sequence, the $|2\rangle \to |1\rangle$ decay mode is set to $\Gamma_{21} = 1 \times 10^{-3}\ \Gamma_{10}$ such that a slow decay occurs from $|2\rangle \to |1\rangle$

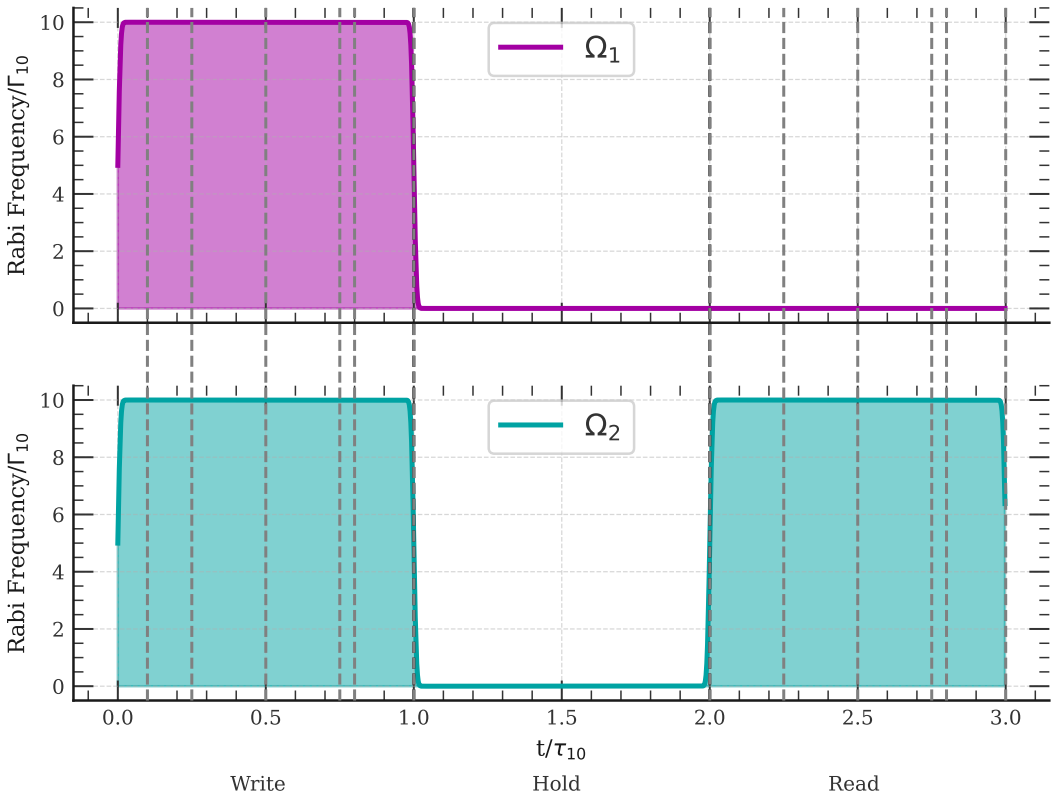


Figure 4.11: Rabi frequencies of the probe and coupling beams in a resonant FWM process. The grey dashed lines show the times during the write (read) stage that are shown in figure 4.12 (4.13).

on the timescale of the simulation. The dashed grey lines in 4.11 during the write stage where both transitions are driven show the times for which octant plots are displayed in figure 4.12. For the second $\tau_{10}$, as neither transition is stimulated and the system is allowed to freely evolve, no plots are shown due to the trivial dynamics of simple $|1\rangle \rightarrow |0\rangle$ decay being the only dynamics of note. In the final $\tau_{10}$, where the $\Omega_2$ drives the upper $|1\rangle \rightarrow |2\rangle$ transition, the dashed grey lines show the times for which octant plots are rendered in figure 4.13. As the coloured elements of the plot correspond to those in figure 4.10 (excluding the dark state components), no additional legend is included in either of these plots. In the first two octants in figure 4.12, an arc is swept out by the population vector due to the simultaneous driving of both transitions. An interesting feature present in these two, as well as the third plot, is the loss in coherence in the $\rho_{20}$ state as indicated by the shrinking blue hand despite the lack of a $\Gamma_{20}$. This feature can be accounted for by considering the $\rho_{20}$ term in (4.23) for no detunings and $\Omega_1 = \Omega_2 = 10\Gamma_{10}$

$$\frac{d\rho_{20}}{dt} = -i \cdot 10\Gamma_{10}(\rho_{10} - \rho_{21}). \tag{4.27}$$

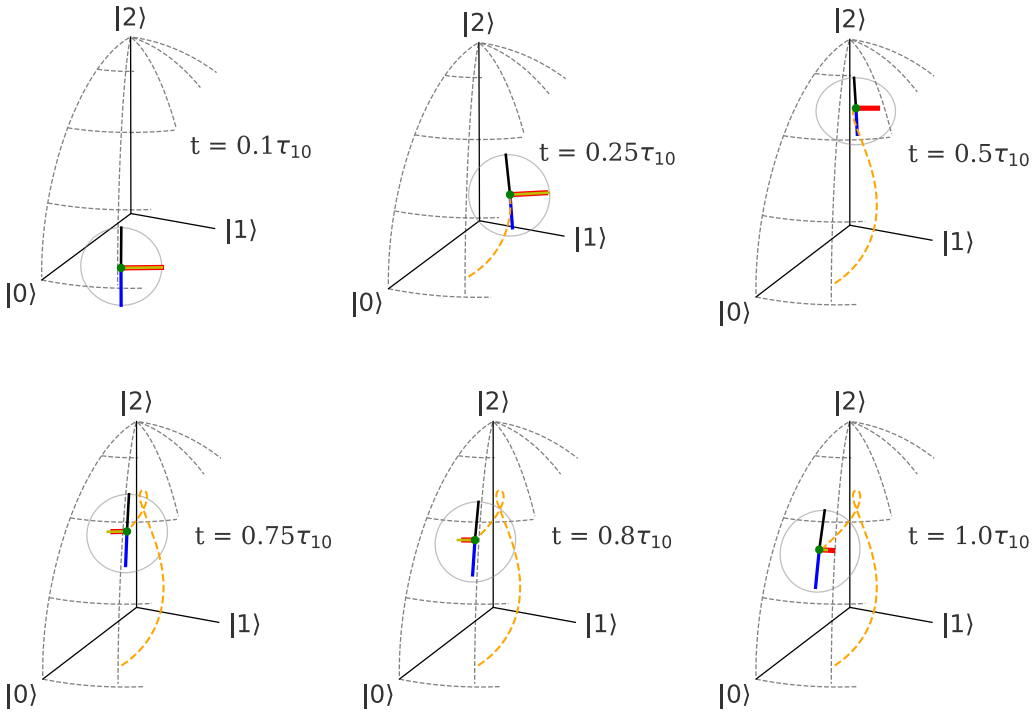


Figure 4.12: Initial dynamics of a FWM process with Rabi frequencies as indictated in the 'Write' stage of figure 4.11. The system begins with an excitation of the qutrit to a long-lived upper state $|2\rangle$. The dotted orange line shows the path traced out by the population vector throughout the write sequence.

Like the cases considered in both sections 4.2.1 and 4.3.1, we have that $\Re(\rho_{10}) = \Re(\rho_{21}) = 0$. This results in a time evolution of the form

$$\frac{d\rho_{20}}{dt} = -10\Gamma_{10}(|\rho_{10}| - |\rho_{21}|), \tag{4.28}$$

thus causing a decay in coherence dependent on the difference between the other coherence terms. Throughout this write sequence the coherence terms with decay modes also oscillate, albeit $\frac{\pi}{2}$ out of phase with the $\rho_{20}$ coherence and decaying in size throughout. In the $\tau_{10}$ time between figures 4.12 and 4.13 the only dynamic of note is the decay of population in the $|1\rangle$ state back to $|0\rangle$, resulting in the red $\phi_1$ hand vanishing entirely. The octant plots in figure 4.13 begin at the end ($t = 2\tau_{10}$) of this hold stage.

During the final decay in figure 4.13, population oscillates between the upper two states while decaying back to ground via state $|1\rangle$. Note that the $\phi_1$ hand returns when population is coherently recovered from the $|2\rangle$ between the first and second plots. The sudden changes in phase as the state oscillates towards $|0\rangle$ are again due to the depopulation of coherence terms resulting in only one phasor being well defined and the other phase terms thus acquiring a $\frac{\pi}{2}$ phase shift from this remaining coherence. The plots in the write sequence elucidate the dynamics of the $\rho_{20}$ term

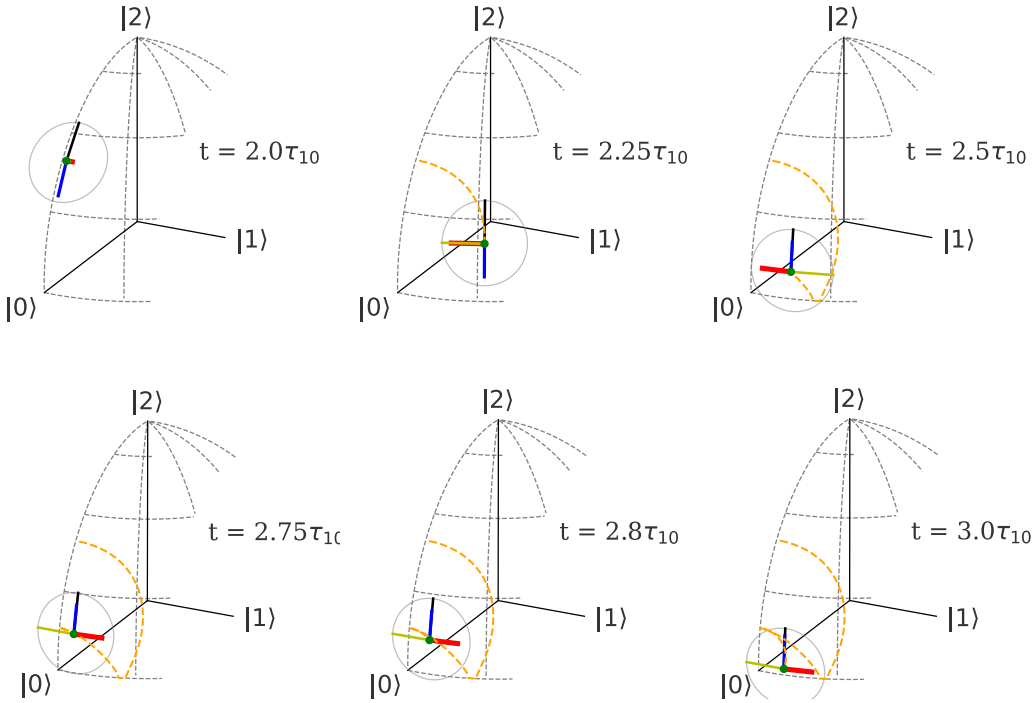


Figure 4.13: End of the FWM process described. Here, the qutrit de-excites from $|2\rangle$ state to the ground state via a strongly decaying intermediate state. The starting state shown here is different from the end state in figure 4.12 as an additional $\tau_{10}$ has passed between the two figures, causing the residual population in $|1\rangle$ to decay. The dotted orange line shows the path traced out by the population vector throughout the read sequence.

which may not initially be obvious when considering the level scheme shown in figure 4.9, and show that even though the other terms decay, the populations oscillate throughout the sequence. Again, these dynamics are not easy to intuit by considering the density matrix alone, and are only made clear by the octant plots for the process. For the latter read stage, the exact path that the qutrit takes back to ground state is shown alongside the phase jumps as the qutrit decays. Though these phase changes are not initially obvious, they have been discussed in the previous examples.

#### 4.3.2.1 FWM - Rydberg Atomic Formation

As stated earlier in section 4.3.2, one of the potential applications of the FWM process is directly related to the experimental platform described in chapter 3 i.e. Rydberg atom creation and photon storage. The process of Rydberg atom formation is modelled using the same pulse sequence as in figure 4.11, albeit with parameters listed in table 4.1 and a pulses as described in figure 4.14

| Parameter | Value |
|---|---|
| $\|0\rangle$ | $5S_{1/2}$ |
| $\|1\rangle$ | $5P_{3/2}$ |
| $\|2\rangle$ | $60S_{1/2}$ |
| $\Gamma_{10}$ | $2\pi \cdot 38.11$MHz |
| $\Gamma_{21}$ | $2\pi \cdot 1.34$kHz |
| $\Delta_1$ | 0Hz |
| $\Delta_2$ | 0Hz |

Table 4.1: Parameters used to simulate a Rydberg atom formation sequence. Here, the beam waists, powers and valence electron energy levels correspond to those utilised in [44].

As the experimentally implemented sequence assumes only a single photon addresses an atomic ensemble in a given run, the Rabi frequency applied in the three level Hamiltonian (4.24) needs to account for this. This is achieved by assuming only one quantum, $E = \hbar\omega_{\text{photon}}$, of energy is transferred over the course of the write sequence. Thus the Rabi frequency is derived from this energy profile with a beam waist as quoted in [44]. Utilising these parameters, the pulse sequence for the process is shown in figure 4.14. In this sequence, the pulse timings correspond to those typically experimentally implemented using the apparatus described in chapter 3. The rise times of 10ns for the pulses correspond to the rise times of the AOMs used to experimentally control laser intensities. The grey dashed lines show the times for which octants are plotted in figure 4.15.
This sequence proceeds in a similar vein to the general FWM sequence shown in figures 4.11, 4.12 and 4.13 with the main differences deriving from the comparative strength of Rabi frequencies. Whereas the sequence in section 4.3.2 had Rabi frequencies $\Omega_1 = \Omega_2 = 10\Gamma_{10}$, this sequence is modelled directly after the experiment described in this work and has $\Omega_{1,\text{peak}} = 0.18\ \Gamma_{10}$ and $\Omega_{1,\text{peak}} = 0.81\ \Gamma_{10}$. Thus, the degree to which the qutrit is excited out of $|0\rangle$ initially is greatly reduced, leading to only a small population transfer out of the ground state during $0\text{ns} < t < 250\text{ns}$. For the first 200ns, this population is transferred into $|2\rangle$ by the stronger coupling beam and for the remaining 50ns before the probe beam is switched off, a transient population transfer between $|0\rangle \rightarrow |1\rangle$ occurs. Due to the strong decay mode, however, the population in $|1\rangle$ quickly decays back to ground. At $t = 350$ns, the $|1\rangle$ state is completely depopulated, leaving only $R_{02} \neq 0$. Then, once the coupling beam $\Omega_2$ re-illuminates the qutrit, the residual excited population decays back down to $|0\rangle$ via the intermediary $|1\rangle$. Phase jumps occur in an equivalent manner to the previous examples throughout the sequence whenever any one of the eigenstates are completely depopulated. Though only a small population is initially excited out of $|0\rangle$, and thus resulting in only a small probability of exciting

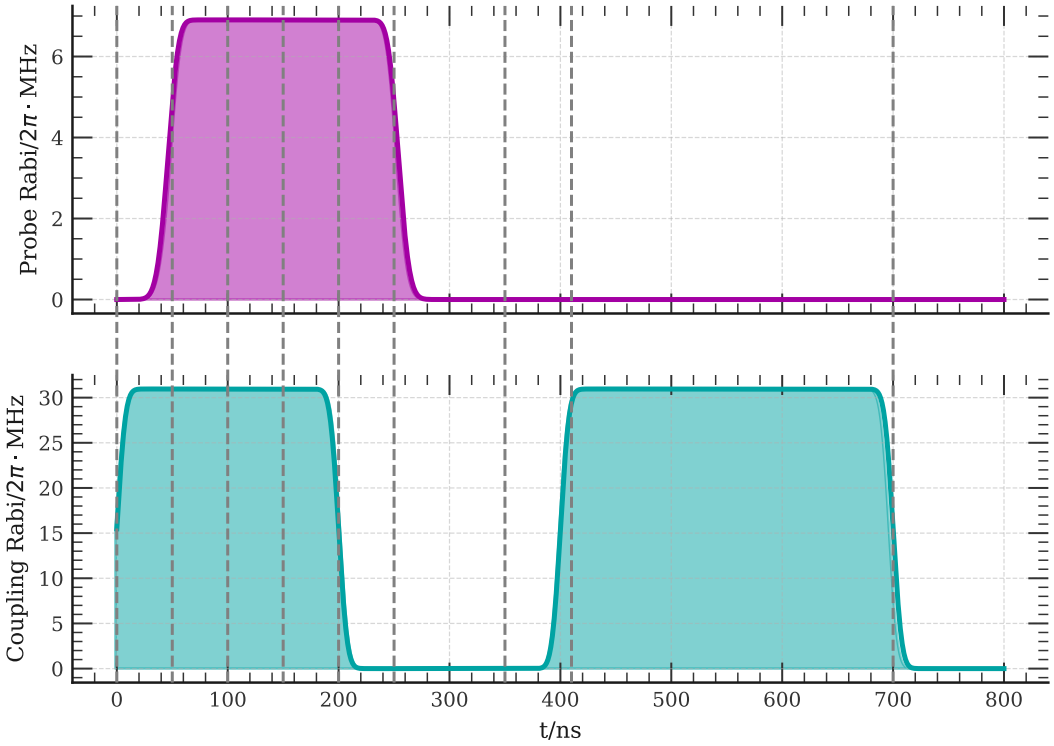


Figure 4.14: Pulse sequence for the simulated Rydberg atom formation. In line with section 2.3.2, the probe beam is switched on and off after the equivalent steps for the coupling beam to ensure that any atom that is excited to the $5P_{3/2}$ state is further excited to the $60S_{1/2}$ state. The grey dashed lines shown here denote the times where octant plots are shown in figure 4.15.

to a Rydberg state, the high repetition rate of the experiment ($\sim$ 10kHz) ensures that an excitation does occur during the course of an experimental run of $\sim$10000 repetitions.

### 4.3.3 Stimulated Raman Adiabatic Passage

The final example shown here is that of STIRAP, which is an invaluable technique for population transfer for a wide range of purposes such as generation of Rydberg atoms [77] as well as ionic qubit state [78], rovibronic ground state molecule [79] and coherent spatial state preparation [80]. As is often the case during a STIRAP process, the aim of the sequence is to coherently transfer population from a starting state ($|0\rangle$) to an end state with no available direct transition ($|2\rangle$) via a strongly decaying intermediate ($|1\rangle$. To avoid populating $|1\rangle$ during the STIRAP sequence, the powers of the coupling beams for the transitions $|0\rangle \rightarrow |1\rangle$ and $|1\rangle \rightarrow |2\rangle$ are

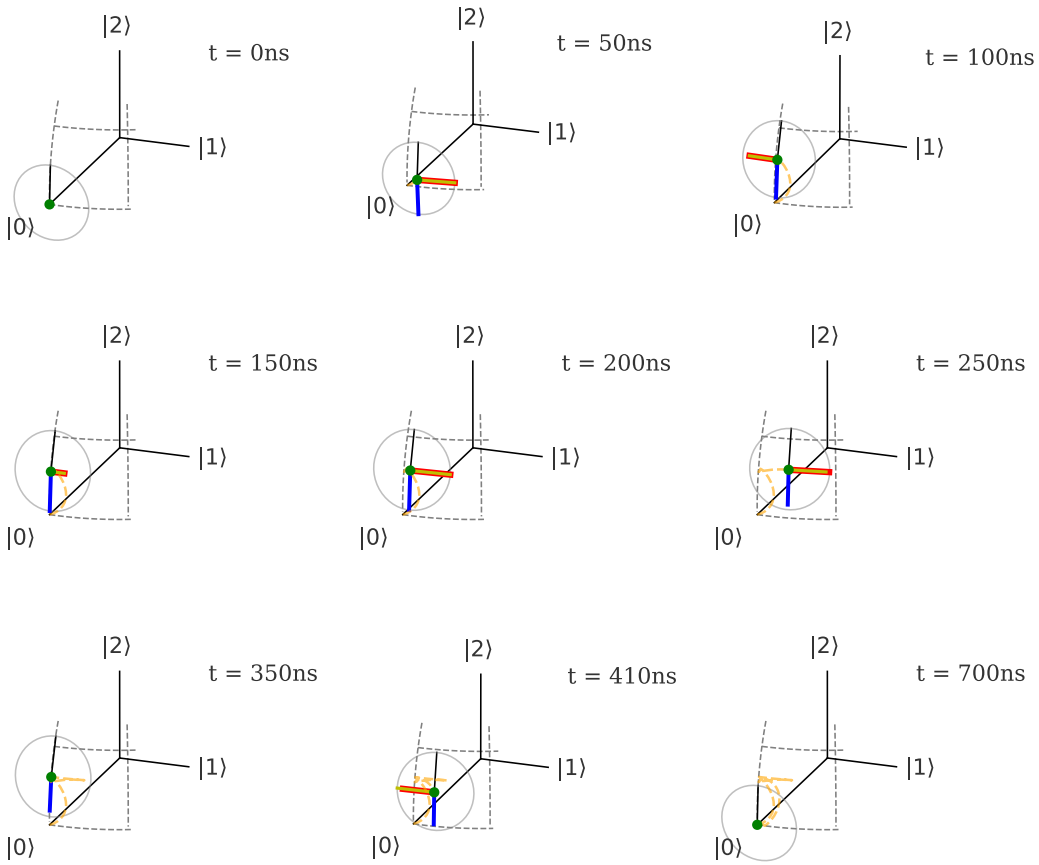


Figure 4.15: Octant plots for the Rydberg excitation sequence shown in figure 4.14. The sequence proceeds in a similar manner to the more general FWM process, but with greatly reduced population transfers. This is due to the small Rabi frequencies; on the $|0\rangle \rightarrow |1\rangle$ transition this is due to the single photon incident in the system, and on the $|1\rangle \rightarrow |2\rangle$ transition this is due to the comparatively small electron dipole moment between the initial and target states as given in (2.7). An additional difference between the sequences is the much greater decay out of $|1\rangle$ due to the proportionally much smaller Rabi frequencies when compared to the $\Gamma_{10}$ decay rate.

ramped over time with the latter of these transitions being ramped first. This pulse sequence is shown in figure 4.16.

Using this pulse sequence in the Hamiltonian (4.24) for the level scheme in figure 4.9, the octant plots for the marked times in figure 4.16 are shown in figure 4.17.

To simulate a long lived atomic state $|2\rangle$ the parameters match those in section 4.3.2.1, though remain naturalised to $\Gamma_{10}$. Here, the population transfer occurs almost exclusively between $|0\rangle$ and $|2\rangle$, however due to the strong decay mode present between $|1\rangle \rightarrow |0\rangle$, any small amount of population that is transferred into $|1\rangle$ decays back to $|0\rangle$ immediately. This results in a loss of coherence in the $\rho_{01}$ state and

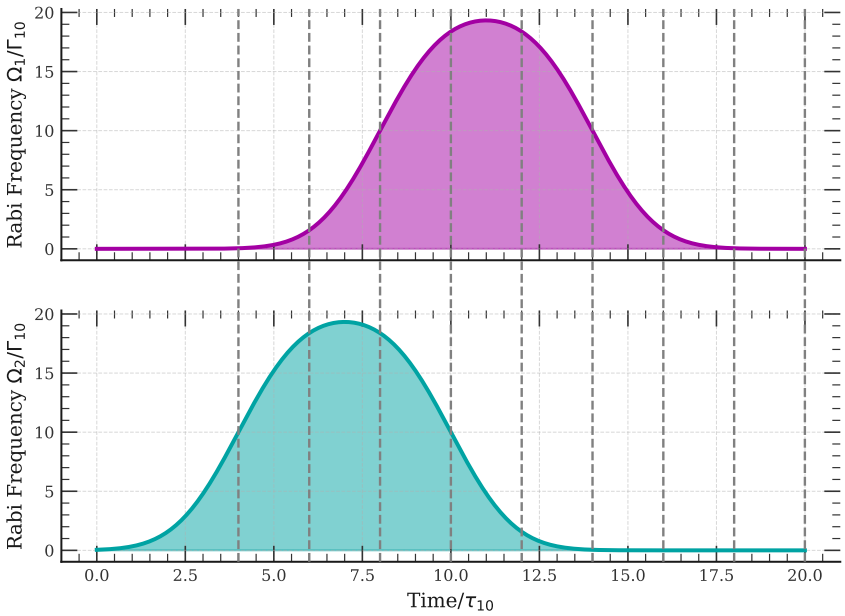


Figure 4.16: Rabi frequencies addressing the $|0\rangle \rightarrow |1\rangle$ (purple) and $|1\rangle \rightarrow |2\rangle$ (teal) transitions. The grey dashed lines mark the times shown in figure 4.17.

the red hand on the clock face shrinks as the system evolves in $4\ \tau_{10} < t < 12\ \tau_{10}$. At time $t = 16\ \tau_{10}$, the coherence is restored due to a small transfer of population into $|1\rangle$ as the $\Omega_1$ pulse tails off. This again illustrates the shortcoming of not being able to display absolute sizes of the coherence terms, as even such a small transfer results in a full length hand $R_{01}$. Over the next two plots shown, this again dies off and the qutrit is left in a statistical mixture of $\rho_{\text{end}} = D_0|0\rangle\langle 0| + D_2|2\rangle\langle 2|$ where $D_0 \gg D_2$.

As in the previous examples, the octant plots aid in displaying the dynamics of the off-diagonal terms: both phases and relative magnitudes, as well as showing the paths traced by the qutrit population vector throughout the sequence thus displaying the level of transfer into $|1\rangle$ during the sequence. Thus the plots could be used as a visual aid in optimising the STIRAP sequence such that population transfer into $|1\rangle$ is minimised.

To summarise this chapter, an intuitive formalism with which to visualise any arbitrary pure or mixed qutrit state has been presented. Test cases were examined to explore and illustrate their internal dynamics with non-trivial phase changes and coherence decays clearly illustrated by the octant plots. Though it is relatively straightforward to interpret the constituent elements of 3 level density matrices, the aforementioned limitations of this visualisation method are not well explored here and could be presented in future work.

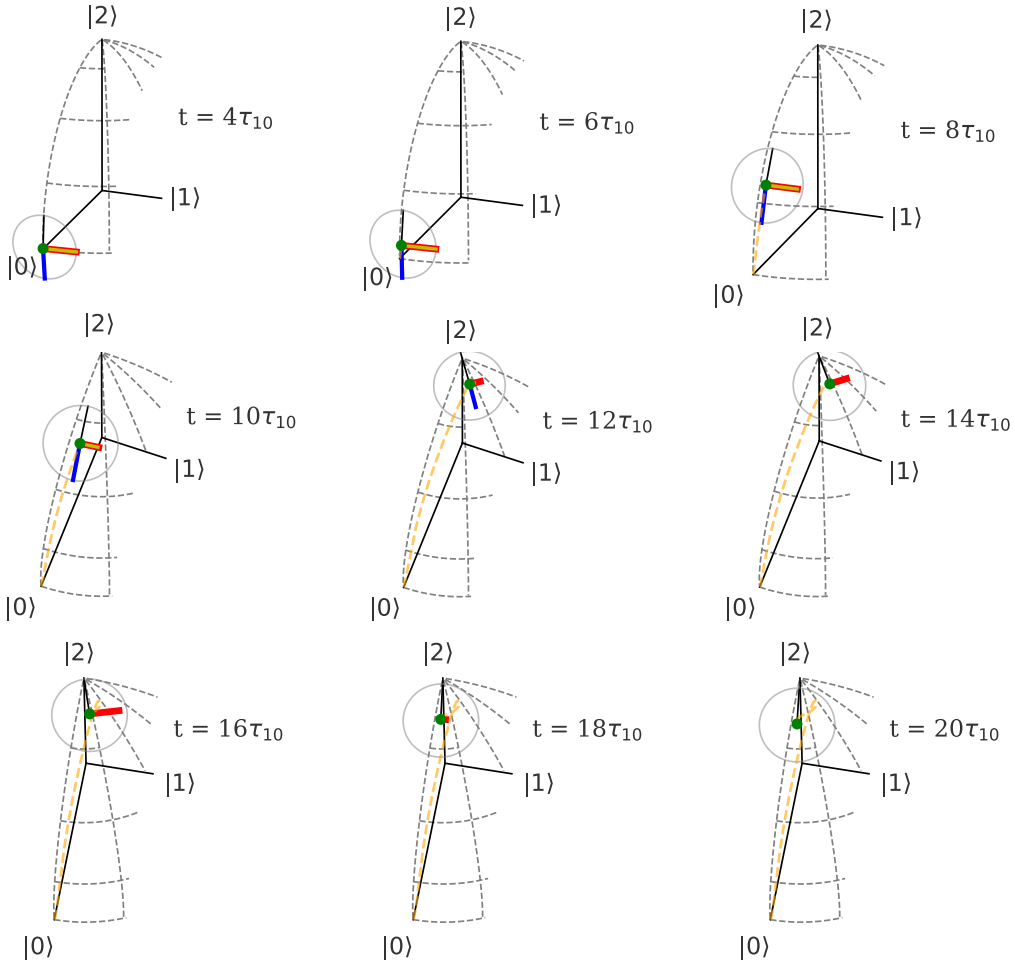


Figure 4.17: Three level system undergoing a STIRAP protocol. The peak values for Rabi frequencies are $\Omega_{1,2} = 20\ \Gamma_{10}$ with a decay rate from state $|2\rangle$ of $\Gamma_{21} = 35 \times 10^{-6}\ \Gamma_{10}$ which corresponds to the ratio of the decay rates in the Rydberg system modelled in section 4.3.2.1. Note that the variables and their corresponding colours stated in the legend in figure 4.10 (excluding the dark state terms) remain unchanged and no legend is included here.

# 5 | Conclusions and Outlook

In summary, this thesis has detailed an experimental platform used to experiment on ultra-cold clouds of $^{87}$Rb excited to Rydberg states. The slight alteration from the design described by H. Busche in [56] were outlined, as well as the steps undertaken to return the setup to a state of experimental readiness from atmospheric pressure to the formation of atomic clouds 33$\mu$K in temperature. In addition to the experiment, a framework with which to visualise any arbitrary qutrit (three level) state was outlined, and example processes were modelled to illustrate the value of the visualisation method in aiding understanding of the arising phenomena.

## 5.1 Theory

This chapter begins with a description of the light-matter interactions at the core of the experiments described, beginning with a two level atom. It is at this point where essential parameters such as the dipole moment operator (2.5 and Rabi frequency (2.7) are defined.

Following this, the three key stages of the optical trapping performed in the process preceding Rydberg atom formation: MOT cooling, sub-Doppler cooling and FORT trapping, are described. Finally, Rydberg atoms are defined, and their desirable properties, and how they change with principle quantum number $n$, are stated. The process of forming a collectively encoded Rydberg atom in our experiment is then described.

## 5.2 Experimental Apparatus

The particulars of the experimental setup are outlined in this chapter. It begins with a description of the laser systems used in experimentation, describing the nature and purposes of each. The mechanism by which these are intensity and fre-

quency controlled: via AOMs, is then described. The design of the chamber itself is then detailed, commencing with the design of the upper 2D MOT cell followed by that of the lower science chamber and the software used in the fast control of the optical components.

This chapter continues with a section dedicated to the re-evacuation process following an unplanned vacuum break. This multi-step process is outlined before the components relevant to the repair process are listed. As the ion pump had indicated faults prior to the vacuum break, this component was independently re-characterised, performing the conditioning and activation processes whilst directly attached to the external vacuum pumping rig. Once the continuing functionality of the pump was confirmed, the components needing replacements were cleaned where necessary and assembled. Assembly consisted of both affixing *in-vacuo* or connecting components directly to the chamber via DN16/DN40 flanges, or spot welding to connection wires. This is followed by the initial pump down, leak testing and bakeout procedures. The (initially erroneously performed) dispenser activation process is outlined, with graphs showing the partial pressure of Ar and $^{85}$Rb displayed in figure 3.18. Following the activation, several attempts were made to clear the Rb deposits on the interior walls of the 2D MOT cell and are outlined. Finally, figure 3.24 shows the entirety of the second evacuation process from start to finish.

With a suitably evacuated chamber, work then commenced on optimising both the atomic loading rates and cloud temperature of the initial stages of optical trapping. The first of the two main techniques utilised to achieve this were atomic fluorescence, measured using a commercial PD, the voltage outlput of which was converted to an atom number via (3.6). The second was resonant absorption imaging, where cloud positions and sizes were recorded in TOF measurements to measure both cloud position (for shim coil current optimisation) and cloud radius (for ballistic expansion measurements) and a temperature of 33$\mu$K was measured through a fitting of (3.11) to cloud size for varying wait times in TOF measurements.

The intricacies of the range of equipment and techniques utilised in progressing toward experimental readiness showed that the value of hands-on, practical experience cannot be overstated. This work also revealed that knowledge transfer of these finer details is vital for the continued functioning of complex cold atom experiments such as this. Another, more specific conclusion to be drawn from this thesis is the import of not following previous cup-type dispenser activation procedures too closely to the letter. The variation in electrical connection between welding

wire and dispensers needs to be appropriately accounted for with sound judgement. Finally, due to the extremely narrow margins for error in achieving temperatures suitable for experimentation, the value of patience, rigour and persistence were acutely highlighted.

## 5.3 Qutrit Visualisation

A visualisation method with which to understand any arbitrary qutrit state is presented in this chapter. It begins with a section outlining the seminal Bloch sphere for qubit visualisation, noting how the framework displays the qubit state clearly for both pure and mixed states. Following this, the transition is made to qutrits starting with the simplest pure state case. The components of the visualisation for a pure state are detailed here, and a simple phase dependant sequence is modelled and displayed.

The extension is then made to fully describe an arbitrary mixed state, with several atomic processes of interest being modelled. These are: EIT, FWM (including the particular case of a Rydberg excitation) and STIRAP. These processes are included such that one may see how the visualisation method elucidates the dynamics at hand.

This visualisation allows a reader to understand a state of the 8D qutrit at a glance, and conveniently determine state populations, relative phases between states and degree of state mixing.

## 5.4 Outlook

On the experimental setup, the main tasks to be undertaken proceeding those documented here are:

- Finalising the cooling process through a thorough optimisation and characterisation of the FORT trapping stage akin to that performed by S. Ball and H. Busche [57, 56].
- Optimising the preparation stage of the trapped cloud to maximise the probability of absorbing a probe photon in the first step of the excitation process described in section 2.3.2.

- Ensure the cloud stores only a single photon by performing second order correlation function $g^{(2)}$ measurements [91].
- Characterise the linewidth of the PDH-locked 480 nm Rydberg excitation laser to allow for accurate blockade radius calculations.
- Re-characterise the microwave sources used to coherently drive population between Rydberg states, as these have gone unused for this purpose for 3 years at time of writing.
- Extend the qubit described by N. L. R. Spong *et. al.* in [44] to a third state and demonstrate qutrit dynamics with a collectively encoded Rydberg atom. Work was performed by Y. Jiao to achieve this, but no works have been published at time of writing.

An additional avenue to be explored is the inclusion of a horizontal 2D MOT probe beam, which would intersect the atomic beam after the differential pumping tube via the windows on the cross piece shown in figure 3.12 that replaced the DN16 connecting gate valve. This probe could see use in providing a real-time measurements for atom number via the depth of absorption features and temperature by their Doppler broadened linewidths.

Further work could be performed on the qutrit visualisation in exploring methods to incorporate decay modes out of the three levels being visualised, or in modelling phenomena in non-atomic systems, where transitions between any two states are possible. One additional, more complex task in expanding the scope of the visualisation would be to incorporate Hamiltonians into the visualisation methods. In the Bloch sphere, this is done elegantly. The Hamiltonian is displayed as a vector with its constituent (normalised) coefficients for each generator matrix corresponding to the length along each of the three axes. This vector provides the axis around which the qubit Bloch vector rotates, thus providing an obvious indication as to how the quantum state of the qubit will evolve in time. As the Hamiltonians for qutrits are higher dimensional and inherently more complex, an equivalent mapping of the Hamiltonian imposed onto the octant, as well as its effect on ensuing dynamics, has the potential to be a powerful tool and warrants further investigation.

# A | Vacuum Repair Methods

## A.1 Vacuum Pump Procedure

As the vacuum pumps in Ph28 of the Durham Physics Department can be irreparably damaged if turned on/off in the incorrect order, turning the equipment on or off in the correct order is of utmost importance. The sequence to do this is as follows:

1. Turn on the rotary pump pictured in figure A.1.


Figure A.1: Rotary Pump

2. After $\sim$ 30s, turn on the turbo pump and open the black valve connecting the turbo to the rig.

3. Use the pirani gauge setting on the IG controller until a pressure of $\mathcal{O}(10^{-2})$mBar is measured, after which monitor the pressure with the IG.

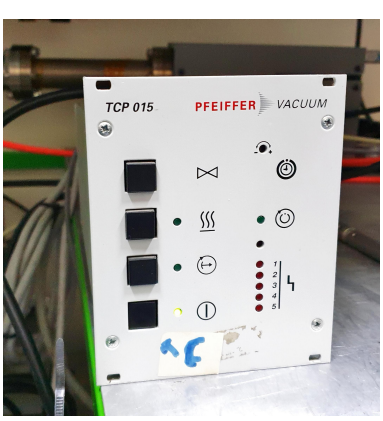


(a)

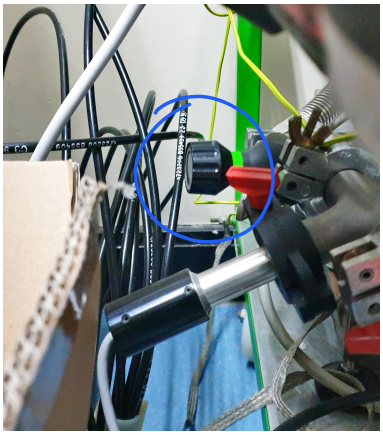

(b)

Figure A.2: Turbo pump power supply **(a)** and gate valve **(b)** circled in blue.

## A.2 Spot Welder Usage

The spot welding process involves a lot of trial and error. This comes at two points: setting the welding power and making the weld. The welding power needs to be sufficiently high that enough heat is generated for a weld to occur, but low enough that the welding process doesn't blow a hole in the dispenser tab. It is the author's recommendation that the welding power is titrated using spare parts (such as the tabs on old dispensers and spare wire). A good connection between the wire and dispensers is one that can withstand light bending both parallel and perpendicular to the dispenser tab. A successful weld can produce a bright spark. As such, safety goggles should be worn when welding. The welding process referencing figure A.3 is as follows:

1. Hold two pieces for welding with crocodile clips and pliers (yellow circle).
2. Set the power of the welder using the coarse (solid green circle) and fine (dashed green circle) adjustment knobs.
3. Turn weld switch (red circle) to on.
4. Bring pieces of metal together, expect a bright spark and trial and error.

## A.3 Residual Gas Analyser Usage

The RGA is of great utility in identifying leaks and for monitoring dispenser activation. The procedure for using the RGA via the PC in Ph28 for leak testing is as follows:

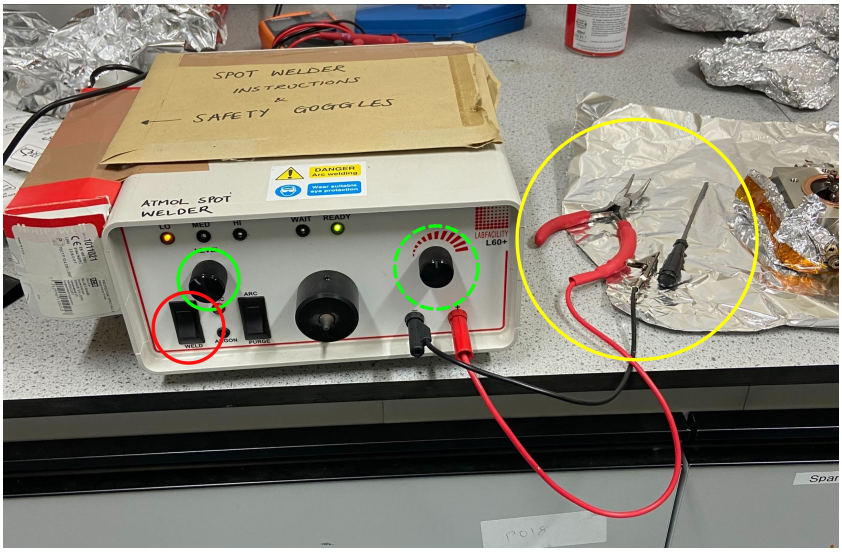


Figure A.3: Spot welder used for the welding described in section 3.3. From left to right, the circled components are the weld switch (red), coarse (solid green) and fine (dashed green) power adjustment knobs and the crocodile clips and pliers for welding (yellow).

1. Turn on RGA control box.

Figure A.4: RGA Control Box.

2. Open the RGA software on the PC.
3. Go to 'Head' dropdown menu and select head on 'Connector List Setup' pictured in figure A.5.
4. Start scan in 'Scan' dropdown menu.
5. Select 'Leak Test' mode in 'Mode' dropdown.
6. When leak testing, make sure regulator valve (red circle in figure A.6) is opened before canister valve (blue circle in figure A.6) so the tubing is flushed with He and air doesn't get back into the canister.

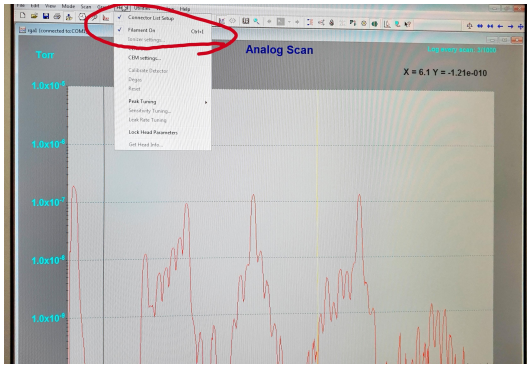


Figure A.5: Connector List Setup under Head dropdown menu.

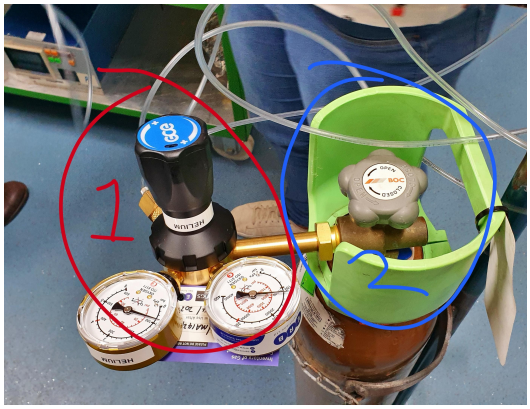


Figure A.6: Valves of the He canister with a regulator valve attached.

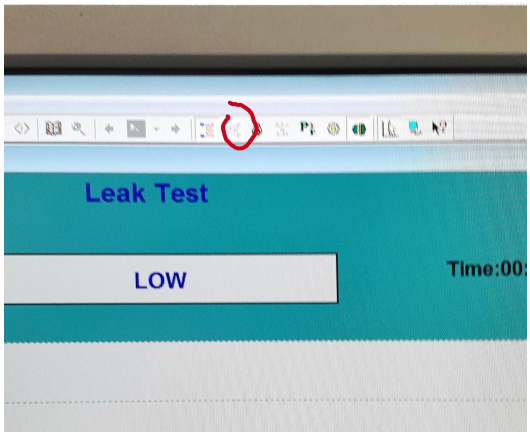


Figure A.7: Electron multiplier setting on the RGA control software, circled in red.

7. Use electron multiplier setting to increase RGA sensitivity, pictured in figure A.7.

8. Use He nozzle to fire He at the joint being tested, looking to detect a spike on the RGA's He partial pressure reading. A small spike is pictured in figure 3.15(b).

9. Repeat for, at minimum, all joins that have been replaced or newly affixed.

# B | Qutrit Visualisation Source Code

This chapter contains the source code used to generate the figures shown in chapter 4. Section B.1 gives the function library called to evolve a qutrit through time and process the qutrit density matrices for plotting on octant plots. Section B.2 gives the code used to generate figure 4.8, excluding the labelling used to explicitly show each component of the density matrix being displayed in the octant plot. The key functions of note being employed are:

- **population_and_phase** to interpret the qutrit state for plotting
- **qutrit_iter** and **obe_iter** for time evolution (not shown in this example but used to implement time evolution in figures shown in chapter 4).
- **clock_vec** for defining the phasor clock hands.

## B.1 Qutrit_Visualisation_Tools Function Library

```
"""
Created on Tue Sep 13 16:45:57 2022
Uploaded on Wed May 10 15:37 2023

@author: Max Z Festenstein
"""
import numpy as np
import scipy.linalg as spl
from scipy.special import erf as errorFunction
machine_err = np.finfo(float).eps
#%%


def full_phase(C):
    '''
    Generate a phase value phi for a complex number C = A * exp(i * phi)
    in the range of 0     phi     2  .

    Keyword Arguments
    -----------
    C : Complex number input for phase calculation. Type: complex

    Returns
    --------
    phase : Phase value phi where 0     phi     2  . Type: float

    '''

    #Normalise the complex input and define the real and imaginary parts.

    C /= np.real(np.sqrt(C*np.conj(C)))

    R = np.real(C)
    I = np.imag(C)

    #Load a default value for phase.

    phase = 0

    #Go through sign checks to determine which   /2 quadrant the phase term is
    # in and return phase value.

    if R >= 0 and I >= 0:
        phase = np.arcsin(I)

    if R < 0 and I >= 0:
        phase = np.pi - np.arcsin(I)

    if R <= 0 and I < 0:
        phase = np.pi - np.arcsin(I)

    if R > 0 and I <= 0:
        phase = 2*np.pi + np.arcsin(I)



    if R == 0 and I == 0:
        phase = 0

    return phase


```

```
63
64 def rho_gen(psi):
65     '''
66     Generate an NxN pure state density matrix for either an 1xN or Nx1 density
67     matrix.
68
69     Keyword Arguments
70     -----------
71     psi : Complex valued vector of the input wavefunction. Type: array-like.
72
73     Returns
74     -------
75     rho : Complex valued pure state density matrix. Type: numpy.ndarray.
76
77     '''
78     rho = np.outer(psi,np.conj(psi))
79     return rho
80
81
82 def erf(x, x0, sigma):
83     '''
84     Calculate the sigmoid error function for a value x, centred on point x0
85     with a standard deviation sigma.
86
87     Parameters
88     -----------
89     x : The point for which the error function is being calculated.
90         Type: float.
91
92     x0 : The centre value for the error function such that erf(x0)=0.5.
93          Type: float.
94
95     sigma : The standard deviation for the error function. Type: float.
96
97     Returns
98     -------
99     erf : The value of the error function at point x. Type: float.
100
101    '''
102    erf = ((errorFunction((x-x0)/sigma)) +1)/2
103    return erf
104
105
106 def onoff(ton,toff,times):
107    '''
108    Boolean array where ramp[time] = 1 for ton <= time <= toff and 0 everywhere
109    else.
110
111    Parameters
112    -----------
113    ton : Time at/after which values of the boolean array are set to 1.
114          Type: float.
115
116    toff : Time at/after which the values of the boolean array are set to 0.
117           Type: float.
118
119    times : Times covered by the onoff switch. Type: array-like.
120
121    Returns
122    -------
123    ramp : Boolean array with values between ton and toff set to 1.
124           Type: numpy.ndarray.
125
126    '''
127    ramp = np.zeros((times.shape[0]))
128    for ti,t in enumerate(times):
```

```
129         if t>=ton and t<= toff:
130             ramp[ti] = 1
131     return ramp
132 
133 
134 
135 
136 def rotate(origin, point, angle):
137     '''
138     Rotate a point anticlockwise by a given angle around a given origin.
139 
140     Keyword Arguments
141     -----------
142     origin : The origin around which the vector is rotated.
143              Type: 2D array-like.
144 
145     point : The coordinate of the point being rotated. Type: 2D array-like.
146 
147     angle : Anticlockwise angle in radians that the point should be rotated by.
148             Type: float.
149 
150     Returns
151     -------
152     qx : Value of the rotated x coordinate. Type: float.
153 
154     qy : Value of the rotated y coordinate. Type: float.
155 
156     '''
157     ox, oy = origin
158     px, py = point
159 
160     qx = ox + np.cos(angle) * (px - ox) - np.sin(angle) * (py - oy)
161     qy = oy + np.sin(angle) * (px - ox) + np.cos(angle) * (py - oy)
162     return qx, qy
163 
164 
165 def trace_distance(rho1,rho2):
166     '''
167     Calculate the trace distance between two density matrices.
168 
169     Keyword Arguments
170     -----------
171     rho1 : The first density matrix. Type: complex array-like.
172 
173     rho2 : The second density matrix. Type: complex array-like.
174 
175     Returns
176     -------
177     td : Trace distance between rho1 and rho2. Type: float.
178 
179     '''
180     tr = np.linalg.norm(rho1-rho2,ord = 1)
181     td = 0.5 * np.real(tr)
182     return td
183 
184 def qutrit_iter(H,psi0,t,dt,density_matrix = False,store_state = False):
185     '''
186     N dimensional pure state time iterator given a time independent Hamiltonian
187     H.
188 
189     Keyword Arguments
190     -----------
191     H : Time independent Hamiltonian under which the system evolves for time t.
192         Type: NxN complex numpy.ndarray.
193 
194     psi0 : Initial state vector or density matrix at time time=0.
```

```
195             Type: Nx1 complex numpy.ndarray -- pure state vector
196                   NxN complex numpy.ndarray -- pure state density matrix.
197
198     t : Total runtime for the time evolution. Type: float.
199
200     dt : Time increment between the finite steps of the system's
201          time evolution. Type: float.
202
203     density_matrix : Optional, boolean flag used to indicate if the quantum
204                      state is defined by a state vector or density matrix.
205                      Type: bool.
206
207                      --Accepted Arguments--
208                      False -- state vector evolution
209                      True  -- density matrix evolution.
210
211                      The default is False.
212
213     store_state : Optional, boolean flag used to indicate if a list of quantum
214                   states at each time increment should be generated.
215                          Type: bool.
216
217                          --Accepted Arguments--
218                          False -- No list generated.
219                          True  -- A list of quantum states at each timestep is
220                                   generated.
221
222                          The default is False.
223     Returns
224     -------
225     End State : State at the time time=t. Type: Nx1 or NxN complex
226                                                 numpy.ndarray.
227
228     State List: If store_state argument == True, a list of states is returned
229                 for each time increment. Type: list of complex numpy.ndarrays.
230
231     '''
232
233     steps = int(np.trunc(t/dt))         #Calculate the total number of timesteps
234                                         # to be iterated through.
235     if density_matrix == False:
236         unitary = spl.expm(-1.0j*H*dt)          #If a state vector is used,
237                                                 # generate a unitary time
238                                                 # iterator per the Heisenberg
239                                                 # picture.
240         psi = psi0
241         if store_state == False:
242             for j in range(steps):              #Iterate through the timesteps by
243                 psi = np.matmul(unitary,psi)    # performing the time iteration
244                                                 # a total of (steps) number of
245                                                 # times.
246             return psi                          #Return the end state vector.
247
248         if store_state == True:                 #Identical to the above iteration
249             psi_list = [psi0]                   # except a list of state vectors
250             for j in range(steps):              # is generated for each timestep.
251                 psi = np.matmul(unitary,psi)
252                 psi_list.append(psi)
253             return psi , psi_list               #Return vector and state list.
254
255     if density_matrix == True:
256         rho = psi0
257
258         if store_state == False:        #Iterate throught the timesteps by
259                                         # performing a decay-free Lindbladian
260                                         # time iteration for a total of (steps)
```

```
261                                     # number of times and return the
262                                     # resultant density matrix.
263
264             for j in range(steps):
265                 rho -= 1.0j*dt*(np.matmul(H,rho) - np.matmul(rho,H))
266             return rho
267
268         if store_state == True:         #Same as above, but generate a list of
269                                         # matrices at each time step, then return
270                                         # the density matrix and state list.
271             psi_list = [rho]
272             for j in range(steps):
273                 rho =  rho - 1.0j*dt*(np.matmul(H,rho) - np.matmul(rho,H))
274                 psi_list.append(rho)
275
276             return rho, psi_list
277
278 def obe_iter(H,rho0,t,dt, Collapse_Operators = None, store_state = False,
279              progress = True):
280     '''
281     N dimensional pure or mixed state density matrix time iterator given a time
282     independent Hamiltonian H.
283
284     Keyword Arguments
285     -----------
286     H : Time independent Hamiltonian under which the system evolves for time t.
287         Type: NxN complex numpy.ndarray.
288
289     rho0 : Initial density matrix at time time=0.
290            Type: NxN complex numpy.ndarray
291
292     t : Total runtime for the time evolution. Type: float.
293
294     dt : Time increment between the finite steps of the system's
295          time evolution. Type: float.
296
297     Collapse_Operators : Optional, list of collapse operators defining the
298                          decays between states in the decay matrix L of the
299                          Lindblad master equation. An example collapse operator
300                          c_op is defined below.
301                          Type: list of lists.
302
303                          ----Accepted Arguments----
304                          c_op -- [lower_state, upper_state, decay_rate]
305                                  lower_state -- n'th diagonal density matrix
306                                                 term defining the state being
307                                                 decayed into.
308                                                 Type: int.
309
310                                  upper_state -- m'th diagonal density matrix
311                                                 term defining the state being
312                                                 decayed from.
313                                                 Type: int.
314
315                                  decay_rate -- The rate at which the decay
316                                                occurs. Type: float.
317
318                          None -- Use if no decay between states is
319                                  present.
320
321
322                          The default is False.
323
324     store_state : Optional, boolean flag used to indicate if a list of quantum
325                   states at each time increment should be generated.
326                          Type: bool.
```

```
327
328                         ----Accepted Arguments----
329                         False -- No list generated.
330                         True  -- A list of quantum states at each timestep is
331                                  generated.
332
333                         The default is False.
334
335     progress: Optional, displays the progress of the simulation as a percentage
336               from completion. Type: bool.
337
338     Returns
339     -------
340     End State : State at the time time=t. Type: NxN complex numpy.ndarray.
341
342     State List: If store_state argument == True, a list of states is returned
343                 for each time increment. Type: list of complex numpy.ndarrays.
344
345
346     '''
347
348
349     steps = int(np.trunc(t/dt)) #Calculate the total number of timesteps
350                                 # to be iterated through.
351
352     rho = rho0.copy() #Explicitly create a deep copy of the initial density
353                       # matrix to prevent future errors.
354
355     if type(Collapse_Operators) != type(None):
356
357         if store_state == False:
358             for j in range(steps):    #Iterate through the time iterator loop
359                                       # a total of (steps) number of times.
360                 if progress == True:  #Print the progress of the simulation
361                     if j%100 == 0:    # every 100 iteration steps.
362                         print("\r",str(np.around(j/steps*100,1))+'%',end = '')
363
364                 L = L_gen(rho,Collapse_Operators)          #Generate the decay
365                                                            # matrix L for use
366                                                            # in the time
367                                                            # iteration, then
368                                                            # iterate throught
369                                                            # the timesteps by
370                                                            # performing a
371                                                            # Lindbladian time
372                                                            # iteration with
373                 rho += dt*(-1.0j*(H @ rho - rho @ H) + L) # decay matrix L.
374
375             return rho #Return the end result density matrix of the iteration.
376
377         if store_state == True:    #Same as above, but generate a list of
378             psi_list = [rho]       # matrices at each time step, then return
379             for j in range(steps): # the end density matrix and state list.
380                 if j%100 == 0:
381                     print("\r",str(np.around(j/steps*100,1))+'%',end = '')
382                 L = L_gen(rho,Collapse_Operators)
383                 rho =  rho + dt*(-1.0j*( H @ rho - rho @ H ) + L)
384                 psi_list.append(rho)
385
386             return rho, psi_list
387
388     if type(Collapse_Operators) == type(None):
389
390         #Same as the Collapse_Operators != None case, but without defining
391         # the decay matrix L.
392
```

```
393         if store_state == False:
394             for j in range(steps):
395                 if j%100 == 0:
396                     print("\r",str(j/steps*100)+'%',end = '')
397                 rho -= 1.0j*dt*(np.matmul(H,rho) - np.matmul(rho,H))
398             return rho
399 
400         if store_state == True:
401             psi_list = [rho]
402             for j in range(steps):
403                 if j%100 == 0:
404                     print("\r",str(j*100/steps)+'%',end = '')
405                 rho =  rho - 1.0j*dt*(np.matmul(H,rho) - np.matmul(rho,H))
406                 psi_list.append(rho)
407 
408             return rho, psi_list
409 
410 
411 def L_gen(rho,Collapse_Operators):
412     '''
413     Generate a decay matrix for use in a Lindblad master equation given a
414     density matrix rho at the current timestep.
415 
416     Keyword Arguments
417     -----------
418     rho : Density matrix at the current timestep.
419           Type: 3x3 complex numpy.ndarray
420     Collapse_Operators : List of collapse operators defining the decays between
421                          states in the decay matrix L of the Lindblad master
422                          equation. An example collapse operator c_op is defined
423                          below.
424                          Type: list of lists.
425 
426                          ----Accepted Arguments----
427                          c_op -- [lower_state, upper_state, decay_rate]
428                                  lower_state -- n'th diagonal density matrix
429                                                 term defining the state being
430                                                 decayed into.
431                                                 Type: int.
432 
433                                  upper_state -- m'th diagonal density matrix
434                                                 term defining the state being
435                                                 decayed from.
436                                                 Type: int.
437 
438                                  decay_rate -- The rate at which the decay
439                                                occurs. Type: float.
440 
441     Raises
442     ------
443     Exception
444         If the upper state is defined before the lower state.
445         Returns: 'The format for collapse operators must be
446                   c_op = [lower state, upper state, decay rate]'
447 
448     Returns
449     -------
450     L : Decay matrix for use in the Lindblad master equation.
451         Type: 3x3 complex numpy.ndarray.
452 
453     '''
454 
455     L = np.zeros((3,3),dtype = 'complex') #Initialise the decay matrix.
456 
457     for j in Collapse_Operators:
458 
```

```
459         if j[0] > j[1]:
460             raise Exception('The format for collapse operators must be c_op '+
461                             '= [lower state, upper state, decay rate]')
462 
463         Aa = np.zeros(3,dtype = 'complex') #Define two vectors to use in the
464         Ab = np.zeros(3,dtype = 'complex') # definition of the collapse
465         Aa[j[0]] = 1                       # operator
466         Ab[j[1]] = 1                       # C = |lower><upper| with decay
467         gamma = j[2]                       # strength gamma.
468         A = np.outer(Aa,Ab)                #Define the collapse operator and
469         Adag = np.transpose(A)             # it's conjugate transpose.
470 
471         #Generate the decay matrix term l according to:
472         # l = gamma*(A*rho*Adag - 0.5*{Adag*A,rho})
473         # and sum over all decay paths to generate a total L = sum(l)
474 
475         l = 2*A @ rho @ Adag
476 
477         l -= rho @ Adag @ A
478 
479         l -= Adag @ A @ rho
480 
481         l *= 0.5
482 
483         l *= gamma
484 
485         L += l
486 
487     return L
488 
489 
490 def polar_transform(vector):
491     '''
492     Transform a cartesian vector to one in circular polar coordinates.
493 
494     Keyword Arguments
495     -----------
496     vector : 3D cartesian vector. Type: 3x1 array-like.
497 
498     Returns
499     -------
500     vec : Polar vector defined in terms or r, theta and phi.
501           Type: 3x1 numpy.ndarray.
502 
503     '''
504 
505     x = vector[0]
506     y = vector[1]
507     z = vector[2]
508 
509     r = np.sqrt(x*x+y*y+z*z)
510 
511     theta = np.arccos(z/r)
512 
513     phi = np.arccos(x/(r*np.sin(theta))-machine_err)
514 
515     vec = np.array([r, theta, phi])
516 
517     return vec
518 
519 def clock_vec(vector,hand_length,phase):
520     '''
521     Generate a phasor term of for an octant plot, rotated clockwise from
522     vertical by (phase) radians around the point (vector)
523 
524     Keyword Arguments
```

```
525     ----------
526     vector : The point around which the phasor is anchored. Cartesian
527              coordinates. Type: 3x1 array-like.
528
529     hand_length : The length of the vector denoting the phasor. Type: float.
530
531     phase : Phase value of the phasor term between 0<phase<2*pi, Type: float.
532
533     Returns
534     -------
535     vec :  Cartesian phase vector stemming from the point defined by (vector)
536            rotated clockwise by (phase) radians. Type: 3x1 numpy.ndarray.
537
538     '''
539
540     #Begin by converting the input vector point to polar coordinates and define
541     # relevant lengths and angles.
542
543     polar_vector = polar_transform(vector)
544     r = polar_vector[0]
545     theta = polar_vector[1]
546     phi = polar_vector[2]
547     hl = hand_length
548
549     #Initially define the phasor's vector at point [1,0,0] as this vector is
550     # calculated as an arc swept out from the end of the point vector by a
551     # length (hand_length). As this arc will change size if swept out at
552     # different points on the octant, the end coordinate of the arc is defined
553     # as that swept out at the origin so the arc will stay the same length
554     # every time. This vector is then rotated around the origin by theta then
555     # phi to place it at the end of the input vector.
556
557     dtheta = np.pi/2 - hl*np.cos(phase) #Define the angles being swept out to
558     dphi = hl*np.sin(phase)             # generate the phasor's vector.
559
560     vec = np.array(([r*np.sin(dtheta)*np.cos(dphi), #Define the phasor vector
561                      r*np.sin(dtheta)*np.sin(dphi),  # in cartesian coordinates
562                      r*np.cos(dtheta)]))             # for rotating.
563
564     vec[0], vec[2] = rotate(origin = [0,0],           #Rotate the x and z
565                             point = [vec[0],vec[2]],  # coords around the y
566                             angle = np.pi/2 - theta)  # axis clockwise by theta
567                                                       # radians.
568
569     vec[0], vec[1] = rotate(origin = [0,0],           #Rotate the x and y
570                             point = [vec[0],vec[1]],  # coords around the z
571                             angle = phi)              # axis anticlockwise by
572                                                       # phi radians.
573     return vec                                        #Return the result.
574
575 def clock_rim(vector, hand_length):
576     '''
577     Generate coordinates for the bounding circle in which all octant phasors
578     are contained: the 'clock rim'.
579
580     Keyword Arguments
581     -----------
582     vector : The point defining the population vector for the qutrit state.
583              Type: 3x1 array-like.
584     hand_length : Radius of the bounding circle. Type: float.
585
586     Returns
587     -------
588     cvxyr : x and y coordinate data for the clock rim. Passed into a matplotlib
589             3D line as line.set_data(cvxyr[:,:]). Type: 2x50 numpy.ndarray.
590     cvzr : z coordinate data for the clock rim. Passed into a matplotlib
```

```
591             3D line as line.set_3d_properties(cvzr[:]).
592             Type: 1x50 numpy.ndarray.
593
594     '''
595
596     angles = np.linspace(0,2*np.pi,50) #Define the full 2*pi radians of the
597                                        # bounding circle.
598
599     crim = clock_vec(vector, hand_length, angles) #Generate the cartesian
600                                                   # coordinates corresponding
601                                                   # to the bounding circle
602                                                   # around the popluation
603                                                   # vector.
604
605     cvxr = crim[0][:] #Format the coordinates into xy and z arrays
606     cvyr = crim[1][:] # and return the results.
607     cvzr = crim[2][:]
608
609     cvxyr = np.array([cvxr,cvyr])
610
611     return cvxyr, cvzr
612
613 def population_and_phase(psi,density_matrix = False,force_lims = False):
614     '''
615     Interpret the state population, phase information and coherence magnitudes
616     in a state vector or density matrix for the purpose of plotting on a
617     qutrit octant plot. If a state vector is passed into this function, the
618     coherence magnitudes will == 1 always.
619
620     Keyword Arguments
621     -----------
622     psi : Qutrit state vector or density matrix to be plotted on an octant.
623           Type: 3x1 complex numpy.ndarray -- pure state vector
624                 3x3 complex numpy.ndarray -- pure state density matrix.
625     density_matrix : Optional, boolean flag used to indicate if the quantum
626                      state is defined by a state vector or density matrix.
627                      Type: bool.
628
629                      --Accepted Arguments--
630                      False -- state vector evolution
631                      True  -- density matrix evolution.
632
633                      The default is False.
634
635     force_lims : Optional, boolean flag used to indicate if the the limits of
636                  population vector need to be forced to 1 IF THE POPULATION IS
637                  OVER DUE TO FLOATING POINT ARITHMETIC ERRORS. This should be
638                  used sparingly and checked against the state vector or matrix
639                  at each usage.
640                  Type: bool.
641
642                  --Accepted Arguments--
643                  False -- The state populations are returned unchanged.
644                  True  -- The state populations are forced to a maximum of 1.
645
646                  The default is False.
647
648     Returns
649     -------
650     list containing the following:
651     [[0 state population     , 1 state population     , 2 state population    ],
652      [phi01                  , phi02                 , phi12                 ],
653      [01 coherence magnitude, 02 coherence magnitude, 12 coherence magnitude]]
654
655     '''
656
```

```
657     if density_matrix == False:  #If a state vector is used, convert to a
658         psi = rho_gen(psi)       # density matrix for ease of computation.
659
660
661     x = psi[0,0]   #Calculate the population in each state by taking the
662     y = psi[1,1]   # diagonal entry of the density matrix for each. For clarity
663     z = psi[2,2]   # the definitions |0> = x, |1> = y and |2> = z are made.
664
665     xy = psi[0,1]  #Define the off-diagonal terms for calculations of
666     yz = psi[1,2]  # phase and coherence magnitudes.
667     xz = psi[0,2]
668     xy_norm = 0
669     xz_norm = 0
670     yz_norm = 0
671     phi1 = 0
672     phi2 = 0
673     phi3 = 0
674     aphi = None #a,b,cphi are all initialised as None to allow for a type check
675     bphi = None # to see if the relevant phases need calculating.
676     cphi = None
677
678
679     #If the populations in x and y are a greater than floating-point error
680     # of 2.22e-16, calculate the phase in the range 0<phase<2*pi and the
681     # coherence magnitude of the |0><1| term accoring to the definition in
682     # https://arxiv.org/abs/2304.01741#
683
684     if x > machine_err and y > machine_err:
685         xy_norm = np.real(np.sqrt(xy*np.conj(xy)))
686         aphi = full_phase(xy)
687
688         xy_norm /= np.real(np.sqrt(x*y))
689
690     #Repeat the above process for |0><2| and |1><2| coherences.
691
692     if x > machine_err and z > machine_err:
693         xz_norm = np.real(np.sqrt(xz*np.conj(xz)))
694         bphi = full_phase(xz)
695
696
697         xz_norm /= np.real(np.sqrt(x*z))
698
699     if y > machine_err and z > machine_err:
700         yz_norm = np.real(np.sqrt(yz*np.conj(yz)))
701         cphi = full_phase(yz)
702
703
704         yz_norm /= np.real(np.sqrt(y*z))
705
706     #Perform a modular division of each phase term by 2*pi to ensure the phase
707     # values are well bounded. Use type check to see if needed.
708
709     if type(aphi) != type(None):
710         phi1 = ((aphi)%(2*np.pi))
711
712     if type(bphi) != type(None):
713         phi2 = ((bphi)%(2*np.pi))
714
715     if type(cphi) != type(None):
716         phi3 = ((cphi)%(2*np.pi))
717
718
719     #If force_lims == False, return list unchanged as specified in docstring.
720     # Coherence magnitudes are always forced due to a high likelihood of
721     # over-shooting at least once if a time iteration is plotted due to
722     # frequently being ~ 1.
```

```
723
724     if force_lims == False:
725
726         return [[np.real(x),np.real(y),np.real(z)],
727                 [np.real(phi1),np.real(phi2),np.real(phi3)],
728                 [min([1.,np.real(xy_norm)]),
729                  min([1.,np.real(xz_norm)]),
730                  min([1.,np.real(yz_norm)])]]
731
732     #If force_lims == True, return list where population values are forced to a
733     # minimum of 0 and a maximum of 1 in order to eliminate floating point
734     # arithmetic errors. Use sparingly!
735
736     if force_lims == True:
737
738         return [[max([min([1.0,np.real(x)]),0]),
739                  max([min([1.0,np.real(y)]),0]),
740                  max([min([1.0,np.real(z)]), 0 ])],
741                 [np.real(phi1),np.real(phi2),np.real(phi3)],
742                 [min([1.,np.real(xy_norm)]),
743                  min([1.,np.real(xz_norm)]),
744                  min([1.,np.real(yz_norm)])]]
```

## B.2 Example Plot

```
"""
Created on Wed Jan 25 17:28:00 2023
Uploaded on Wed May 10 15:37 2023

@author: Max Z. Festenstein
"""
import os
script_directory = os.getcwd()

import matplotlib.pyplot as plt
os.chdir('/home/wpmw81/Desktop/RQO')
plt.style.use('MZF_Thesis.mplstyle')

os.chdir('/home/wpmw81/Desktop/RQO/Qutrits')
import numpy as np
import Qutrit_Visualisation_Tools as qvt

#Define 2*pi radians for convenience and an array of angles encompassing a full
# 2*pi radians.

radians = 2*np.pi
angles = np.linspace(0,2*np.pi,50)

#Define lists for state populations. For clarity, X = |0>, Y = |1> and Z = |2>.
#Lists are defined rather than single vector componenets to conform with
# sequences where these lists store all x,y and z coordinates for the duration
# of a time iteration process.

Xs = []
Ys = []
Zs = []
vectors = []

#Initialise the state as a real, equal superposition vector.

psi =  np.array([[1],
                 [1],
                 [1]],dtype='complex') * 1/np.sqrt(3)

#'Find' the population magnitudes, phases and coherence magnitudes for this
# state vector. Note that as this is an example plot, the phases and magnitudes
# ARE HARD-CODED AFTER-THE-FACT and the 'phase' and 'mags' results are
# discarded from plotting. In a normal time evolution sequence, this would
# be the point where those elements are generated.

vector,phase,mags = qvt.population_and_phase(psi,density_matrix = False)
vectors.append(np.sqrt(vector))
Xs.append(np.sqrt(vector[0]))   #Populations are square rooted such that the
Ys.append(np.sqrt(vector[1]))   # state vector lies on the surface of the
Zs.append(np.sqrt(vector[2]))   # octant.

#Define the plots used for the octant. The plt subfigure environment is used
# as controlling aspect ratios and axes are more straightforward than in the
# mpl_toolkits.mplot3d.Axes3D environment.
fig = plt.figure()
ax1 = fig.add_subplot(111,projection='3d')
ax1.set_box_aspect([1,1,1])

#Set the camera angles.
ax1.azim = 12
ax1.elev = 25

```

```
63
64 #Seperately define the phases to be plotted
65 phis1 = [np.pi/2]
66 phis2 = [np.pi*3/4]
67 phis3 = [np.pi*1/4]
68
69 #Generate the cartesian vectors used for the phasors using the previously
70 # defined phases and state vector.
71 cvec1 = qvt.clock_vec(vectors[0],0.2,phis1[0])
72 cvec2 = qvt.clock_vec(vectors[0],0.2,phis2[0])
73 cvec3 = qvt.clock_vec(vectors[0],0.2,phis3[0])
74
75 #Define the state vector as solid green for labelling in the legend.
76 lnvec = ax1.plot(Xs[0], Ys[0], Zs[0], 'g-',lw=2,label='State Vector')[0]
77
78
79 #Plot the previously defined clock vectors.
80 clock1 = ax1.plot([Xs[0],cvec1[0]],[Ys[0],cvec1[1]],[Zs[0],cvec1[2]],
81                   'red',label = r'$\phi_{1}$',linewidth = 1.5)[0]
82 clock2 = ax1.plot([Xs[0],cvec2[0]],[Ys[0],cvec2[1]],[Zs[0],cvec2[2]],
83                   'blue',label = r'$\phi_{2}$',linewidth = 1.25)[0]
84 clock3 = ax1.plot([Xs[0],cvec3[0]],[Ys[0],cvec3[1]],[Zs[0],cvec3[2]],
85                   '#A300A3',label = r'$\phi_{12}$',linewidth = 1)[0]
86
87
88 # Commented out below are the labels used for the coherence magnitudes R_jk.
89 # ==========================================================================
90 # rsize = 11
91 #
92 # ax1.text(cvec1[0]+0.2,cvec1[1]+0.05,cvec1[2]+0.06,r'$\mathrm{R}_{01}$',color='
       red', size = rsize)
93 # ax1.text(cvec2[0],cvec2[1]-0.05,cvec2[2],r'$\mathrm{R}_{02}$',color='blue', size
       = rsize)
94 # ax1.text(cvec3[0]-0.1,cvec3[1]+0.01,cvec3[2],r'$\mathrm{R}_{12}$',color='#A300A3
       ', size = rsize)
95 #
96 # ==========================================================================
97
98 #Create ket labels for the three axes and remove the axis lines themselves.
99 #NB: The axes are later re-defined explicitly in the range from 0 --> 1.
100 #Also remove background colours and remove background grids. Aesthetic only.
101 labelsize = 12
102 ax1.text(1.18,-0.05,0,r'$|0 \rangle$', size = labelsize)
103 ax1.text(0.05,1.02,0,r'$|1 \rangle$', size = labelsize)
104 ax1.text(0,-0.05,1.05,r'$|2 \rangle$', size = labelsize)
105 ax1.tick_params(left = False, right = False , labelleft = False,labelbottom =
       False, bottom = False)
106 ax1.axis('off')
107
108 ax1.xaxis.set_pane_color((1.0, 1.0, 1.0, 0.0))
109 ax1.yaxis.set_pane_color((1.0, 1.0, 1.0, 0.0))
110 ax1.zaxis.set_pane_color((1.0, 1.0, 1.0, 0.0))
111
112
113 # make the grid lines transparent
114 ax1.xaxis._axinfo["grid"]['color'] =  (1,1,1,0)
115 ax1.yaxis._axinfo["grid"]['color'] =  (1,1,1,0)
116 ax1.zaxis._axinfo["grid"]['color'] =  (1,1,1,0)
117
118
119 #Plot the dashed grey lines to guide the eye to the surface of the octant.
120
121 v = np.linspace(0,np.pi/2,101)
122 u= np.linspace(0,np.pi/2,5)
123 for j in u:
124     x = np.cos(j)*np.sin(v)
```

```
125     y = np.sin(j)*np.sin(v)
126     z = np.cos(v)
127     ax1.plot3D(x, y, z, color="grey",ls='—',lw = 0.5)
128
129 for j in u:
130     x = np.cos(v)*np.sin(j)
131     y = np.sin(v)*np.sin(j)
132     z = np.cos(j)
133     ax1.plot3D(x, y, z, color="grey",ls='—',lw = 0.5)
134
135
136 #Now draw the axes restricted from 0 —> 1.
137 xline=((0,1),(0,0),(0,0))
138 ax1.plot(xline[0],xline[1],xline[2],'black',linewidth=0.5)
139 yline=((0,0),(0,1),(0,0))
140 ax1.plot(yline[0],yline[1],yline[2],'black',linewidth=0.5)
141 zline=((0,0),(0,0),(0,1))
142 ax1.plot(zline[0],zline[1],zline[2],'black',linewidth=0.5)
143
144 #Define and plot the state vector from the origin to the point derived from the
145 # calculation from the population_and_phase function.
146 xv = [0,Xs[0]]
147 yv = [0,Ys[0]]
148 zv = [0,Zs[0]]
149 ax1.plot(xv,yv,zv,'g',linewidth=2,alpha=1)
150
151 # Commented out below are the labels used to show population magnitudes.
152 # ==========================================================================
153 # #========================= Axis highlights to show states clearly==========
154 #
155 # # Z axis highlight
156 #
157 # ax1.plot([0,0],[0,0],[0,Zs[0]],'g',ls = '--', linewidth = 1.2,alpha = 1)
158 #
159 # textsize = 14
160 #
161 # ax1.text(0.2,-0.05,Zs[0]/2,r'$\gamma$',color='g', size = textsize)
162 #
163 #
164 # #Y axis highlight
165 #
166 # ax1.plot([0,0],[0,Ys[0]],[0,0],'g',ls = '--', linewidth = 1.2,alpha = 1)
167 #
168 # ax1.text(-0.01,Ys[0]/2,0.05,r'$\beta$',color='g', size = textsize)
169 #
170 # # X axis highlight
171 #
172 # ax1.plot([0,Xs[0]],[0,0],[0,0],'g',ls = '--', linewidth = 1.2,alpha = 1)
173 #
174 # ax1.text(Xs[0]/2+0.1,-0.07,0.05,r'$\alpha$',color='g', size = textsize)
175 #
176 # ==========================================================================
177
178
179 # Commented out below are calculations of the phase arcs used to illustrate the
180 # rotation of the phasors from the phase = 0 point.
181 # ==========================================================================
182 # arc1 = np.linspace(0,phis1[0],50)
183 # arc2 = np.linspace(0,phis2[0],50)
184 # arc3 = np.linspace(0,phis3[0],100)
185 #
186 # arc1 = qvt.clock_vec(vectors[0],0.21,arc1)
187 # arc2 = qvt.clock_vec(vectors[0],0.23,arc2)
188 # arc3 = qvt.clock_vec(vectors[0],0.25,arc3)
189 #
190 # ==========================================================================
```

```
191
192 #The bounding circle for the phasors is defined and plotted.
193 crim = qvt.clock_vec(vectors[0],0.2,angles)
194 ax1.plot(crim[0],crim[1],crim[2],'grey',ls = '-',linewidth = 0.6, alpha = 0.5)
195 #The phase=0 line is defined.
196 cveczero = qvt.clock_vec(vectors[0],.2,0)
197
198
199 #The x,y and z components of the phase=0 line out from the population vector
200 # are defined and plotted.
201 cvx1 = [Xs[0],cveczero[0]]
202 cvy1 = [Ys[0],cveczero[1]]
203 cvz1 = [Zs[0],cveczero[2]]
204 ax1.plot(cvx1,cvy1,cvz1,'k',ls= '-',linewidth = 1.0, alpha = 1,label = r'$\phi = 0
      $')
205
206 #In order to reduce the magnitudes of the phi1 and phi 2 components, new clock
207 # vectors with reduced hand sizes (0.75 and 0.5 respectively) are calculated
208 # and the lines for each are adjusted accordingly.
209 cvec1 = qvt.clock_vec(vectors[0],0.75*0.2,phis1[0])
210 cvec2 = qvt.clock_vec(vectors[0],0.5*0.2,phis2[0])
211
212 cvx1 = [Xs[0],cvec1[0]]
213 cvy1 = [Ys[0],cvec1[1]]
214 cvz1 = [Zs[0],cvec1[2]]
215
216 cvxy1 = np.array([cvx1,cvy1])
217 clock1.set_data(cvxy1[:,:])
218 clock1.set_3d_properties(cvz1[:])
219
220 cvx2 = [Xs[0],cvec2[0]]
221 cvy2 = [Ys[0],cvec2[1]]
222 cvz2 = [Zs[0],cvec2[2]]
223
224 cvxy2 = np.array([cvx2,cvy2])
225 clock2.set_data(cvxy2[:,:])
226 clock2.set_3d_properties(cvz2[:])
227
228 # Commented out below are plots for the phase arcs used to illustrate the
229 # rotation of the phasors from the phase = 0 point.
230 # ================================================================
231 # ax1.plot(arc1[0],arc1[1],arc1[2],'red',ls = '--',linewidth = 0.7, alpha = 0.8)
232 # ax1.plot(arc2[0],arc2[1],arc2[2],'blue',ls = '--',linewidth = 0.7, alpha = 0.8)
233 # ax1.plot(arc3[0],arc3[1],arc3[2],'#A300A3',ls = '--',linewidth = 0.7, alpha =
      0.8)
234 # ================================================================
235
236
237
238 # Commented out below are the in-plot guiding lines for the population vector's
239 # x,y and z components.
240 # ================================================================
241 # #=======Plot some guide lines to show relative positions on each axis=========
242 # # Start with Z axis
243 #
244 #
245 # ax1.plot([0,Xs[0]],[0,Ys[0]],[Zs[0],Zs[0]],'k',ls = '--', linewidth = 0.5,alpha
      = 0.9)
246 #
247 #
248 # # Plot X and Y guide stem
249 #
250 # ax1.plot([Xs[0],Xs[0]],[Ys[0],Ys[0]],[0,Zs[0]],'k',ls = '--', linewidth = 0.5,
      alpha = 0.9)
251 #
252 # #Plot X guide
```

```
253 #
254 # ax1.plot([Xs[0],Xs[0]],[0,Ys[0]],[0,0],'k',ls = '--', linewidth = 0.5,alpha =
        0.9)
255 #
256 # #Plot Y guide
257 #
258 # ax1.plot([0,Xs[0]],[Ys[0],Ys[0]],[0,0],'k',ls = '--', linewidth = 0.5,alpha =
        0.9)
259 #
260 #
261 #
262 # ================================================================================
263 ax1.legend(loc= 1, prop={'size':10})
264
265 plt.show()
```

# Bibliography


[1] William Hyde Wollaston. XII. A method of examining refractive and dispersive powers, by prismatic reflection. *Philosophical Transactions of the Royal Society of London*, 92:365–380, 12 1802. ISSN 0261-0523. doi: 10.1098/rstl.1802.0014. URL https://royalsocietypublishing.org/doi/10.1098/rstl.1802.0014.

[2] C.J Foot. *Atomic Physics*. Oxford University Press, Oxford, 1st edition, 2005. ISBN 0-19-850695-3.

[3] J. J. Balmer. Note on the Spectral Lines of Hydrogen. *Annalen der Physik und Chemie*, 3(25):80–87, 1885.

[4] J. N. Lockyer. VIII. Notice of an observation of the spectrum of a solar prominence, by J. N. Lockyer, Esq., in a letter to the secretary. Communicated by Dr. Sharpey. *Proceedings of the Royal Society of London*, 17:91–92, 12 1869. ISSN 0370-1662. doi: 10.1098/rspl.1868.0011.

[5] J. R. Rydberg. XXXIV. On the structure of the line-spectra of the chemical elements. *The London, Edinburgh, and Dublin Philosophical Magazine and Journal of Science*, 29(179):331–337, 4 1890. ISSN 1941-5982. doi: 10.1080/14786449008619945.

[6] N. Bohr. I. On the constitution of atoms and molecules. *The London, Edinburgh, and Dublin Philosophical Magazine and Journal of Science*, 26(151): 1–25, 7 1913. ISSN 1941-5982. doi: 10.1080/14786441308634955.

[7] A. Einstein. On a Heuristic Point of View Concerning the Production and Transformation of Light. *Annalen der Physik*, 17:132–148, 1905.

[8] P Dirac. The fundamental equations of quantum mechanics. *Proceedings of the Royal Society of London. Series A, Containing Papers of a Mathematical and Physical Character*, 109(752):642–653, 12 1925. ISSN 0950-1207. doi: 10.1098/rspa.1925.0150.

[9] W. Heisenberg. Uber quantentheoretische Umdeutung kinematischer und mechanischer Beziehungen. *Zeitschrift fur Physik*, 33(1):879–893, 12 1925. ISSN 1434-6001. doi: 10.1007/BF01328377.

[10] Alfred Kastler. Optical Methods for Studying Hertzian Resonances. *Science*, 158(3798):214–221, 10 1967. ISSN 0036-8075. doi: 10.1126/science.158.3798.214. URL https://www.science.org/doi/10.1126/science.158.3798.214.

[11] A. L. Schawlow and C. H. Townes. Infrared and Optical Masers. *Physical Review*, 112(6):1940–1949, 12 1958. ISSN 0031-899X. doi: 10.1103/PhysRev.112.1940. URL https://link.aps.org/doi/10.1103/PhysRev.112.1940.

[12] C. K. N. Patel and R. J. Kerl. LASER OSCILLATION ON X1 Σ+ VIBRATIONAL-ROTATIONAL TRANSITIONS OF CO. *Applied Physics Letters*, 5(4):81–83, 8 1964. ISSN 0003-6951. doi: 10.1063/1.1754065. URL https://pubs.aip.org/aip/apl/article/5/4/81-83/51542.

[13] E Archbold, D W Harper, and T P Hughes. Time-resolved spectroscopy of laser-generated microplasmas. *British Journal of Applied Physics*, 15 (11):1321–1326, 11 1964. ISSN 0508-3443. doi: 10.1088/0508-3443/15/11/309. URL https://iopscience.iop.org/article/10.1088/0508-3443/15/11/309.

[14] C. Wieman and T. W. Hänsch. Doppler-Free Laser Polarization Spectroscopy. *Physical Review Letters*, 36(20):1170–1173, 5 1976. ISSN 0031-9007. doi: 10.1103/PhysRevLett.36.1170. URL https://link.aps.org/doi/10.1103/PhysRevLett.36.1170.

[15] S.L. Kaufman. High-resolution laser spectroscopy in fast beams. *Optics Communications*, 17(3):309–312, 6 1976. ISSN 00304018. doi: 10.1016/0030-4018(76)90267-4. URL https://linkinghub.elsevier.com/retrieve/pii/0030401876902674.

[16] W. Nagourney, G. Janik, and H. Dehmelt. Linewidth of single laser-cooled 24Mg + ion in radiofrequency trap. *Proceedings of the National Academy of Sciences*, 80(2):643–646, 1 1983. ISSN 0027-8424. doi: 10.1073/pnas.80.2.643. URL https://pnas.org/doi/full/10.1073/pnas.80.2.643.

[17] E. L. Raab, M. Prentiss, Alex Cable, Steven Chu, and D. E. Pritchard. Trapping of Neutral Sodium Atoms with Radiation Pressure. *Physical Review Letters*, 59(23):2631–2634, 12 1987. ISSN 0031-9007. doi: 10.1103/PhysRevLett.59.2631.

[18] William D Phillips and Harold J Metcalf. Cooling and Trapping Atoms. *Scientific American*, 256(3):50–57, 1987. URL http://www.jstor.org/stable/24979340.

[19] William D. Phillips. Nobel Lecture: Laser cooling and trapping of neutral atoms. *Reviews of Modern Physics*, 70(3):721–741, 7 1998. ISSN 0034-6861. doi: 10.1103/RevModPhys.70.721. URL https://link.aps.org/doi/10.1103/RevModPhys.70.721.

[20] M. H. Anderson, J. R. Ensher, M. R. Matthews, C. E. Wieman, and E. A. Cornell. Observation of Bose-Einstein Condensation in a Dilute Atomic Vapor. *Science*, 269(5221):198–201, 7 1995. ISSN 0036-8075. doi: 10.1126/science.269.5221.198. URL https://www.science.org/doi/10.1126/science.269.5221.198.

[21] Richard P. Feynman. Simulating physics with computers. *International Journal of Theoretical Physics*, 21(6-7):467–488, 6 1982. ISSN 0020-7748. doi: 10.1007/BF02650179.

[22] David P. DiVincenzo. The physical implementation of quantum computation, 2000. ISSN 00158208.

[23] Sergei Slussarenko and Geoff J. Pryde. Photonic quantum information processing: A concise review. *Applied Physics Reviews*, 6(4):041303, 12 2019. ISSN 1931-9401. doi: 10.1063/1.5115814. URL https://pubs.aip.org/aip/apr/article/997349.

[24] Igor P Ivanov, Valeriy G Serbo, and Pengming Zhang. Fate of the Landau–Yang theorem for twisted photons. *Journal of Optics*, 21(11):114001, 11 2019. ISSN 2040-8978. doi: 10.1088/2040-8986/ab491a.

[25] Michael Fleischhauer, Atac Imamoglu, and Jonathan P Marangos. Electromagnetically induced transparency: Optics in coherent media. *Reviews of Modern Physics*, 77(2):633–673, 2005. doi: https://doi.org/10.1103/RevModPhys.77.633.

[26] A. K. Mohapatra, T. R. Jackson, and C. S. Adams. Coherent Optical Detection of Highly Excited Rydberg States Using Electromagnetically Induced Transparency. *Physical Review Letters*, 98(11):113003, 3 2007. ISSN 0031-9007. doi: 10.1103/PhysRevLett.98.113003. URL https://link.aps.org/doi/10.1103/PhysRevLett.98.113003.

[27] Lijun Ma, Oliver Slattery, Paulina Kuo, and Xiao Tang. EIT quantum memory with Cs atomic vapor for quantum communication. In Ronald E.

Meyers, Yanhua Shih, and Keith S. Deacon, editors, *Quantum Communications and Quantum Imaging XIII*, volume 9615, page 96150D. SPIE, 9 2015. ISBN 9781628417814. doi: 10.1117/12.2186639. URL http://proceedings.spiedigitallibrary.org/proceeding.aspx?doi=10.1117/12.2186639.

[28] Lijun Ma, Oliver Slattery, and Xiao Tang. Optical quantum memory based on electromagnetically induced transparency. *Journal of Optics*, 19(4):043001, 4 2017. ISSN 2040-8978. doi: 10.1088/2040-8986/19/4/043001. URL https://iopscience.iop.org/article/10.1088/2040-8986/19/4/043001.

[29] Xing Lei, Lixia Ma, Jieli Yan, Xiaoyu Zhou, Zhihui Yan, and Xiaojun Jia. Electromagnetically induced transparency quantum memory for non-classical states of light. *Advances in Physics: X*, 7(1), 12 2022. ISSN 2374-6149. doi: 10.1080/23746149.2022.2060133. URL https://www.tandfonline.com/doi/full/10.1080/23746149.2022.2060133.

[30] Inbal Friedler, David Petrosyan, Michael Fleischhauer, and Gershon Kurizki. Long-range interactions and entanglement of slow single-photon pulses. *Physical Review A*, 72(4):043803, 10 2005. ISSN 1050-2947. doi: 10.1103/PhysRevA.72.043803. URL https://link.aps.org/doi/10.1103/PhysRevA.72.043803.

[31] Alexey V. Gorshkov, Johannes Otterbach, Michael Fleischhauer, Thomas Pohl, and Mikhail D. Lukin. Photon-Photon Interactions via Rydberg Blockade. *Physical Review Letters*, 107(13):133602, 9 2011. ISSN 0031-9007. doi: 10.1103/PhysRevLett.107.133602. URL https://link.aps.org/doi/10.1103/PhysRevLett.107.133602.

[32] D. Paredes-Barato and C. S. Adams. All-Optical Quantum Information Processing Using Rydberg Gates. *Physical Review Letters*, 112(4):040501, 1 2014. ISSN 0031-9007. doi: 10.1103/PhysRevLett.112.040501. URL https://link.aps.org/doi/10.1103/PhysRevLett.112.040501.

[33] Mohammadsadegh Khazali, Khabat Heshami, and Christoph Simon. Photon-photon gate via the interaction between two collective Rydberg excitations. *Physical Review A*, 91(3):030301, 3 2015. ISSN 1050-2947. doi: 10.1103/PhysRevA.91.030301. URL https://link.aps.org/doi/10.1103/PhysRevA.91.030301.

[34] I. Mourachko, D. Comparat, F. de Tomasi, A. Fioretti, P. Nosbaum, V. M. Akulin, and P. Pillet. Many-Body Effects in a Frozen Rydberg Gas. *Physical Review Letters*, 80(2):253–256, 1 1998. ISSN 0031-9007. doi:

10.1103/PhysRevLett.80.253. URL https://link.aps.org/doi/10.1103/PhysRevLett.80.253.

[35] D. Maxwell, D. J. Szwer, D. Paredes-Barato, H. Busche, J. D. Pritchard, A. Gauguet, M. P. A. Jones, and C. S. Adams. Microwave control of the interaction between two optical photons. *Physical Review A*, 89(4):043827, 4 2014. ISSN 1050-2947. doi: 10.1103/PhysRevA.89.043827. URL https://link.aps.org/doi/10.1103/PhysRevA.89.043827.

[36] D. Barredo, S. Ravets, H. Labuhn, L. Béguin, A. Vernier, F. Nogrette, T. Lahaye, and A. Browaeys. Demonstration of a Strong Rydberg Blockade in Three-Atom Systems with Anisotropic Interactions. *Physical Review Letters*, 112(18):183002, 5 2014. ISSN 0031-9007. doi: 10.1103/PhysRevLett.112.183002. URL https://link.aps.org/doi/10.1103/PhysRevLett.112.183002.

[37] Christophe Boisseau, Ionel Simbotin, and Robin Côté. Macrodimers: Ultralong Range Rydberg Molecules. *Physical Review Letters*, 88(13):133004, 3 2002. ISSN 0031-9007. doi: 10.1103/PhysRevLett.88.133004. URL https://link.aps.org/doi/10.1103/PhysRevLett.88.133004.

[38] Kilian Singer, Markus Reetz-Lamour, Thomas Amthor, Simon Fölling, Michaela Tscherneck, and Matthias Weidemüller. Spectroscopy of an ultracold Rydberg gas and signatures of Rydberg–Rydberg interactions. *Journal of Physics B: Atomic, Molecular and Optical Physics*, 38(2):S321–S332, 1 2005. ISSN 0953-4075. doi: 10.1088/0953-4075/38/2/023. URL https://iopscience.iop.org/article/10.1088/0953-4075/38/2/023.

[39] Thad G. Walker and M. Saffman. Consequences of Zeeman degeneracy for the van der Waals blockade between Rydberg atoms. *Physical Review A*, 77(3):032723, 3 2008. ISSN 1050-2947. doi: 10.1103/PhysRevA.77.032723. URL https://link.aps.org/doi/10.1103/PhysRevA.77.032723.

[40] E. Urban, T. A. Johnson, T. Henage, L. Isenhower, D. D. Yavuz, T. G. Walker, and M. Saffman. Observation of Rydberg blockade between two atoms. *Nature Physics*, 5(2):110–114, 2 2009. ISSN 1745-2473. doi: 10.1038/nphys1178. URL http://www.nature.com/articles/nphys1178.

[41] Alpha Gaëtan, Yevhen Miroshnychenko, Tatjana Wilk, Amodsen Chotia, Matthieu Viteau, Daniel Comparat, Pierre Pillet, Antoine Browaeys, and Philippe Grangier. Observation of collective excitation of two individual atoms in the Rydberg blockade regime. *Nature Physics*, 5(2):115–118, 2

2009. ISSN 1745-2473. doi: 10.1038/nphys1183. URL http://www.nature.com/articles/nphys1183.

[42] J. M. Raimond, M. Brune, and S. Haroche. Manipulating quantum entanglement with atoms and photons in a cavity. *Reviews of Modern Physics*, 73(3): 565–582, 8 2001. ISSN 0034-6861. doi: 10.1103/RevModPhys.73.565. URL https://link.aps.org/doi/10.1103/RevModPhys.73.565.

[43] M. Gross and S. Haroche. Superradiance: An essay on the theory of collective spontaneous emission. *Physics Reports*, 93(5):301–396, 12 1982. ISSN 03701573. doi: 10.1016/0370-1573(82)90102-8. URL https://linkinghub.elsevier.com/retrieve/pii/0370157382901028.

[44] Nicholas L.R. Spong, Yuechun Jiao, Oliver D.W. Hughes, Kevin J. Weatherill, Igor Lesanovsky, and Charles S. Adams. Collectively Encoded Rydberg Qubit. *Physical Review Letters*, 127(6), 8 2021. ISSN 10797114. doi: 10.1103/PhysRevLett.127.063604.

[45] M. Saffman, T. G. Walker, and K. Mølmer. Quantum information with Rydberg atoms. *Reviews of Modern Physics*, 82(3):2313–2363, 8 2010. ISSN 0034-6861. doi: 10.1103/RevModPhys.82.2313. URL https://link.aps.org/doi/10.1103/RevModPhys.82.2313.

[46] Antoine Browaeys and Thierry Lahaye. Many-body physics with individually controlled Rydberg atoms. *Nature Physics*, 16(2):132–142, 2 2020. ISSN 1745-2473. doi: 10.1038/s41567-019-0733-z. URL http://www.nature.com/articles/s41567-019-0733-z.

[47] Sepehr Ebadi, Tout T. Wang, Harry Levine, Alexander Keesling, Giulia Semeghini, Ahmed Omran, Dolev Bluvstein, Rhine Samajdar, Hannes Pichler, Wen Wei Ho, Soonwon Choi, Subir Sachdev, Markus Greiner, Vladan Vuletić, and Mikhail D. Lukin. Quantum phases of matter on a 256-atom programmable quantum simulator. *Nature*, 595(7866):227–232, 7 2021. ISSN 0028-0836. doi: 10.1038/s41586-021-03582-4. URL https://www.nature.com/articles/s41586-021-03582-4.

[48] Eduard A. Manykin. Nonlinear optical processes in Rydberg atoms systems. In Anatoly V. Andreev, Pavel A. Apanasevich, Vladimir I. Emel'yanov, and Alexander P. Nizovtsev, editors, *ICONO 2001: Fundamental Aspects of Laser-Matter Interaction and Physics of Nanostructures*, volume 4748, page 13. SPIE, 5 2002. doi: 10.1117/12.468941. URL http://proceedings.spiedigitallibrary.org/proceeding.aspx?doi=10.1117/12.468941.

[49] Serge Haroche. Nobel Lecture: Controlling photons in a box and exploring the quantum to classical boundary. *Reviews of Modern Physics*, 85(3):1083–1102, 7 2013. ISSN 0034-6861. doi: 10.1103/RevModPhys.85.1083. URL https://link.aps.org/doi/10.1103/RevModPhys.85.1083.

[50] Georg Raithel, Andira Ramos, Kaitlin Moore, and Vladimir Malinovsky. Measurement of the Rydberg Constant with Trapped Rydberg Atoms. In *2018 Conference on Precision Electromagnetic Measurements (CPEM 2018)*, pages 1–2. IEEE, 7 2018. ISBN 978-1-5386-0974-3. doi: 10.1109/CPEM.2018.8501136. URL https://ieeexplore.ieee.org/document/8501136/.

[51] Bo Yang, Bo Zhang, Zilong Liu, and Hengyu Yao. Interactions of cold Rydberg atoms and metallic surfaces. *Journal of Physics B: Atomic, Molecular and Optical Physics*, 52(9):095501, 5 2019. ISSN 0953-4075. doi: 10.1088/1361-6455/ab066b. URL https://iopscience.iop.org/article/10.1088/1361-6455/ab066b.

[52] Chengshu Li and Fan Yang. Lee-Yang zeros in the Rydberg atoms. *Frontiers of Physics*, 18(2):22301, 4 2023. ISSN 2095-0462. doi: 10.1007/s11467-022-1226-6. URL https://link.springer.com/10.1007/s11467-022-1226-6.

[53] Yafen Cai, Shuai Shi, Yijia Zhou, Jianhao Yu, Yali Tian, Yitong Li, Kuan Zhang, Chenhao Du, Weibin Li, and Lin Li. A multi-band atomic candle with microwave-dressed Rydberg atoms. *Frontiers of Physics*, 18(1):12302, 2 2023. ISSN 2095-0462. doi: 10.1007/s11467-022-1218-6. URL https://link.springer.com/10.1007/s11467-022-1218-6.

[54] Kevin J Weatherill. *A C02 Laser Lattice Experiment for Cold Atoms*. PhD thesis, Durham University, Durham, 2007.

[55] D. Maxwell, D. J. Szwer, D. Paredes-Barato, H. Busche, J. D. Pritchard, A. Gauguet, K. J. Weatherill, M. P. A. Jones, and C. S. Adams. Storage and Control of Optical Photons Using Rydberg Polaritons. *Physical Review Letters*, 110(10):103001, 3 2013. ISSN 0031-9007. doi: 10.1103/PhysRevLett.110.103001. URL https://link.aps.org/doi/10.1103/PhysRevLett.110.103001.

[56] Hannes Busche. *Contactless quantum non-linear optics with cold Rydberg atoms*. PhD thesis, 2017.

[57] Simon Ball. *A Coherent Microwave Interface For Manipulation of Single Optical Photons*. PhD thesis, Durham University, Durham, 11 2017.

[58] Nicholas Leonard Robert Spong. *Coherent Manipulation of Rydberg Polaritons*. PhD thesis, 2021.

[59] Thomas Durt, Nicolas J. Cerf, Nicolas Gisin, and Marek Żukowski. Security of quantum key distribution with entangled qutrits. *Physical Review A*, 67 (1):6, 2003. ISSN 10941622. doi: 10.1103/PhysRevA.67.012311.

[60] You-Bang Zhan, Ling-Ling Zhang, and Qun-Yong Zhang. Quantum secure direct communication by entangled qutrits and entanglement swapping. *Optics Communications*, 282(23):4633–4636, 12 2009. ISSN 00304018. doi: 10.1016/j.optcom.2009.08.024. URL https://linkinghub.elsevier.com/retrieve/pii/S0030401809007883.

[61] Yevhen Vasiliu, Igor Limar, Tomasz Gancarczyk, and Mikolaj Karpinski. New Quantum Secret Sharing Protocol Using Entangled Qutrits. In *2019 10th IEEE International Conference on Intelligent Data Acquisition and Advanced Computing Systems: Technology and Applications (IDAACS)*, pages 324–329. IEEE, 9 2019. ISBN 978-1-7281-4069-8. doi: 10.1109/IDAACS.2019.8924256. URL https://ieeexplore.ieee.org/document/8924256/.

[62] L-m Duan, M D Lukin, J I Cirac, and P Zoller. Long-distance quantum communication with atomic ensembles and linear optics. *Nature*, 414, 2001. URL www.nature.com.

[63] Valerii Tkachuk. Quantum Genetic Algorithm Based on Qutrits and Its Application. *Mathematical Problems in Engineering*, 2018, 2018. ISSN 15635147. doi: 10.1155/2018/8614073.

[64] Liang Qiu, An Min Wang, and Xiao San Ma. Optimal dense coding with thermal entangled states. *Physica A: Statistical Mechanics and its Applications*, 383(2):325–330, 9 2007. ISSN 03784371. doi: 10.1016/j.physa.2007.05.021. URL https://linkinghub.elsevier.com/retrieve/pii/S037843710700516X.

[65] Sovik Roy and Biplab Ghosh. Study of controlled dense coding with some discrete tripartite and quadripartite states. *International Journal of Quantum Information*, 13(05):1550033, 8 2015. ISSN 0219-7499. doi: 10.1142/S0219749915500331.

[66] Liang Qiu, Zhi Liu, and Fei Pan. Entanglement Purification of Noisy Two-Qutrit States Via Environment Measurement. *International Journal of Theoretical Physics*, 57(2):301–310, 2 2018. ISSN 0020-7748. doi:

10.1007/s10773-017-3562-9. URL http://link.springer.com/10.1007/s10773-017-3562-9.

[67] Yi-Han Luo, Han-Sen Zhong, Manuel Erhard, Xi-Lin Wang, Li-Chao Peng, Mario Krenn, Xiao Jiang, Li Li, Nai-Le Liu, Chao-Yang Lu, Anton Zeilinger, and Jian-Wei Pan. Quantum Teleportation in High Dimensions. *Physical Review Letters*, 123(7):070505, 8 2019. ISSN 0031-9007. doi: 10.1103/PhysRevLett.123.070505. URL https://link.aps.org/doi/10.1103/PhysRevLett.123.070505.

[68] Yang Huang and Wei Yang. Quantum Teleportation via Qutrit Entangled State. *Chinese Journal of Electronics*, 29(2):228–232, 3 2020. ISSN 1022-4653. doi: 10.1049/cje.2019.12.009. URL https://onlinelibrary.wiley.com/doi/10.1049/cje.2019.12.009.

[69] M.S. Blok, V.V. Ramasesh, T. Schuster, K. O'Brien, J.M. Kreikebaum, D. Dahlen, A. Morvan, B. Yoshida, N.Y. Yao, and I. Siddiqi. Quantum Information Scrambling on a Superconducting Qutrit Processor. *Physical Review X*, 11(2):021010, 4 2021. ISSN 2160-3308. doi: 10.1103/PhysRevX.11.021010. URL https://link.aps.org/doi/10.1103/PhysRevX.11.021010.

[70] Mohamed Omri, M.Y. Abd-Rabbou, E.M. Khalil, and S. Abdel-Khalek. Thermal information and teleportation in two-qutrit Heisenberg XX chain model. *Alexandria Engineering Journal*, 61(10):8335–8342, 10 2022. ISSN 11100168. doi: 10.1016/j.aej.2022.01.051. URL https://linkinghub.elsevier.com/retrieve/pii/S1110016822000618.

[71] Daniel Schraft, Marcel Hain, Nikolaus Lorenz, and Thomas Halfmann. Stopped Light at High Storage Efficiency in a Pr3+:Y2SiO5 Crystal. *Physical Review Letters*, 116(7):073602, 2 2016. ISSN 0031-9007. doi: 10.1103/PhysRevLett.116.073602. URL https://link.aps.org/doi/10.1103/PhysRevLett.116.073602.

[72] A. Nicolas, L. Veissier, L. Giner, E. Giacobino, D. Maxein, and J. Laurat. A quantum memory for orbital angular momentum photonic qubits. *Nature Photonics*, 8(3):234–238, 3 2014. ISSN 17494885. doi: 10.1038/nphoton.2013.355.

[73] Xian Qi Lin, Zhe Chen, Jia Wei Yu, Pei Qing Liu, Peng Fei Li, and Zhizhang Chen. An EIT-Based Compact Microwave Sensor With Double Sensing Functions. *IEEE Sensors Journal*, 16(2):293–298, 1 2016. ISSN 1530437X. doi: 10.1109/JSEN.2015.2480800.

[74] G G Grigoryan and Y T Pashayan. Adiabatic population transfer in three-level system with non-zero two-photon detuning. *Optics Communications*, 198(1-3):107–113, 2001. ISSN 0030-4018. doi: https://doi.org/10.1016/S0030-4018(01)01502-4. URL www.elsevier.com/locate/optcomhttps://www.sciencedirect.com/science/article/pii/S0030401801015024.

[75] Iavor I. Boradjiev and Nikolay V. Vitanov. Stimulated Raman adiabatic passage with unequal couplings: Beyond two-photon resonance. *Physical Review A*, 81(5):053415, 5 2010. ISSN 10502947. doi: 10.1103/PhysRevA.81.053415. URL https://link.aps.org/doi/10.1103/PhysRevA.81.053415.

[76] Y. Miroshnychenko, A. Gaëtan, C. Evellin, P. Grangier, D. Comparat, P. Pillet, T. Wilk, and A. Browaeys. Coherent excitation of a single atom to a Rydberg state. *Physical Review A*, 82(1):013405, 7 2010. ISSN 1050-2947. doi: 10.1103/PhysRevA.82.013405. URL https://link.aps.org/doi/10.1103/PhysRevA.82.013405.

[77] T. Cubel, B. K. Teo, V. S. Malinovsky, J. R. Guest, A. Reinhard, B. Knuffman, P. R. Berman, and G. Raithel. Coherent population transfer of ground-state atoms into Rydberg states. *Physical Review A*, 72(2):023405, 8 2005. ISSN 10502947. doi: 10.1103/PhysRevA.72.023405. URL https://link.aps.org/doi/10.1103/PhysRevA.72.023405.

[78] S. Weidt, J. Randall, S.C. Webster, K. Lake, A.E. Webb, I. Cohen, T. Navickas, B. Lekitsch, A. Retzker, and W.K. Hensinger. Trapped-Ion Quantum Logic with Global Radiation Fields. *Physical Review Letters*, 117 (22):220501, 11 2016. ISSN 0031-9007. doi: 10.1103/PhysRevLett.117.220501. URL https://link.aps.org/doi/10.1103/PhysRevLett.117.220501.

[79] Peter K. Molony, Philip D. Gregory, Zhonghua Ji, Bo Lu, Michael P. Köppinger, C. Ruth Le Sueur, Caroline L. Blackley, Jeremy M. Hutson, and Simon L. Cornish. Creation of Ultracold 87Rb 133Cs Molecules in the Rovibrational Ground State. *Physical Review Letters*, 113(25):255301, 12 2014. ISSN 0031-9007. doi: 10.1103/PhysRevLett.113.255301. URL https://link.aps.org/doi/10.1103/PhysRevLett.113.255301.

[80] R Menchon-Enrich, A Benseny, V Ahufinger, A D Greentree, Th Busch, and J Mompart. Spatial adiabatic passage: a review of recent progress. *Reports on Progress in Physics*, 79(7):074401, 7 2016. ISSN 0034-4885. doi: 10.1088/0034-4885/79/7/074401. URL https://iopscience.iop.org/article/10.1088/0034-4885/79/7/074401.

[81] Musang Gong, Min Yu, Ralf Betzholz, Yaoming Chu, Pengcheng Yang, Zhenyu Wang, and Jianming Cai. Accelerated quantum control in a three-level system by jumping along the geodesics. *Physical Review A*, 107(4): L040602, 4 2023. ISSN 2469-9926. doi: 10.1103/PhysRevA.107.L040602. URL https://link.aps.org/doi/10.1103/PhysRevA.107.L040602.

[82] Yoon-Seok Lee, Sang Min Lee, Heonoh Kim, and Han Seb Moon. Highly bright photon-pair generation in Doppler-broadened ladder-type atomic system. *Optics Express*, 24(24):28083, 11 2016. ISSN 10944087. doi: 10.1364/oe.24.028083.

[83] Michael Zugenmaier, Karsten B. Dideriksen, Anders S. Sørensen, Boris Albrecht, and Eugene S. Polzik. Long-lived non-classical correlations towards quantum communication at room temperature. *Communications Physics*, 1 (1):76, 11 2018. ISSN 2399-3650. doi: 10.1038/s42005-018-0080-x. URL https://www.nature.com/articles/s42005-018-0080-x.

[84] R. T. Willis, F. E. Becerra, L. A. Orozco, and S. L. Rolston. Four-wave mixing in the diamond configuration in an atomic vapor. *Physical Review A*, 79(3):033814, 3 2009. ISSN 1050-2947. doi: 10.1103/PhysRevA.79.033814. URL https://link.aps.org/doi/10.1103/PhysRevA.79.033814.

[85] Yoon-Seok Lee, Sang Min Lee, Heonoh Kim, and Han Seb Moon. Single-photon superradiant beating from a Doppler-broadened ladder-type atomic ensemble. *Physical Review A*, 96(6):063832, 12 2017. ISSN 2469-9926. doi: 10.1103/PhysRevA.96.063832. URL https://link.aps.org/doi/10.1103/PhysRevA.96.063832.

[86] Jiho Park, Heonoh Kim, and Han Seb Moon. Polarization-Entangled Photons from a Warm Atomic Ensemble Using a Sagnac Interferometer. *Physical Review Letters*, 122(14):143601, 4 2019. ISSN 0031-9007. doi: 10.1103/PhysRevLett.122.143601. URL https://link.aps.org/doi/10.1103/PhysRevLett.122.143601.

[87] Heung-Ryoul Noh and Han Seb Moon. Four-wave mixing in a ladder configuration of warm 87Rb atoms: a theoretical study. *Optics Express*, 29 (5):6495, 3 2021. ISSN 1094-4087. doi: 10.1364/OE.416960. URL https://opg.optica.org/abstract.cfm?URI=oe-29-5-6495.

[88] D. A. Kleinman. Theory of Second Harmonic Generation of Light. *Physical Review*, 128(4):1761–1775, 11 1962. ISSN 0031-899X. doi: 10.1103/PhysRev.128.1761. URL https://link.aps.org/doi/10.1103/PhysRev.128.1761.

[89] Jiao Lin, Ming-Hsien Lee, Zhi-Ping Liu, Chuangtian Chen, and Chris J. Pickard. Mechanism for linear and nonlinear optical effects in $\beta$BaB2O4 crystals. *Physical Review B*, 60(19):13380–13389, 11 1999. ISSN 0163-1829. doi: 10.1103/PhysRevB.60.13380. URL https://link.aps.org/doi/10.1103/PhysRevB.60.13380.

[90] Rihong Cong, Tao Yang, Fuhui Liao, Yingxia Wang, Zheshuai Lin, and Jianhua Lin. Experimental and theoretical studies of second harmonic generation for Bi 2O 2[NO 3(OH)]. *Materials Research Bulletin*, 47(9):2573–2578, 9 2012. ISSN 00255408. doi: 10.1016/j.materresbull.2012.04.145.

[91] Mark Fox. *Quantum Optics*. Oxford University Press, Oxford, 1 edition, 2006. ISBN 978-0-19-856673-1.

[92] L. Allen and J. H. Eberly. *Optical Resonance and Two Level Atoms*. Dover Publications, New York, 2 edition, 1987.

[93] Michael A. Nielsen and Isaac L. Chuang. *Quantum computation and quantum information*. Cambridge University Press, 2010. ISBN 9781107002173.

[94] G. Lindblad. On the generators of quantum dynamical semigroups. *Communications in Mathematical Physics*, 48(2):119–130, 6 1976. ISSN 0010-3616. doi: 10.1007/BF01608499. URL http://link.springer.com/10.1007/BF01608499.

[95] D.R. Lide, editor. *CRC Handbook of Chemistry and Physics*. CRC Press, Boca Raton, 81 edition, 2000. ISBN 0849304814.

[96] H. M. J. M. Boesten, C. C. Tsai, J. R. Gardner, D. J. Heinzen, and B. J. Verhaar. Observation of a shape resonance in the collision of two cold 87Rb atoms. *Physical Review A*, 55(1):636–640, 1 1997. ISSN 1050-2947. doi: 10.1103/PhysRevA.55.636. URL https://link.aps.org/doi/10.1103/PhysRevA.55.636.

[97] S. L. Cornish, N. R. Claussen, J. L. Roberts, E. A. Cornell, and C. E. Wieman. Stable 85Rb Bose-Einstein Condensates with Widely Tunable Interactions. *Physical Review Letters*, 85(9):1795–1798, 8 2000. ISSN 0031-9007. doi: 10.1103/PhysRevLett.85.1795. URL https://link.aps.org/doi/10.1103/PhysRevLett.85.1795.

[98] S Bize, Y Sortais, M. S Santos, C Mandache, A Clairon, and C Salomon. High-accuracy measurement of the 87Rb ground-state hyperfine splitting in an atomic fountain. *Europhysics Letters (EPL)*, 45(5):558–564, 3 1999. ISSN

0295-5075. doi: 10.1209/epl/i1999-00203-9. URL https://iopscience.iop.org/article/10.1209/epl/i1999-00203-9.

[99] Jun Ye, Steve Swartz, Peter Jungner, and John L. Hall. Hyperfine structure and absolute frequency of the 87Rb 5P3/2 state. *Optics Letters*, 21(16): 1280, 8 1996. ISSN 0146-9592. doi: 10.1364/OL.21.001280. URL https://opg.optica.org/abstract.cfm?URI=ol-21-16-1280.

[100] Alan L. Migdall, John V. Prodan, William D. Phillips, Thomas H. Bergeman, and Harold J. Metcalf. First Observation of Magnetically Trapped Neutral Atoms. *Physical Review Letters*, 54(24):2596–2599, 6 1985. ISSN 0031-9007. doi: 10.1103/PhysRevLett.54.2596. URL https://link.aps.org/doi/10.1103/PhysRevLett.54.2596.

[101] S D Jenkins, T Zhang, and T A B Kennedy. Motional dephasing of atomic clock spin waves in an optical lattice. *Journal of Physics B: Atomic, Molecular and Optical Physics*, 45(12):124005, 6 2012. ISSN 0953-4075. doi: 10.1088/0953-4075/45/12/124005. URL https://iopscience.iop.org/article/10.1088/0953-4075/45/12/124005.

[102] S. E. Hamann, D. L. Haycock, G. Klose, P. H. Pax, I. H. Deutsch, and P. S. Jessen. Resolved-Sideband Raman Cooling to the Ground State of an Optical Lattice. *Physical Review Letters*, 80(19):4149–4152, 5 1998. ISSN 0031-9007. doi: 10.1103/PhysRevLett.80.4149.

[103] J. Dalibard and C. Cohen-Tannoudji. Laser cooling below the Doppler limit by polarization gradients: simple theoretical models. *Journal of the Optical Society of America B*, 6(11):2023, 11 1989. ISSN 0740-3224. doi: 10.1364/JOSAB.6.002023. URL https://opg.optica.org/abstract.cfm?URI=josab-6-11-2023.

[104] Naoto Masuhara, John M. Doyle, Jon C. Sandberg, Daniel Kleppner, Thomas J. Greytak, Harald F. Hess, and Greg P. Kochanski. Evaporative Cooling of Spin-Polarized Atomic Hydrogen. *Physical Review Letters*, 61(8): 935–938, 8 1988. ISSN 0031-9007. doi: 10.1103/PhysRevLett.61.935. URL https://link.aps.org/doi/10.1103/PhysRevLett.61.935.

[105] Paul D. Lett, Richard N. Watts, Christoph I. Westbrook, William D. Phillips, Phillip L. Gould, and Harold J. Metcalf. Observation of Atoms Laser Cooled below the Doppler Limit. *Physical Review Letters*, 61(2):169–172, 7 1988. ISSN 0031-9007. doi: 10.1103/PhysRevLett.61.169. URL https://link.aps.org/doi/10.1103/PhysRevLett.61.169.

[106] Rudolf Grimm, Matthias Weidemüller, and Yurii B. Ovchinnikov. Optical Dipole Traps for Neutral Atoms. volume 42, pages 95–170. Academic Press, 2000. doi: 10.1016/S1049-250X(08)60186-X. URL https://www.sciencedirect.com/science/article/pii/S1049250X0860186X.

[107] Stefan Liam Kemp. *Laser cooling and optical trapping of Ytterbium*. PhD thesis, Durham University, 2017. URL http://etheses.dur.ac.uk/12166/.

[108] J Mitroy, M S Safronova, and Charles W Clark. Theory and applications of atomic and ionic polarizabilities. *Journal of Physics B: Atomic, Molecular and Optical Physics*, 43(20):202001, 10 2010. ISSN 0953-4075. doi: 10.1088/0953-4075/43/20/202001. URL https://iopscience.iop.org/article/10.1088/0953-4075/43/20/202001.

[109] Robert Alicki. The Markov master equations and the Fermi golden rule. *International Journal of Theoretical Physics*, 16(5):351–355, 5 1977. ISSN 0020-7748. doi: 10.1007/BF01807150. URL http://link.springer.com/10.1007/BF01807150.

[110] C.S. Adams and E. Riis. Laser cooling and trapping of neutral atoms. *Progress in Quantum Electronics*, 21(1):1–79, 1 1997. ISSN 00796727. doi: 10.1016/S0079-6727(96)00006-7. URL https://linkinghub.elsevier.com/retrieve/pii/S0079672796000067.

[111] Thomas F. Gallagher. *Rydberg Atoms*. Cambridge University Press, Cambridge, 1994. ISBN 978-0-521-02166-1.

[112] C S Adams, J D Pritchard, and J P Shaffer. Rydberg atom quantum technologies. *Journal of Physics B: Atomic, Molecular and Optical Physics*, 53 (1):012002, 1 2020. ISSN 0953-4075. doi: 10.1088/1361-6455/ab52ef. URL https://iopscience.iop.org/article/10.1088/1361-6455/ab52ef.

[113] Rolf Heidemann, Ulrich Raitzsch, Vera Bendkowsky, Björn Butscher, Robert Löw, Luis Santos, and Tilman Pfau. Evidence for Coherent Collective Rydberg Excitation in the Strong Blockade Regime. *Physical Review Letters*, 99 (16):163601, 10 2007. ISSN 0031-9007. doi: 10.1103/PhysRevLett.99.163601. URL https://link.aps.org/doi/10.1103/PhysRevLett.99.163601.

[114] N.V. Vitanov, B.W. Shore, L. Yatsenko, K. Böhmer, T. Halfmann, T. Rickes, and K. Bergmann. Power broadening revisited: theory and experiment. *Optics Communications*, 199(1-4):117–126, 11 2001. ISSN 00304018. doi: 10.1016/S0030-4018(01)01495-X. URL https://linkinghub.elsevier.com/retrieve/pii/S003040180101495X.

[115] Remy Legaie, Craig J. Picken, and Jonathan D. Pritchard. Sub-kilohertz excitation lasers for quantum information processing with Rydberg atoms. *Journal of the Optical Society of America B*, 35(4):892, 4 2018. ISSN 0740-3224. doi: 10.1364/JOSAB.35.000892. URL https://opg.optica.org/abstract.cfm?URI=josab-35-4-892.

[116] J. I. Thorpe, K. Numata, and J. Livas. Laser frequency stabilization and control through offset sideband locking to optical cavities. *Optics Express*, 16(20):15980, 9 2008. ISSN 1094-4087. doi: 10.1364/OE.16.015980. URL https://opg.optica.org/oe/abstract.cfm?uri=oe-16-20-15980.

[117] M. Ebert, M. Kwon, T.G. Walker, and M. Saffman. Coherence and Rydberg Blockade of Atomic Ensemble Qubits. *Physical Review Letters*, 115 (9):093601, 8 2015. ISSN 0031-9007. doi: 10.1103/PhysRevLett.115.093601. URL https://link.aps.org/doi/10.1103/PhysRevLett.115.093601.

[118] Yuechun Jiao, Nicholas L. R. Spong, Oliver D. W. Hughes, Chloe So, Teodora Ilieva, Kevin J. Weatherill, and Charles S. Adams. Single-photon stored-light Ramsey interferometry using Rydberg polaritons. *Optics Letters*, 45 (20):5888, 10 2020. ISSN 0146-9592. doi: 10.1364/OL.405143. URL https://opg.optica.org/abstract.cfm?URI=ol-45-20-5888.

[119] M. Saffman and T. G. Walker. Analysis of a quantum logic device based on dipole-dipole interactions of optically trapped Rydberg atoms. *Physical Review A*, 72(2):022347, 8 2005. ISSN 1050-2947. doi: 10.1103/PhysRevA.72.022347. URL https://link.aps.org/doi/10.1103/PhysRevA.72.022347.

[120] Joseph Lindon, Arina Tashchilina, Logan W. Cooke, and Lindsay J. LeBlanc. Complete Unitary Qutrit Control in Ultracold Atoms. *Physical Review Applied*, 19(3):034089, 3 2023. ISSN 2331-7019. doi: 10.1103/PhysRevApplied.19.034089. URL https://link.aps.org/doi/10.1103/PhysRevApplied.19.034089.

[121] Lin Xiu-Min, Zhou Zheng-Wei, Wu Yu-Chun, Wang Cheng-Zhi, and Guo Guang-Can. Preparation of Two-Qutrit Entangled State in Cavity QED. *Chinese Physics Letters*, 22(6):1318–1320, 6 2005. ISSN 0256-307X. doi: 10.1088/0256-307X/22/6/006. URL https://iopscience.iop.org/article/10.1088/0256-307X/22/6/006.

[122] Yue Fu, Wenquan Liu, Xiangyu Ye, Ya Wang, Chengjie Zhang, Chang-Kui Duan, Xing Rong, and Jiangfeng Du. Experimental Investigation of Quantum Correlations in a Two-Qutrit Spin System. *Physical Review Letters*, 129(10):

100501, 8 2022. ISSN 0031-9007. doi: 10.1103/PhysRevLett.129.100501. URL https://link.aps.org/doi/10.1103/PhysRevLett.129.100501.

[123] A. B. Klimov, R. Guzmán, J. C. Retamal, and C. Saavedra. Qutrit quantum computer with trapped ions. *Physical Review A*, 67(6):062313, 6 2003. ISSN 1050-2947. doi: 10.1103/PhysRevA.67.062313. URL https://link.aps.org/doi/10.1103/PhysRevA.67.062313.

[124] Ivaylo S. Madjarov, Jacob P. Covey, Adam L. Shaw, Joonhee Choi, Anant Kale, Alexandre Cooper, Hannes Pichler, Vladimir Schkolnik, Jason R. Williams, and Manuel Endres. High-fidelity entanglement and detection of alkaline-earth Rydberg atoms. *Nature Physics*, 16(8):857–861, 8 2020. ISSN 1745-2473. doi: 10.1038/s41567-020-0903-z. URL https://www.nature.com/articles/s41567-020-0903-z.

[125] Harry Levine, Alexander Keesling, Giulia Semeghini, Ahmed Omran, Tout T. Wang, Sepehr Ebadi, Hannes Bernien, Markus Greiner, Vladan Vuletić, Hannes Pichler, and Mikhail D. Lukin. Parallel Implementation of High-Fidelity Multiqubit Gates with Neutral Atoms. *Physical Review Letters*, 123(17):170503, 10 2019. ISSN 0031-9007. doi: 10.1103/PhysRevLett.123.170503.

[126] Hannes Busche, Simon W. Ball, and Paul Huillery. A high repetition rate experimental setup for quantum non-linear optics with cold Rydberg atoms. *European Physical Journal: Special Topics*, 225(15-16):2839–2861, 12 2016. ISSN 19516401. doi: 10.1140/epjst/e2015-50338-3.

[127] Jon H. Shirley. Modulation transfer processes in optical heterodyne saturation spectroscopy. *Optics Letters*, 7(11):537, 11 1982. ISSN 0146-9592. doi: 10.1364/OL.7.000537. URL https://opg.optica.org/abstract.cfm?URI=ol-7-11-537.

[128] D J McCarron, S A King, and S L Cornish. Modulation transfer spectroscopy in atomic rubidium. *Measurement Science and Technology*, 19(10):105601, 10 2008. ISSN 0957-0233. doi: 10.1088/0957-0233/19/10/105601. URL https://iopscience.iop.org/article/10.1088/0957-0233/19/10/105601.

[129] Chloe So. *Zeeman-tunable Modulation Transfer Spectroscopy*. PhD thesis, Durham University, Durham, 2020. URL http://etheses.dur.ac.uk.

[130] N. Šibalić, J.D. Pritchard, C.S. Adams, and K.J. Weatherill. ARC: An open-source library for calculating properties of alkali Rydberg atoms. *Computer*

*Physics Communications*, 220:319–331, 11 2017. ISSN 00104655. doi: 10.1016/j.cpc.2017.06.015.

[131] R. P. Abel, A. K. Mohapatra, M. G. Bason, J. D. Pritchard, K. J. Weatherill, U. Raitzsch, and C. S. Adams. Laser frequency stabilization to excited state transitions using electromagnetically induced transparency in a cascade system. *Applied Physics Letters*, 94(7):071107, 2 2009. ISSN 0003-6951. doi: 10.1063/1.3086305. URL http://aip.scitation.org/doi/10.1063/1.3086305.

[132] N. L. R. Spong. *Coherent Manipulation of Rydberg Polaritons*. PhD thesis, Durham, Durham, 2022.

[133] Acousto-Optic Theory Application Notes. Technical report, AA Opto-Electronics, Orsay. URL www.aaoptoelectronic.com.

[134] William D. Phillips and Harold Metcalf. Laser Deceleration of an Atomic Beam. *Physical Review Letters*, 48(9):596–599, 3 1982. ISSN 0031-9007. doi: 10.1103/PhysRevLett.48.596. URL https://link.aps.org/doi/10.1103/PhysRevLett.48.596.

[135] Zhong Lin, Kazuko Shimizu, Mingsheng Zhan, Fujio Shimizu, and Hiroshi Takuma Hiroshi Takuma. Laser Cooling and Trapping of Li. *Japanese Journal of Applied Physics*, 30(7B):L1324, 7 1991. ISSN 0021-4922. doi: 10.1143/JJAP.30.L1324. URL https://iopscience.iop.org/article/10.1143/JJAP.30.L1324.

[136] K. M. R. van der Stam, E. D. van Ooijen, R. Meppelink, J. M. Vogels, and P. van der Straten. Large atom number Bose-Einstein condensate of sodium. *Review of Scientific Instruments*, 78(1):013102, 1 2007. ISSN 0034-6748. doi: 10.1063/1.2424439. URL https://pubs.aip.org/aip/rsi/article/349799.

[137] G. Lamporesi, S. Donadello, S. Serafini, and G. Ferrari. Compact high-flux source of cold sodium atoms. *Review of Scientific Instruments*, 84(6), 6 2013. ISSN 00346748. doi: 10.1063/1.4808375.

[138] K. Dieckmann, R. J. C. Spreeuw, M. Weidemüller, and J. T. M. Walraven. Two-dimensional magneto-optical trap as a source of slow atoms. *Physical Review A*, 58(5):3891–3895, 11 1998. ISSN 1050-2947. doi: 10.1103/PhysRevA.58.3891. URL https://link.aps.org/doi/10.1103/PhysRevA.58.3891.

[139] E Pedrozo-Peñafiel, F Vivanco, P Castilho, R R Paiva, K M Farias, and V S Bagnato. Direct comparison between a two-dimensional magneto-optical trap and a Zeeman slower as sources of cold sodium atoms. *Laser Physics Letters*, 13(6):065501, 6 2016. ISSN 1612-2011. doi: 10.1088/1612-2011/13/6/065501. URL https://iopscience.iop.org/article/10.1088/1612-2011/13/6/065501.

[140] T. G. Tiecke, S. D. Gensemer, A. Ludewig, and J. T. M. Walraven. High-flux two-dimensional magneto-optical-trap source for cold lithium atoms. *Physical Review A*, 80(1):013409, 7 2009. ISSN 1050-2947. doi: 10.1103/PhysRevA.80.013409. URL https://link.aps.org/doi/10.1103/PhysRevA.80.013409.

[141] Yuri B. Ovchinnikov. Compact magneto-optical sources of slow atoms. *Optics Communications*, 249(4-6):473–481, 5 2005. ISSN 00304018. doi: 10.1016/j.optcom.2005.01.047. URL https://linkinghub.elsevier.com/retrieve/pii/S0030401805000684.

[142] Jiho Noh, Sung Jong Park, Chang Yong Park, Won-Kyu Lee, Dai-Hyuk Yu, and Jongchul Mun. High-performance experimental apparatus for large atom number 87Rb Bose-Einstein condensates. *Journal of the Korean Physical Society*, 61(7):1021–1027, 10 2012. ISSN 0374-4884. doi: 10.3938/jkps.61.1021. URL http://link.springer.com/10.3938/jkps.61.1021.

[143] Weibin Xie, Qing Wang, Xuan He, Shengwei Fang, Zhichao Yuan, Xianghui Qi, and Xuzong Chen. A cold cesium beam source based on a two-dimensional magneto-optical trap. *AIP Advances*, 12(7):075124, 7 2022. ISSN 2158-3226. doi: 10.1063/5.0099415. URL https://pubs.aip.org/aip/adv/article/2819147.

[144] Robert Löw, Hendrik Weimer, Johannes Nipper, Jonathan B Balewski, Björn Butscher, Hans Peter Büchler, and Tilman Pfau. An experimental and theoretical guide to strongly interacting Rydberg gases. *Journal of Physics B: Atomic, Molecular and Optical Physics*, 45(11):113001, 6 2012. ISSN 0953-4075. doi: 10.1088/0953-4075/45/11/113001. URL https://iopscience.iop.org/article/10.1088/0953-4075/45/11/113001.

[145] C. S. Hofmann, G. Günter, H. Schempp, N. L. M. Müller, A. Faber, H. Busche, M. Robert-de Saint-Vincent, S. Whitlock, and M. Weidemüller. An experimental approach for investigating many-body phenomena in Rydberg-interacting quantum systems. *Frontiers of Physics*, 9(5):571–586, 10 2014. ISSN 2095-0462. doi: 10.1007/s11467-013-0396-7. URL http://link.springer.com/10.1007/s11467-013-0396-7.

[146] Melvin M. Weiner. *Monopole Antennas*. CRC Press, 4 2003. ISBN 9780203912676. doi: 10.1201/9780203912676.

[147] Timothy Wiles and Peter. *Dynamics of bright solitary matter-waves*. PhD thesis, Durham University, Durham, 2013. URL http://etheses.dur.ac.uk.

[148] T. Arpornthip, C. A. Sackett, and K. J. Hughes. Vacuum-pressure measurement using a magneto-optical trap. *Physical Review A*, 85(3):033420, 3 2012. ISSN 1050-2947. doi: 10.1103/PhysRevA.85.033420. URL https://link.aps.org/doi/10.1103/PhysRevA.85.033420.

[149] St 171 ® and St 172-Sintered Porous Getters. Technical report, SAES Getters, 2007.

[150] B. P. Anderson and M. A. Kasevich. Loading a vapor-cell magneto-optic trap using light-induced atom desorption. *Physical Review A*, 63(2):023404, 1 2001. ISSN 1050-2947. doi: 10.1103/PhysRevA.63.023404. URL https://link.aps.org/doi/10.1103/PhysRevA.63.023404.

[151] S. Tsvetkov, M. Taslakov, and S. Gateva. Dynamics of the light-induced atomic desorption at homogeneous illumination. *Applied Physics B: Lasers and Optics*, 123(3), 3 2017. ISSN 09462171. doi: 10.1007/s00340-017-6662-6.

[152] D. S. Barker, E. B. Norrgard, J. Scherschligt, J. A. Fedchak, and S. Eckel. Light-induced atomic desorption of lithium. *Physical Review A*, 98(4):043412, 10 2018. ISSN 2469-9926. doi: 10.1103/PhysRevA.98.043412. URL https://link.aps.org/doi/10.1103/PhysRevA.98.043412.

[153] T. Karaulanov, M. T. Graf, D. English, S. M. Rochester, Y. J. Rosen, K. Tsigutkin, D. Budker, E. B. Alexandrov, M. V. Balabas, D. F. Jackson Kimball, F. A. Narducci, S. Pustelny, and V. V. Yashchuk. Controlling atomic vapor density in paraffin-coated cells using light-induced atomic desorption. *Physical Review A*, 79(1):012902, 1 2009. ISSN 1050-2947. doi: 10.1103/PhysRevA.79.012902. URL https://link.aps.org/doi/10.1103/PhysRevA.79.012902.

[154] Stoyan Tsvetkov and Sanka Gateva. Light induced atomic desorption for spectroscopy of optically thick Rb atomic vapor. In Tanja N. Dreischuh and Latchezar A. Avramov, editors, *20th International Conference and School on Quantum Electronics: Laser Physics and Applications*, page 5. SPIE, 1 2019. ISBN 9781510627680. doi: 10.1117/12.2516045. URL https://www.spiedigitallibrary.

org/conference-proceedings-of-spie/11047/2516045/Light-induced-atomic-desorption-for-spectroscopy-of-optically-thick-Rb/10.1117/12.2516045.full.

[155] Naota Sekiguchi, Takumi Sato, Kiyoshi Ishikawa, and Atsushi Hatakeyama. Spectroscopic study of a diffusion-bonded sapphire cell for hot metal vapors. *Applied Optics*, 57(1):52, 1 2018. ISSN 1559-128X. doi: 10.1364/AO.57.000052. URL https://opg.optica.org/abstract.cfm?URI=ao-57-1-52.

[156] Thomas G. Mayerhöfer, Susanne Pahlow, and Jürgen Popp. The Bouguer-Beer-Lambert Law: Shining Light on the Obscure. *ChemPhysChem*, 21(18): 2029–2046, 9 2020. ISSN 1439-4235. doi: 10.1002/cphc.202000464. URL https://onlinelibrary.wiley.com/doi/10.1002/cphc.202000464.

[157] Joseph Goodman. *Introduction to Fourier Optics*. W. H. Freeman, 4 edition, 5 2017.

[158] D Boddy. *First observations of Rydberg blockade in a frozen gas of divalent atoms*. PhD thesis, Durham University, Durham, 2014. URL http://etheses.dur.ac.uk.

[159] Tomasz M Brzozowski, Maria Maczynska, Michal Zawada, Jerzy Zachorowski, and Wojciech Gawlik. Time-of-flight measurement of the temperature of cold atoms for short trap-probe beam distances. *Journal of Optics B: Quantum and Semiclassical Optics*, 4(1):62–66, 2 2002. ISSN 1464-4266. doi: 10.1088/1464-4266/4/1/310. URL https://iopscience.iop.org/article/10.1088/1464-4266/4/1/310.

[160] Xiao Feng Shi. Suppressing Motional Dephasing of Ground-Rydberg Transition for High-Fidelity Quantum Control with Neutral Atoms. *Physical Review Applied*, 13(2), 2 2020. ISSN 23317019. doi: 10.1103/PhysRevApplied.13.024008.

[161] P.W. Shor. Algorithms for quantum computation: discrete logarithms and factoring. In *Proceedings 35th Annual Symposium on Foundations of Computer Science*, pages 124–134. IEEE Comput. Soc. Press, 1994. ISBN 0-8186-6580-7. doi: 10.1109/SFCS.1994.365700. URL http://ieeexplore.ieee.org/document/365700/.

[162] Lov K. Grover. A fast quantum mechanical algorithm for database search. In *Proceedings of the twenty-eighth annual ACM symposium on Theory of computing - STOC '96*, pages 212–219, New York, New York, USA, 1996.

ACM Press. ISBN 0897917855. doi: 10.1145/237814.237866. URL http://portal.acm.org/citation.cfm?doid=237814.237866.

[163] Jacob Biamonte, Peter Wittek, Nicola Pancotti, Patrick Rebentrost, Nathan Wiebe, and Seth Lloyd. Quantum machine learning. *Nature*, 549:195–202, 9 2017. ISSN 14764687. doi: 10.1038/nature23474.

[164] Bob Coecke and Ross Duncan. Interacting quantum observables: categorical algebra and diagrammatics. *New Journal of Physics*, 13(4):043016, 4 2011. ISSN 1367-2630. doi: 10.1088/1367-2630/13/4/043016.

[165] Aleks Kissinger and John van de Wetering. Universal MBQC with generalised parity-phase interactions and Pauli measurements. *Quantum*, 3:134, 4 2019. ISSN 2521-327X. doi: 10.22331/q-2019-04-26-134.

[166] Niel de Beaudrap and Dominic Horsman. The ZX calculus is a language for surface code lattice surgery. *Quantum*, 4:218, 1 2020. ISSN 2521-327X. doi: 10.22331/q-2020-01-09-218.

[167] Aleks Kissinger and John van de Wetering. Simulating quantum circuits with ZX-calculus reduced stabiliser decompositions. *Quantum Science and Technology*, 7(4):044001, 10 2022. ISSN 2058-9565. doi: 10.1088/2058-9565/ac5d20.

[168] Laurentiu Nita, Laura Mazzoli Smith, Nicholas Chancellor, and Helen Cramman. The challenge and opportunities of quantum literacy for future education and transdisciplinary problem-solving. *Research in Science & Technological Education*, 41(2):564–580, 4 2023. ISSN 0263-5143. doi: 10.1080/02635143.2021.1920905.

[169] Paweł Kurzyński, Adrian Kołodziejski, Wiesław Laskowski, and Marcin Markiewicz. Three-dimensional visualization of a qutrit. *Physical Review A*, 93(6):062126, 6 2016. ISSN 2469-9926. doi: 10.1103/PhysRevA.93.062126. URL https://link.aps.org/doi/10.1103/PhysRevA.93.062126.

[170] Sania Jevtic, Matthew Pusey, David Jennings, and Terry Rudolph. Quantum Steering Ellipsoids. *Physical Review Letters*, 113(2):020402, 7 2014. ISSN 0031-9007. doi: 10.1103/PhysRevLett.113.020402. URL https://link.aps.org/doi/10.1103/PhysRevLett.113.020402.

[171] Pranav Gokhale, Jonathan M. Baker, Casey Duckering, Natalie C. Brown, Kenneth R. Brown, and Frederic T. Chong. Asymptotic improvements to quantum circuits via qutrits. In *Proceedings of the 46th International Symposium on Computer Architecture*, pages 554–566, New York, NY, USA, 6

2019. ACM. ISBN 9781450366694. doi: 10.1145/3307650.3322253. URL https://dl.acm.org/doi/10.1145/3307650.3322253.

[172] Zheng-Hao Liu, Kai Sun, Jiannis K. Pachos, Mu Yang, Yu Meng, Yu-Wei Liao, Qiang Li, Jun-Feng Wang, Ze-Yu Luo, Yi-Fei He, Dong-Yu Huang, Guang-Rui Ding, Jin-Shi Xu, Yong-Jian Han, Chuan-Feng Li, and Guang-Can Guo. Topological Contextuality and Anyonic Statistics of Photonic-Encoded Parafermions. *PRX Quantum*, 2(3):030323, 8 2021. ISSN 2691-3399. doi: 10.1103/PRXQuantum.2.030323. URL https://link.aps.org/doi/10.1103/PRXQuantum.2.030323.

[173] Ruben Verresen. Everything is a quantum Ising model. 1 2023. URL http://arxiv.org/abs/2301.11917.

[174] Asmae Benhemou, Toonyawat Angkhanawin, Charles S. Adams, Dan E. Browne, and Jiannis K. Pachos. Universality of Z3 parafermions via edge mode interaction and quantum simulation of topological space evolution with Rydberg atoms. 11 2021. URL http://arxiv.org/abs/2111.04132.

[175] Reinhold A Bertlmann and Philipp Krammer. Bloch vectors for qudits. *Journal of Physics A: Mathematical and Theoretical*, 41(23):235303, 6 2008. ISSN 1751-8113. doi: 10.1088/1751-8113/41/23/235303. URL https://iopscience.iop.org/article/10.1088/1751-8113/41/23/235303.

[176] Julio Gea-Banacloche, Yong-qing Li, Shao-zheng Jin, and Min Xiao. Electromagnetically induced transparency in ladder-type inhomogeneously broadened media: Theory and experiment. *Physical Review A*, 51(1):576–584, 1 1995. ISSN 1050-2947. doi: 10.1103/PhysRevA.51.576. URL https://link.aps.org/doi/10.1103/PhysRevA.51.576.

## Colophon

This thesis is based on a template developed by Matthew Townson and Andrew Reeves. It was typeset with LaTeX $2_\varepsilon$. It was created using the *memoir* package, maintained by Lars Madsen, with the *madsen* chapter style. The font used is Latin Modern, derived from fonts designed by Donald E. Kunith. Figures were generated using Inkscape and the matplotlib python package. Diagrams of optical components utilised the gwoptics ComponentLibrary by Alexander Franzen. Numerical simulations were performed using python 3.9.12.